# Numerical Investigation of Particle Dispersion in a Gravitational Field and in Zero Gravity.

Marthe Willesvik Heggøy
The University of Bergen, Department of Physics and Technology
Bergen, Norway

June 29, 2017


A thesis in partial fulfilment of the requirements for the degree of *Master of Science* in the subject of Process Safety Technology

# Acknowledgements

I will start by thanking my amazing and supportive supervisor Prof. Pawel Jan Kosinski. He provided me with relevant literature and gave me good and specific feedback. He encouraged me through the whole process, always with a smile on his face and a positive attitude.

I would also like to thank Dr. Boris Balakin for setting up the foundation work of the CFD code and for being very helpful answering my questions about the software Star CCM+.

The last year has been both challenging and educational, with many ups and downs. In the downs, just a friendly and supportive face combined with some coffee crackers at the office did wonders. Therefore I would like to give a big thanks to all my fellow students that have helped me through this process. Without the support and encourage from them I would never have the strength to finish. Everyone have been so supportive and motivational.

A huge shout out to my life partner Edvin Eldholm that have endured with me also this year, even though I came home tired and frustrated after a long day at the office. I will also like to thank him and my aunt Lea Willesvik for proofreading this thesis and contributing with useful feedback.

Eventually I also need to thank my parents that have always been supportive and facilitated everything for me so that I was able to follow my dreams and finally complete my master degree.

Bergen, June 2017

Marthe Willesvik Heggøy

# Abstract

Combustible solid particles dispersed in gas has previously been discovered to be a precursor to a potential dust explosion. Consequently, a growing interest on the subject has been observed in recent years. Numerous experimental investigations have been performed on dust dispersion, but there are still some challenging issues when investigating the dust cloud combustion characteristics. Therefore, zero gravity condition ($g = 0$) have been suggested to be an "ideal" condition for dust cloud explosion research. The aim of this thesis is to supplement data from previous numerical and experimental studies that have been performed on the dispersion process in a modified Hartmann tube, and investigate the particle dispersion in this "ideal" condition.

Using the computational fluid dynamics (CFD) in form of the simulation software Star CCM+ the dispersion of the solid particles was investigated in this research. The Eulerian-Lagrangian approach was used to simulate the multiphase flow of a small amount of particles in gas. Different models were used in the CFD code to observe the effect on the movement of the particles. The computer aided design (CAD) model used in the simulations is based on the shape and dimensions for a standard modified Hartmann tube. The simulations were run in normal condition and in zero gravity condition. In addition, different inlet velocities, amount of particles and particle characteristics were varied. Finally, it was investigated how the coefficient of restitution, shear lift force and pressure gradient force influenced the particle dispersion.

In the course of the research it was discovered that the vertical velocity profile of the fluid flow distribution was non-symmetric, which correlates with similar previous numerical simulation performed on a single particle. Two main particle movement paths immediately after gas injection initiation were discovered. One of these paths also correlated with results from earlier work done. After running the simulations for about 100 ms, an approximately uniform particle cloud could be found with the help of volume fraction monitors. In normal condition the particle cloud settled as the velocity decayed and sedimented at the tube bottom. For the suggested "ideal" condition, the particles stayed in a dispersed cloud during the whole simulation.

An important discovery was how the dispersion got affected by the gas inlet velocity and the apparatus geometry. Gas injection velocities under 40 m/s did not generate a uniform particle cloud before the settling process started. When smaller particles were used, the results showed that the particle velocity, velocity decay time and dispersion time increased. When increasing the amount of particles present, no significant effect on the movement was found.

Three values for the restitution coefficient were tested and the results showed major deviations whether the particle-wall collisions were elastic or inelastic. As the collisions went from totally elastic to fully inelastic, the particle velocities decreased. The influence of the shear lift force, modelled using two approaches (Saffman and Sommefeld) was investigated.

A minor increase in particle velocity and particle lifting was observed for the Saffman approach. Finally, the pressure gradient force was investigated by comparing the results with a simulation where the force was enabled. Nevertheless, no significant differences were detected in this case.

# Nomenclature

| | | |
|---|---|---|
| $a$ | acceleration | $(\mathrm{m{\cdot}s^{-2}})$ |
| $A$ | area | $(\mathrm{m^2})$ |
| $C$ | Sutherman's constant | |
| $C_d$ | drag coefficient | |
| $C_{LS}$ | shear lift coefficient | |
| $C_{vm}$ | virtual mass coefficient | |
| $C_{\epsilon 1}, C_{\epsilon 2}, C_\mu$ | emperical constants | |
| $c_d$ | specific heat capacity of dispersed phase | $(\mathrm{J{\cdot}kg^{-1}{\cdot}K^{-1}})$ |
| $D$ | diameter | (m) |
| $E$ | energy | $(\mathrm{J{=}kg{\cdot}m^2{\cdot}s^{-2}})$ |
| $e$ | restitution coefficient | |
| $F$ | force | $(\mathrm{kg{\cdot}m{\cdot}s^{-2}})$ |
| $F_b$ | body forces | $(\mathrm{kg{\cdot}m{\cdot}s^{-2}})$ |
| $F_{dr}$ | drag forces | $(\mathrm{kg{\cdot}m{\cdot}s^{-2}})$ |
| $F_g$ | gravity forces | $(\mathrm{kg{\cdot}m{\cdot}s^{-2}})$ |
| $F_{LS}$ | shear lift forces | $(\mathrm{kg{\cdot}m{\cdot}s^{-2}})$ |
| $F_p$ | pressure gradient forces | $(\mathrm{kg{\cdot}m{\cdot}s^{-2}})$ |
| $F_s$ | surface forces | $(\mathrm{kg{\cdot}m{\cdot}s^{-2}})$ |
| $F_{vm}$ | virtual mass forces | $(\mathrm{kg{\cdot}m{\cdot}s^{-2}})$ |
| $f$ | mass transfer correction | |
| $f_i$ | acceleration due to distant forces | $(\mathrm{m{\cdot}s^{-2}})$ |
| $g$ | gravitational acceleration | $(\mathrm{m{\cdot}s^{-2}})$ |
| $h$ | heat transfer coefficient | |
| $k$ | turbulent kinetic energy | $(\mathrm{J{\cdot}kg^{-1}{=}m^2{\cdot}s^{-2}})$ |
| $l_e$ | length scale of the eddies | (m) |
| $m$ | mass | (kg) |
| $\dot{m}$ | rate of mass transfer | $(\mathrm{kg{\cdot}s^1})$ |
| $Nu_d$ | particle Nusselt number | |
| $p$ | pressure | (Pa) |
| $P_k$ | production of kinetic turbulent energy | $(\mathrm{W{\cdot}kg^{-1}{=}m^2{\cdot}s^{-3}})$ |
| $Re_s$ | Reynolds number for the shear flow | |
| $Re_d$ | particle Reynolds number | |
| $r$ | normal distance from the wall | (m) |
| $T$ | gas temperature | (K) |
| $T_w$ | temperature at the wall | (K) |
| $t$ | time | (s) |
| $u$ | velocity in x-direction | $(\mathrm{m{\cdot}s^{-1}})$ |
| $v$ | velocity in y-direction | $(\mathrm{m{\cdot}s^{-1}})$ |
| $w$ | velocity in z-direction | $(\mathrm{m{\cdot}s^{-1}})$ |
| $\vec{V}$ | flow velocity vector | $(\mathrm{m{\cdot}s^{-1}})$ |
| $\vec{n}$ | unit normal vector at a point on the surface | |
| $u_s$ | slip velocity | $(\mathrm{m{\cdot}s^{-1}})$ |
| $u^*$ | friction velocity | $(\mathrm{m{\cdot}s^{-1}})$ |
| $u^+$ | dimensionless velocity quotient | |

| | | |
|---|---|---|
| $u'$ | fluctation part of the velocity | $(\mathrm{m{\cdot}s^{-1}})$ |
| $\overline{u}$ | mean part of the velocity | $(\mathrm{m{\cdot}s^{-1}})$ |
| $V$ | volume | $(\mathrm{m^3})$ |
| $V_{mo}$ | molecules in a mixture sampling volume | $(\mathrm{m^3})$ |
| $y^+$ | dimensionless distance | (m) |
| $x$ | certesian coordinate | (m) |
| $Q_t$ | convective heat transfer to the particle | $(\mathrm{W{=}J{\cdot}s^{-1}})$ |
| $\dot{Q}$ | heat per unit time | $(\mathrm{W{=}J{\cdot}s^{-1}})$ |
| $\dot{W}$ | work per unit time | $(\mathrm{W{=}J{\cdot}s^{-1}})$ |

## Greek letters

| | | |
|---|---|---|
| $\alpha$ | volume fraction | |
| $\epsilon$ | turbulent dissipation rate | $(\mathrm{W{\cdot}kg^{-1}{=}m^2{\cdot}s^{-3}})$ |
| $\lambda$ | thrmal conductivity | $(\mathrm{W{\cdot}m^{-1}{\cdot}K^{-1}})$ |
| $\mu$ | dynamic viscosity | (Pa·s=kg·m·s) |
| $\mu_0$ | reference viscosity | (Pa·s=kg·m·s) |
| $\mu_t$ | turbulent viscosity | (Pa·s=kg·m·s) |
| $\nu_t$ | kinematic turbulent viscosity | $(\mathrm{m^2{\cdot}s^{-1}})$ |
| $\rho$ | density | $(\mathrm{kg{\cdot}m^{-3}})$ |
| $\tau$ | stress | $(\mathrm{Pa{=}N{\cdot}m^{-2}})$ |
| $\tau_w$ | shear stress at the pipe wall | $(\mathrm{Pa{=}N{\cdot}m^{-2}})$ |
| $\tau_e$ | eddy time-scale | $(\mathrm{Pa{=}N{\cdot}m^{-2}})$ |
| $\tau_v$ | momentim response time | (s) |
| $\nu_t$ | kinematic turbulent viscosity | $(\mathrm{m{\cdot}s^{-2}})$ |
| $\omega$ | curl of the fluid velocity | |
| $\sigma_k\sigma_\varepsilon$ | constants | |
| $\delta_{ij}$ | Kronecker-delta tensor | (m) |

## Subscripts

| | |
|---|---|
| $c$ | continuous phase |
| $d$ | dispersed phase |
| $i$ | coordinate direction with $i = x, y, z$ |
| $j$ | coordinate direction with $j = x, y, z$ |
| $n$ | normal |
| $t$ | tangential |

# Contents

**Acknowledgements** i

**Abstract** iii

**Nomenclature** vii

**1 Introduction and motivation** 1
1.1 Objective . . . 2
1.2 Background . . . 3
1.3 Literature survey . . . 3
1.3.1 Particle-cloud combustion research . . . 3
1.3.2 Dispersion of the solid particles . . . 3
1.3.3 Zero gravity, the "ideal condition". . . . 4
1.3.4 Particle properties and combustion characteristics . . . 6
1.3.5 Other relevant studies and results . . . 6
1.3.6 Numerical simulations . . . 8

**2 Computational Fluid Dynamics (CFD)** 9
2.1 Continuity equation . . . 10
2.2 Momentum equation . . . 10
2.3 Energy equation . . . 11
2.4 Physical boundary conditions . . . 11
2.5 Discretization . . . 12
2.6 Mesh . . . 13

**3 Modelling multiphase** 14
3.1 Basic equations . . . 16
3.1.1 Modelling the continuous phase . . . 16
3.1.2 Modelling the dispersed phase . . . 16
3.1.3 Particle-wall and particle-particle interaction . . . 17
3.2 Phase coupling . . . 18
3.2.1 Linear momentum coupling . . . 19
3.2.2 Momentum response time, $\tau_v$ . . . 22
3.2.3 Energy coupling . . . 22
3.3 Turbulence . . . 23

**4 Methodology** 25
4.1 Geometry . . . 25
4.2 Mesh . . . 27
4.3 Initial conditions . . . 28
4.4 Boundary conditions . . . 28
4.5 Properties of the fluid and the particle . . . 29
4.6 Turbulence models . . . 30
4.7 Models and the solver control . . . 31
4.8 Simulation (preparations) . . . 32

**5 Results and discussion** **32**
5.1 Gas flow . . . 33
5.1.1 Velocity . . . 33
5.1.2 Pressure . . . 40
5.1.3 Turbulent kinetic energy . . . 45
5.2 The movement of the particles . . . 47
5.3 Volume fraction . . . 55
5.4 Influence of the gas injection velocity . . . 58
5.5 Particle cloud propagation . . . 63
5.6 Duration of a steady particle cloud . . . 67
5.7 Explosive dust cloud generation . . . 72
5.8 Influence of the coefficient of restitution, $e$ . . . 77
5.9 Influence of the shear lift force, $F_{LS}$ . . . 80
5.10 Influence of the pressure gradient force, $F_p$ . . . 81

**6 Grid and time-step independence** **83**

**7 Concluding remarks** **84**
7.1 Further work . . . 85

# 1 Introduction and motivation

Any solid material that can burn in air will do so when ignited. The burning violence and speed increase when the material is divided into smaller parts, and as a result a higher contact area between the air and the combustible material occurres. If the particles are suspended in an adequately large volume of air, the particles may generate a dust explosion if allowed to burn unrestricted [1].

In an increasing number of industrial activities, pulverulent products are involved. They are used for energy production, in propelling systems and are present in metallurgical, chemical, pharmaceutical and food industries. By extraction, storage, transport and handling of fine solid particles, all these activities are exposed to explosion hazards [2].

In June 2015, flammable starch-based powder exploded at the Formosa Fun Coast, a recreational water park in Bali. As many as 508 people was injured, resulting in 15 fatalities. The explosion occurred on a music stage during an "color play Asia" party [3]. This is only one of many examples the hazard, which apparently harmless starch-powder represents.

Prevention of dust explosions is an ongoing process, and studies of dust behaviour can contribute to a better understanding of the dust explosion phenomena. Experiments and numerically investigation of the dispersion process can contribute to fully understand the nature of a dust explosion, by physically observe and measure the behaviour of the dust and use computer programs to get more accurate data.

Many experimental and theoretical studies of combustion of particle clouds have been performed. Parameters defining the explosiveness of a dust-air mixture include lower explosive limit (LEL), minimum ignition energy (MIE), limiting oxygen concentration and maximum explosion pressure ($P_{max}$). The modified Hartmann tube is one of the apparatus used to test these parameters experimentally [4].

However, in spite of strong practical interest, these parameters together with combustion characteristics such as burning velocity, quenching distance and flame structure are less understood for dust explosions. There are two reasons for the challanges in particle cloud combustion research. One is the complexity of the combustion process, the other reason is the gravitational force. The gravitational force causes buoyancy of the flame, as well as sedimentation of the particles. A microgravity field provides ideal conditions for experimental set-ups, therefore several experiments of particle cloud combustion in zero gravity have been conducted recently [5].

Until now, zero gravity condition have primary been investigated experimentally and only a few numerical studies have focused on dust dispersion in the modified Hartmann tube. Numerical investigation of the dispersion process in normal condition and in zero gravity condition can therefore give a great amount of information on particle movement in a generated dust cloud.

## 1.1 Objective

The objective of this thesis was to run Computational Fluid Dynamic (CFD) simulations, using the simulation software STAR CCM+, with the purpose to numerically investigate the dispersion of a given number of particles in normal condition and in zero gravity condition.

Firstly, the development of the gas flow in the modified Hartmann tube was investigated followed by a description of the movement of the particles as a result of particle-gas interactions. The movement of the particles was first analysed for varying gas injection velocities and different particle characteristics before the formation of an approximately uniform dispersion of the particles and the possibility of obtaining an explosive dust cloud was considered. Eventually numerical models affecting the particle-wall and the particle-gas interactions were analysed before the simulation results were verified with experimental results.

## 1.2 Background

## 1.3 Literature survey

The study of combustible particle clouds is of fundamental scientific interest as well as practical concern. Many experiments and theoretical studies of combustion of particle clouds have been performed in literature. The principal scientific interests are the combustion characteristics such as flame structure, burning velocity, quenching distance, minimum ignition energy and flammability limits. All though there has been an increasing interest in this field, the fundamental combustion mechanics of uniform mixtures of this kind is less understood for dust explosions, especially when compared to gas mixtures. This section provides an overview of previous particle cloud combustion experiments performed under normal conditions as well as zero gravity conditions.

### 1.3.1 Particle-cloud combustion research

Investigating particle cloud combustion characteristics in normal gravity conditions lead to several difficulties. Mixtures of solid particles and gas constitute a complex system and there are mainly two reasons why it is so challenging to carry out particle cloud research with a high quality and good reproducibility. The first is the complexity of the combustion process itself. The process of particle burning involves pyrolysis, gasification and mixing. The combustion characteristics are strongly affected by the chemical and physical properties and distributions of shape and size of the particles. A simple model of particle cloud combustion with simplified composition and a monodispersion of fuel particles is desired and therefore should be applied to understand the combustion mechanism [5]. The other main reason is the gravitational force that not only causes sedimentation of the fuel particles, but also buoyancy of the flame. This is some of the reasons why homogeneous gas mixture combustions are more easily investigated and a better understood system.

### 1.3.2 Dispersion of the solid particles

In order to perform experiments on particle cloud combustion, an external force is required to suspend the particles to achieve an approximate uniform mixture. Unfortunately, these forces lead to turbulence field formation in the fluid, which makes the combustion process and dispersion of particles much more complex [6].

Particle-gas mixtures have been created in many ways in the last years. Berlad and Tangirala [7] used acoustic waves, Ballal [8] used a dust feed assembly, Jarosinski, Podfilipski and Pu used a dispersion system with a very small scale of turbulence [9] and Peraldi [10] applied an electrical field to achieve an approximately uniform distribution of the dust air-mixture. Neverthless, all these

methods cause a strong turbulent flow. Regardless of the combustion problematics that occure with a high level of turbulence in the flow field, the solid fuel gets distributed, which was the main goal of introducin an external force. The next problem is to keep the the dust in suspension after the decay of turbulence. Under normal conditions it is impossible to maintain solid particles in suspension at rest [2] and therefore microgravity fields could be an alternative dispute resolution. According to Law and Faeth‘s review paper [11], microgravity fields provide ideal conditions for experiments of particle-cloud combustion, because no sedimentation occurs and it is possible to wait for the turbulence to decay before ignition [5]. Another reason why microgravity fields provide ideal conditions for combustion experiments of particle clouds, is that the flame does not get distorted by buoyancy [6].

### 1.3.3 Zero gravity, the "ideal condition".

Lee, Peraldi and Knystautas [12] compared combustion experiments performed with and without gravitational force to investigate the benefits of using a microgravity field. They tested how different delay times between dispersion and ignition effected the pressure rise and the variation of peak constant explosion overpressure. The goal was to obtain a quiescent dust cloud for a sufficiently long duration and thus be able to get fundamental data for the combustion process. They used high pressure air to disperse the aluminium dust into the spherical combustion chamber. The experiments were performed during the nominal 20 second duration of parabolic flights of the NASA KC-135 and ESA‘s Caravelle. The results showed that for short delay times (<50 ms) the pressure rise for normal gravity and microgravity were practically identical. As the delay time increased the pressure rise decreased sufficiently in normal gravity. For the microgravity case the pressure rise remained the same for different delay times. They concluded that the dispersion turbulence could be neglected after the first 5 seconds. As a result of the experiments, they identified the major problem to be the initial generation of the dust suspension and its introduction into the combustion chamber. The reproducibility was very challenging in a normal gravity field. Once the dust dispersion problem was resolved, experimental dust-cloud combustion set-ups could be designed and collection of decent data was feasible.

As Lee et al., also Berlad and Tangirala [7] used a parabolic flight to achieve microgravity condition. To maintain a rather constant pressure during combustion, an inflatable balloon was placed at the opposite ends of the speakers. Acoustic waves from the speakers lifted up an approximately uniform layer of dust. Peraldi and Tangirala observed a chattering or pulsating flame in the cylindrical experimental tube. This pulsating flame occured due to non-uniform stratified distribution of the dust by the acoustic waves creating the field [13]. Nevertless, according to Lee, Paraldi and Knystautas this type of vibrating flame is typical for flame propagation in tubes due to flame-pressure wave interactions [12]. Hanai et al. [6] investigated this pulsating flame characteristics further and explained

the mechanism of a pulsating flame propagation as follows: when the burning velocity is rapid, there is insufficient time for the particles to be heated by radiation from the burned region. Therefore the burning velocity slows down, the flame is first weakened by heat loss, but then it gets enhanced by the radiation heat again. This happens because the particles in front of the flame are sufficiently heated when the burning velocity slows down and this makes the flame oscilliate as it propagates [6, 14].

Parabolic flights are not the only opportunity to achieve microgravity conditions. Hanai et al. [5] measured the lean flammability limits of heterogeneous mixtures of combustible solid particles and air in a microgravity field using a cylindrical closed vessel in a drop capsule. Combustible particles (polymethylmethacrylate) were dispersed using an air jet, which created turbulence in the suspension. About 6 seconds after dispersion the decay of turbulence was completed and the mixture became quiescent without sedimentation. Using pressure histories, CCD camera images and flame speed measured by ionization probes, they could conclude that the flame became spherical and relatively smooth as a result of delaying the ignition. The flame speed increased with decreasing particle diameter and the equivalence ratio at the lean flammability limit narrowed linearly as the particle diameter was increased [5].

Jarosinski et al. [9] applied visualization methods to the experimental study of cornstarch dust-air mixture combustion. They used a closed vessel volume under microgravity conditions. Microgravity environment was created by a falling assembly in a drop tower and a high-speed video camera was used to record the flame propagation through the quiescent mixture. The duration of the dispersion process was about 100 ms and the ignition delay time for the turbulence to decay was 500 ms. The experiments showed a very irregular flame front at a late stage of the combustion. It was found that in dust flames only small part of heat was released at the flame front the remaining part being released far behind it [9].

Also Bozier and Veyssière [2] were concerned with the reproducibility and the possibility to make a good experimental set-up for particle-cloud combustion research. They planned to characterize the evolution as function of time of the aerodynamic flow field and the dust distribution inside a cylindrical combustion chamber. With the use of cornstarch as fuel and parabolic flights they developed an experimental process where they could perform high speed PIV and dust concentration measurements in microgravity conditions.

The pulsating flame or "chattering flame" as it also is called, was discovered already in 1989 by the research team from Lewis Research Center and University of California [13]. With the help of NASA Lewis drop towers and aircraft, a reduced gravitational environment was created. Of great scientific interest was the finding that for near-stoichiometric mixtures, the new mode of flame propagation was observed. The flame did not propagate steadily through the tube. They developed a new theory, which showed that chattering flame propagation was controlled by radiation from combustion products that heated the thin organic

layer sufficiently to cause autoignition.

Also Niioka et al. [15] discovered the phenomena of pulsating flame when investigating the lean flammability limit and flame dynamics of heterogeneous mixtures of solid particles and air. They observed the flame with the use of CCD video camera and the time history of pressure and ionization. They discovered that the pulsating flame only occurred near the lean flammability limit.

### 1.3.4 Particle properties and combustion characteristics

PMMA particles are often used in dust cloud experiments because they are roughly spherical and it is possible to use a narrow size distribution. The chemical and physical properties are also known [15, 5]. The combustion characteristics are strongly affected, not only by the chemical and physical properties, but also by distributions of shape and size of the particles. For best possible results, it is essential that the solid particles used in the experiment have a simple composition and gets approximately uniformly dispersed in the tube.

Cornstarch is another commonly used material. The cornstarch particles are almost spherical in shape and are fairly uniform in size distribution. It is important to note that the substance used as fuel in the experiments also can influence the results. Peraldi et al. [12] used aluminium with two different particle sizes ($5\mu$m and $20\mu$m). Nevertheless, an electron micrograph analysis indicated that the morphology is far form spherical. Instead, the geometries of the particles were highly irregular. When comparing their result for peak overpressure with the theoretical computed value for aluminium, there was a clear deviation. The theoretical computed value is on 11.6 atm, but they only achieved a peak overpressure of 6.2 atm. This could be accounted for by the problems involving adhesion of the dust to the wall, as well as heat loss and quenching as the flame reaches the walls of the spherical vessel.

Niioka et al. [15] investigated the effects of the equivalence ratio and particle diameters on the flame speed. The lean flammability limit was studied for different diameters and the trending result was that the lean flammability increased linearly as the mean diameter was increased. In their experiments they used an air jet to get a uniform distribution of the particles in a cylindrical steel vessel. The air was injected as soon as the drop capsule was released.

### 1.3.5 Other relevant studies and results

The Hartmann tube is the most common used apparatus to measure parameters associated with the explosiveness of dust. The minimum ignition energy (MIE) for different dust substances and characteristics is one of them. To perform this kind of experiment the dust sample is placed in a dispersion cup at the bottom of the tube before pressurised air is injected to disperse the dust. At the side of the tube geometry ignition sources are placed. A spark of desired energy is

discharged between the electrodes with the purpose to ignite the dust-gas mixture and whether an explosion occur can be recorded visually [1].

As mentioned earlier, in 1989, Berland et al. [13] investigated the feasibility of reduced gravity experiments and attained interesting results. With the use of acoustic waves fuel particles were dispersed, but the cloud did not reach sufficient uniformity. The longer the acoustic system operated the more particles tended to adhered to the tube walls, rather than remain in the suspension. As a result of these first two problems, quasi-steady flame propagation was never observed. The study showed that a cloud uniformity on the order of $\pm 10$ percent of the mean concentration can be regularly achieved for rich mixtures, and occasionally for lean mixtures. The study also showed that particle-wall adhesion levels on the order in 10 percent ($\pm 5$ percent) can be achieved for both lean and rich mixtures. Nevertheless, the most important result was that quasi-steady flame propagation was observed for fuel-rich mixtures.

As mentioned in [15] the radiation heat transfer is a well known dominating process which affects the flame propagation of dust-clouds. Krazinski et al. [16] explains that the increase in flame thickness and burning velocity comes from the excess enthalpy produced from radiation heat transfer. The radiation behaviour in a particle-cloud combustion is a very complicated process and has not yet been understood quantitatively. Joualin et al. [17, 18, 19] and Buckmaster [20, 21] tried to explain the effect of radiation heat transfer in a mixture of gas and particles, but reported similar models. Joulin et al. concluded that it is primarily the radiative heat transfer from the particles in the burned gas to the particles in the fresh mixture, which is dominant.

Laminar dust flames in reduced-gravity environment is a common main topic in dust-cloud combustion research. Goroshin et. al. [22] also investigated the combustion parameters within dust-cloud combustion. They used suspensions of iron powder consisting of different sizes and shapes, and changed the properties of the dust fuel to see what impact the different properties had on the combustion characteristics. They achieved reduced-gravity environment with the use of a parabolic flight and concluded that the experimental results of this work demonstrated the reduced-gravity environment benefits. It proved to be an invaluable tool in the dust combustion research. By comparing the results with theoretical models, they found out that one of the dominant mechanisms that differentiate dust flames from gas combustion is that the ignition of individual particles result in the appearance of micro-diffusion flames around each particle within the global reaction zone. The other is the theoretically predicted existence of a discrete regime of flame propagation, where the randomized structure of the media defines the flame speed and propagation limit rather then the reaction rates.

### 1.3.6 Numerical simulations

A lot of experiments have been carried out in diverse explosion chambers using different kinds of fuel and substances with a variety of dispersion devices. Murillo et al. [24, 23, 25] conducted the most comparable experiments and numerical simulations that were used for validation of the results in this thesis. In [23] they investigated the dynamics of dust dispersion in a modified Hartmann tube. The research included the discussion of particle size distribution, the agglomeration degree, the dust concentration within the cloud and the degree of turbulence of the suspension. With the use of a high speed camera and particle measurements, they were able to identify the dust cloud development and particle size distribution. A CFD-code was created with the use of data achieved from the experimental research. The numerical simulation gave results regarding the dispersion process, variation in fuel size distribution and the elevation of the ignition source. Three stages of the solid dispersion process were observed. Fragmentation phase, stabilization phase and the sedimentation phase. Murillo et al. conducted their experiments and numerical simulations in normal conditions, while the present research focuses on microgravity condition as well. They observed three stages of the dispersion process, it is the third and final stage that will be investigated in this thesis.

Murillo et al. [24, 25] used the Eulerian-Lagrangian approach to model the two-phase flow in their numerical simulations, which is the approach adopted into this thesis. The Eulerian-Lagrangian approach tracks each particle as it flows through the continuous phase. It takes into account more physical phenomena such as particle-particle and particle-wall interactions and gives more detailed results. Details of the Eulerian-Lagrangian approach are described in section 3. Murillo et al. [24, 25] continued their research with the use of numerical simulations and they investigated the placement of the ignition source in the tube. When varying the gas injection pressure, the particle size distribution was measured at different heights above the dispersion nozzle to validate the ignition point in the tube. The results showed that the ignition source should be placed 10 cm above the nozzle in a flammability test to get a low turbulence level. In order to obtain a fine particle size distribution at a given ignition height the injection pressure of the gas was suggested to be 5 bar.

Kosinski et al. [26] investigated dust lifting with a shock wave moving over particles in a channel. They used the E-L approach, and analysed the influence of the coefficient of restitution. The simulation results showed that the collisions affected the movement of the particles significant and low value of the restitution coefficient led to a slower entrainment process. Ilea et al. [27] performed the same simulations with a higher amount of particles. The results showed that the inter-particle and the particle-wall interactions had an influence on the dust lifting phenomena, and these phenomena needed to be included in the CFD code. They observed that a higher restitution coefficient led to a higher lifting effect on the particles.

# 2 Computational Fluid Dynamics (CFD)

Computational fluid dynamics (CFD) is a sub-division of fluid mechanics that uses numerical analysis and algorithms to solve mathematical equations involving fluid flows. Computers are used to solve the mathematical equations and extract information from the solutions. CFD is a research tool that obtains a large amount of accurate information compared to other commonly used techniques, such as experimental studies.

CFD is based on three fundamental equations governing fluid dynamics: the continuity, momentum and energy equation. In CFD the equations are mathematical statements of three fundamental physical principles:

1. Mass is conserved
2. Newton's second law, $\mathbf{F} = \mathbf{ma}$
3. Energy is conserved

In obtaining the basic equations of fluid motion a procedure is always followed. First, choose the appropriate fundamental physical principles from the law of physics listed above. Then, apply these physical principles to a suitable model of the flow and from this application extract the mathematical equations.

For the continuous fluid there are four different flow models: a finite control volume fixed in space with the fluid moving through it, a finite control volume moving along with the fluid, an infinitesimal fluid element fixed in space and an infinitesimal fluid element moving along a streamline in the fluid. Each model of the flow leads to a particular form of the governing equation: integral equations in conservation or nonconservation form and differential equations in conservation or nonconservation form.

The conservation form of the governing equations provides a numerical and computer programming convenience because the continuity, momentum and energy equation in conservation from can all be expressed by the same generic equations and they all have a divergence term on the left-hand side, the divergence of the flux of some kind. The conservation form of the equations is obtained directly from the flow model where a control volume is fixed in space rather than moving along with the fluid.

When describing a viscous flow these fundamental equations are called the Navier Stokes equations, where phenomena such as friction, thermal conduction and mass diffusion make the entropy increase. If the flow is non-viscous the equations are called the Euler equations and in this case the dissipative, transport phenomena of viscosity, mass diffusion, and the thermal conductivity are neglected [28].

## 2.1 Continuity equation

The governing flow equation, which results from the application of the physical principle of mass conservation to any of the four models of the flow mentioned above is called the continuity equation.

The continuity equation is based on the physical principle of conservation of mass. When applying the physical principle of mass conservation to any of the four flow models mentioned earlier, the continuity equation is formed. Regardless of which of the four forms the equation becomes, it is still the continuity equation. By indirect manipulation of these four different forms, they all can be written as:

*Rate of mass flow in - rate of mass flow out = rate of mass accumulation*

The form of the continuity equation, which is most relevant in this thesis, is the partial differential equation in conservation form. The Einstein summation method is used for an infinitesimally small element fixed in space to achieve the following:

$$\frac{\partial \rho_c}{\partial t} + \left[\frac{\partial(\rho_c u_i)}{\partial x_i}\right] = 0, \tag{1}$$

where $\rho_c$ is the density of the continuous phase and $u_i$ is the velocity component with $i = x, y, z$ representing the direction [28].

## 2.2 Momentum equation

The physical principle for the momentum equation is the Newton's second law, $\mathbf{F}$=m$\mathbf{a}$. In contrast to the continuity equation, the momentum equation is derived mainly with the use of one of the flow models, namely the infinitesimally small, moving fluid element model. This model is particularly convenient for the derivation of the momentum equation as well as the energy equation.

When Newton's second law is applied to the moving fluid element, we must take into consideration that it is a vector relation. This means that it can be split into three scalar directions.

There are two sources of force working on the moving fluid element [28]:

1. *Body forces*: these forces act at a distance and directly on the volumetric mass of the fluid element. Examples are gravitational, electric and magnetic forces.

2. *Surface forces*: act directly on the surface of the fluid element. There are only two kinds, viscous and pressure forces. The viscous force includes the shear and normal stress distribution acting on the surface and the friction between the outside fluid. The pressure force involves the total pressure acting on the elements surface by the surrounding fluid.

Momentum equation in conservation form written with Einstein summation notation:

$$\frac{\partial(\rho_c u_i)}{\partial t} + \frac{\partial(\rho_c u_i u_j)}{\partial x_j} = -\frac{\partial p}{\partial x_i} + \frac{\partial \tau_{ij}}{\partial x_j} + \rho_c f_i, \tag{2}$$

where $p$ is pressure, $\tau_{ij}$ is the stress working on the fluid element with $i = x, y, z$ and $j = x, y, z$. The acceleration due to distant forces is, $f_i$. This equation describes the motion of a viscous flow and is one of the Navier-Stokes equations. If the flow is inviscid, the equations are called Euler equations [28].

## 2.3 Energy equation

The energy equation is based on the physical principle of energy conservation, which also is the first law of thermodynamics. The law states that the total energy of an isolated system is constant; energy can be transformed from one form to another, but cannot be created or destroyed. When applying this physical principle on the flow model where a fluid element is moving with the flow, it states the following [28]:

*Rate of change of energy inside fluid element =*
*Net flux of heat into element*
*+*
*Rate of work done on element due to body and surface forces.*

Energy is conserved according to the following equation:

$$\frac{\partial(\rho_c E)}{\partial t} + \left[\frac{\partial(\rho_c E u_i)}{\partial x_i}\right] = \left[\frac{\partial(\tau_{ij} u_i)}{\partial x_i}\right] - Q_t, \tag{3}$$

where $E$ is the total energy and $Q_t$ is heat transfer to the particle from the continuous phase.

## 2.4 Physical boundary conditions

Although the governing equations mentioned above are the same for different types of flows past and through all kinds of geometries, the flow fields are quite different for each case. This is where the boundary conditions are essential. Boundary conditions determine the particular solution to be obtained from the governing equations. It is important to apply certain physical boundary conditions on the particular geometric surface for the numerical solutions to be accurate. This is crucial in CFD simulations. Any numerical solution of the governing flow equations needs a good numerical representation of the proper boundary conditions.

In this thesis we need to specify boundary conditions on the surface of the tube and the nozzle geometry, this kind of boundaries are physical solid boundaries. The inlet and outlet are considered as open boundaries and also need individual specifications.

For a viscous flow through a pipe or a channel the proper physical boundary condition is described as a no-slip condition. No-slip condition indicates that the relative velocity between the surface and the gas immediately at the surface is assumed to be zero:

$$u = v = w = 0. \tag{4}$$

If the material temperature of the surface and the temperature of the fluid layer immediately in contact with the surface of the wall are denoted by $T_w$, we can set the boundary condition on the gas $T$ to be:

$$T = T_w. \tag{5}$$

Inviscid flows, on the other hand, have a flow velocity at the wall that is a finite, nonzero value. This is due to the lack of friction between the flowing fluid and the surface. The result is a velocity vector tangent to the wall:

$$\vec{V} \cdot \vec{n} = 0, \tag{6}$$

which is the only surface boundary for an inviscid flow.

No-slip and inviscid flow conditions can be applied directly in the simulation code for the specific fluid flow. But if the flow also is turbulent we need to use specific models for this. This is due to the eddies that occur in the velocity field near the wall, see section 3.3.

## 2.5 Discretization

Discretization can be explained as a process where a closed-form mathematical expression is transformed into discrete counterparts. Closed-form mathematical equations can be functions or differential or integral equation involving functions. They all have an infinite continuum of values throughout the domain of interest. Numerical simulations can give solutions at only discrete points in the domain, and these points are called grid points. In order to solve equations at these points, discretization is necessary. The step of discretization is usually carried out as a fist step toward making the equations suitable for numerical evaluation. All methods in CFD utilize some form of discretization as a tool to get a discrete number from the governing equations in the computational domain. There are several methods of discretization but the most common ones are the finite difference (FD) method and the finite volume (FV) method.

In the FD method the partial derivatives in the equations governing the conservation of mass, momentum and energy are replaced by approximate algebraic difference quotients which are expressed strictly in terms of the flow-field variables at two or more of the discrete grid points. Further the partial differential equations are totally replaced by a system of algebraic equations, which can be solved for the values of the flow-field variables only at the discrete grid points [28].

Star CCM+ makes use of another commonly applied method, namely the FV method. The equations governing the fluid flow are also here replaced with algebraic equations. The difference is that in the FV methodology that Star CCM+ uses, the equations are in integral form. The domain of interest is divided into cells. The FV method starts with integration over an individual computational cell and solves for an computational node, which is placed in the center of each cell. This results as in the FD method to a system of algebraic equations.

There are to common techniques for solving the resulting algebraic equations, the implicit and explicit approach. In the explicit approach there is only one unknown parameter in each equation and they can be solved easily. In this thesis the implicit approach is used. This approach is more difficult because there is more than one unknown and the equations need to be solved simultaneously [29].

## 2.6 Mesh

Having discretized the original differential equations and achieved a system of algebraic equations, we need to split the physical domain into small cells to be able to solve the new set of equations. The discretized equations in CFD requires that the calculations are made over a collection of discrete grid points, where the grid points are located in the joints between the cells. The collection of these discrete grid points, cells or subdomains throughout the flow field is called a mesh or a grid. There are many ways to generate the mesh, but the determination of a proper mesh for the flow field over or through a given geometric shape is a very important part of the calculations. The type of mesh we choose for a given flow problem can determine the accuracy of the numerical solution [28].

In the simulation software Star CCM+, the mesh system is very adaptable and there exists numerous different combinations of features. The mesh operation tool makes it possible to fit the mesh to the boundary surface and the computational domain automatically. The mesh consists of different shapes of cells to achieve good mesh generation also in local geometries. This is especially useful when we need to customize a finer and more detailed mesh configuration around critical parts of the domain [29]. It is important to note that a finer mesh requires more computational time and power.

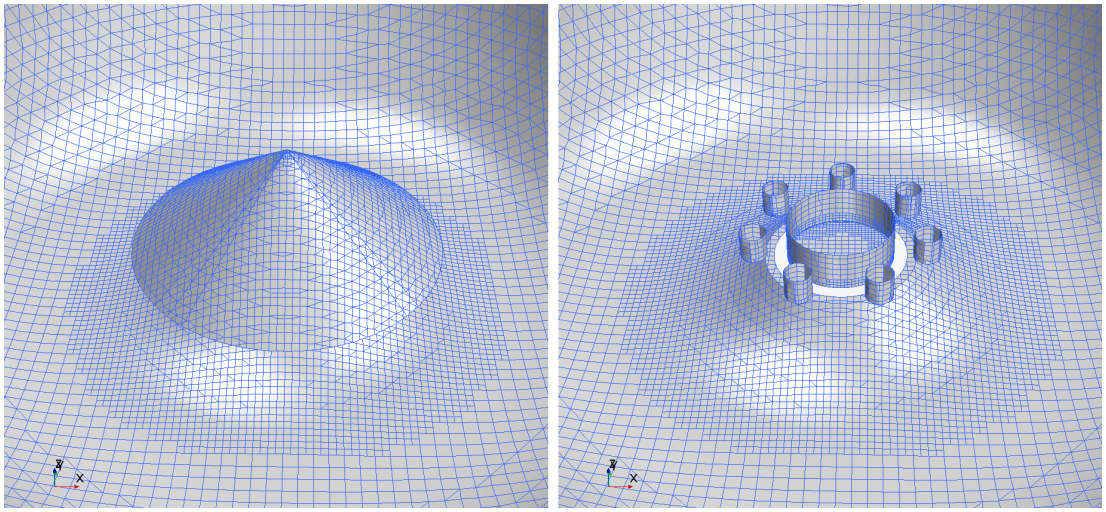

Figure 1: Illustration of how the mesh is finer and more detailed around the inlet region. On the left the inlet region from the CAD-model. On the right the inlet region without the inside mushroom and the outside cone.

# 3 Modelling multiphase

When studying the process of dust-cloud generation and explosions, a proper knowledge of multiphase flows is necessary. In multiphase flows and systems, different phases are mixed together at a macroscopic level. As a phase we understand the thermodynamically different states of matter, such as solid, liquid, gas and plasma. An example of such a system is a steam-water flow, which consist of one fluid phase and one gas phase. When discussing different flows it is also important to mention the difference between a multiphase and a multicomponent flow. A flow with just one component is a single component flow such as a nitrogen flow. One component means that there is only one chemical species and in this example the species is nitrogen. A multicomponent flow is a flow consisting of two or more chemical species that are mixed together at a molecular level.

In this thesis the system is a multiphase flow. Multiphase flows can have several phases present within the flow area. We distinguish between four main categories of multiphase flows: gas-liquid, gas- solid, liquid-solid and three-phase flows. In this thesis we have a gas-solid flow where the air is in gas phase and the glass particles are in solid form. The air alone represents a single phase multicomponent system because it consist of a mixture of various gases. Despite this, air is treated in this thesis as a single component with a known viscosity and thermal conductivity, which represents the gas mixture. The gas phase represents the carrier phase which is the continuous phase in this thesis, and the solid particles represent the dispersed phase. Because the solid particles represent a dispersed phase the flow characteristics follow a dispersed phase flow. The governing flow equations need to be modified and we need to introduce phase coupling, which is

the exchange of properties between phases (see section 3.2) [30, 31].

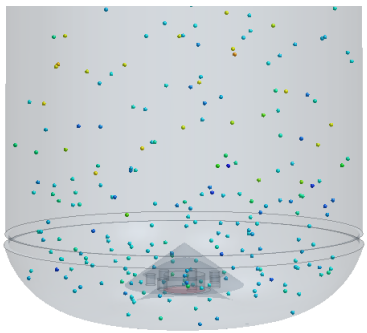

Figure 2: Simulation of multiphase flow consisting of solid particles dispersed in gas.

### Eulerian-Eulerian vs. Eulerian-Lagrangian

The two most common multiphase modelling approaches are Eulerian-Lagrangian (E-L) and the Eulerian-Eulerian (E-E). The main difference between these approaches is how they handle the dispersed phase. The continuous phase is in both cases treated with Eulerian approach, which means that the model solves Navier-Stokes equations for the fluid flow.

The E-L model solves Navier-Stokes equations for the continuous phase and solves the equation of motion for each individual particle. The E-L model treats each particle individually and tracks them as they move through the continuous phase. Every particle requires its own set of equations, which makes this model very accurate, but if the particle cloud is very dense this method requires an extreme amount of computational time.

The advantages with the E-L approach is that it gives detailed information about each particle and is therefore ideal in determining particle size distribution, heat and mass transfer between particles and the surrounding fluid, particle-particle collisions, coalescence and agglomeration. We also achieve a detailed model of turbulence interactions between particles and eddies in the carrier fluid. The disadvantages occur when the particle-cloud is very dense, as mentioned earlier. In order to implement this modelling for a dense cloud consisting of hundreds and thousands of solid particles, we need more computational resources. The method is therefore limited to a smaller concentration of particles (up to 40 percent in STAR-CCM+) [30].

In the E-E approach the dispersed solid phase is considered to be a continuous phase, as well as the carrier phase. This makes it possible to solve the Navier-stokes equations for each phase that is present. The conservation equations are solved simultaneously at every node in the domain of interest and a single pressure field is used for all phases. The computations are performed in fixed points in the multiphase flow field where properties such as temperature, velocity and pressure are monitored. This model covers the full range of volume fraction and we can

obtain mean quantities directly. It allows modelling mixing and separation of phases, but modelling size distribution of each particle is complex. The particle-particle and particle-wall interactions cannot be represented directly and strong coupling of phases make convergence difficult. This model is usually the best alternative for dense particle clouds where it is challenging to single out particles [30].

In this thesis the Eulerian-Lagrangian model and other physical models are applied to investigate the movement of the particles during and after dispersion, both in normal gravity and in a microgravity environment. This model treats each particle individually and this makes it possible to obtain detailed information about the particle movement in these two cases.

## 3.1 Basic equations

In all cases of multiphase flow the flow consists, as mentioned above, of a continuous phase and one or more dispersed phases. In this thesis there is only one dispersed phase in the form of solid particles. The equations used in the E-L approach based on the Star-CCM+ methodology [29] are shown in this section.

### 3.1.1 Modelling the continuous phase

The governing equations for the carrier phase are expressed in the Eulerian form based on equation (1) and (2), and are suitably modified to take into account the presence of the dispersed phase. In this thesis the dispersed phase does not have any significant affect on the continuous phase and therefore the flow model in the simulation describes an uncoupled flow (more about this in section 3.2 and 4.7).

### 3.1.2 Modelling the dispersed phase

In this thesis the flow involves a small number of dispersed elements and it is therefore possible to solve the set of Lagrangian equations for every element. In other words, the dispersed phase consists of solid particles and the software uses a Lagrangian framework to modify the conservation equations.

**Momentum:**

The momentum equation for one particle with mass $m_d$ is:

$$m_d \frac{d\mathbf{u}_d}{dt} = \mathbf{F}_s + \mathbf{F}_b, \tag{7}$$

where $\mathbf{u}_d$ is the instantaneous particle velocity, $\mathbf{F}_b$ is the body forces which is the force acting on the mass of the particle, such as gravity ($\mathbf{F}_g$):

$$\mathbf{F}_b = \mathbf{F}_g. \tag{8}$$

$\mathbf{F}_s$ is the surface forces, forces acting on the particle surface due to inter-phase forces and collisions:

$$\mathbf{F}_s = \mathbf{F}_{dr} + \mathbf{F}_p + \mathbf{F}_{vm} + \mathbf{F}_{LS}, \tag{9}$$

where $\mathbf{F}_{dr}$ is the drag force acting on the particle, $\mathbf{F}_p$ is the pressure force, $\mathbf{F}_{vm}$ is the virtual mass force and $\mathbf{F}_{LS}$ is the shear lift force [29].

**Energy:**

The single particle equation for energy in a multiphase system is:

$$\frac{dE}{dt} = \dot{Q} - \dot{W}, \tag{10}$$

where, $E$ is the total energy (kinematic plus internal), $\dot{Q}$ is the heat transfer rate to the system and $\dot{W}$ is the work per unit time done by the system on the surroundings. As mentioned earlier Equation (10) is simply the first law of thermodynamics for a closed system. This is the Lagrangian form of the energy equation. In this thesis there is one-way coupling and there are no work done by the dispersed phase that have any significant effect on the continuous phase [31].

### 3.1.3 Particle-wall and particle-particle interaction

**Particle-particle interaction**

For dilute gas-particle flows, particle-particle collisions are less important. This enables to neglect the loss of particle kinetic energy due to inter-particle collisions. The difference between a dilute dispersed phase and a dense dispersed phase is the number of solid particles with respect to the volume of the total mixture. In a dilute system the particle motion is controlled only by the fluid forces, drag and lift (see section 3.2.1). The particle volume fraction is defined as:

$$\alpha_d = \lim_{\Delta V \to \Delta V_{mo}} \frac{\Delta V_d}{\Delta V}, \tag{11}$$

where $\Delta V_d$ is the volume of the dispersed phase in the volume, $\Delta V$ is the sampling volume and $\Delta V_{mo}$ defines the molecules in a mixture sampling volume. It can be assumed that a system is dilute if $\alpha_d < 0.001$.

**Particle-wall interaction**

When modelling fluid flow of particles in pipes and channels it is important to calculate the particle-wall interactions properly, both for dilute and dense fluid flows. In this thesis the hard sphere model is used to calculate collisions and contact between the particles and the wall. This model can only be applied to binary collisions, which was sufficient in this research since the particulate phase was dispersed. Using this model pre- and post-collisional velocities are explicitly given by using the restitution coefficient ($e$). A further simplification that were made is that the instantaneous deformation of the sphere is not included in the equations.

The equation that relates the restitution coefficient with the velocity of the particle before and after the collision with the walls is:

$$\mathbf{u}_d^2 = e_t \mathbf{u}_{d,t}^1 - e_n \mathbf{u}_{d,n}^1, \tag{12}$$

where $\mathbf{u}_d$ is the particle velocity, subscript $n$ and $t$ refer to the state for normal and tangential to the wall, and the superscript 1 and 2 refer to the state before and after the collision. This equation can be split into two equations since the $n$ and $t$ components are orthogonal [29, 31]:

$$\mathbf{u}_{d,t}^2 = e_t \mathbf{u}_{d,t}^1 \tag{13}$$

$$\mathbf{u}_{d,n}^2 = -e_n \mathbf{u}_{d,n}^1. \tag{14}$$

The value for the restitution coefficient ranges between zero and one. A completely elastic collision, where the kinetic energy will be conserved, represents a restitution coefficient value of one. When it is zero it is a completely inelastic collision and the particle will merge with the wall and the kinetic energy will dissipate [31].

## 3.2 Phase coupling

For the Eulerian-Lagrangian method, the two-way coupling model allows the dispersed phase to exchange mass, momentum and energy with the continuous phase. Because of the small size of the particles (diameter between 106$\mu$m - 500$\mu$m) and few number of particles present, the dispersed phase has a negligible influence on the flow of the continous phase. This simplification also shortens the computational time. On the other hand, the motion of the continous phase has a significant effect on the dispersed phase. This kind of flow is referred to as a one-way coupled flow. The continuous phase influences the dispersed phase through drag in the momentum equation and heat transfer in the energy equation. It is important to notice that there is no mass transfer between the phases due to no change in the particles mass as it flows in the carrier phase [29, 31].

### 3.2.1 Linear momentum coupling

As a result of interphase drag and lift forces, linear momentum coupling between the phases appears due to [31]:

#### The drag force, $\mathbf{F}_{dr}$

The drag force $\mathbf{F}_{dr}$ is an inter-phase force acting on the particle due to the pressure differences on the particle surface and the fluid flowing around. This difference in pressure is due to the relative velocity $(u_c - u_d)$ between the continuous phase and the particle, also called the slip velocity $u_s$. The force is defined as:

$$\mathbf{F}_{dr} = \frac{1}{2} C_d \rho_c A_d |\mathbf{u}_c - \mathbf{u}_d|(\mathbf{u}_c - \mathbf{u}_d), \tag{15}$$

where $C_d$ is the drag coefficient, $\rho_c$ is the density of the continuous phase and $A_d$ is the particle cross-sectional area. The drag coefficient needs to be derived from experiments or theoretical studies. In this thesis the Schiller-Naumann correlation is used for defining the drag coefficient. This method is suitable for spherical solid particles and it is formulated as:

$$C_d = \begin{cases} \frac{24}{Re_d}\left(1 + 0.15 Re_d^{0.687}\right) & Re_d \leq 10^3 \\ \\ 0.44 & Re_d > 10^3, \end{cases} \tag{16}$$

where $Re_d$ is the particle Reynolds number defined as:

$$Re_d \equiv \frac{\rho_c |\mathbf{u}_c - \mathbf{u}_d| D_d}{\mu_c}, \tag{17}$$

where $D_d$ is the particle diameter and $\mu_c$ is the viscosity of the continuous phase. This corrrelation is only available when the continuous phase is viscous [31, 29].

#### The pressure gradient force, $\mathbf{F}_p$

The pressure gradient force is also a inter-phase force that acts on the particle when flowing in the carrier fluid. The force occurs due to the pressure differences in the continuous phase and is given by:

$$\mathbf{F}_p = -V_d \nabla p, \tag{18}$$

where $V_d$ is the particle volume and $\nabla p$ is the gradient of the static pressure in the carrier fluid. It is assumed that the pressure gradient is constant over the volume of the particle. A minus sign is used because the force works in the opposite direction of the pressure gradient [31, 29].

### The shear lift force, $\mathbf{F}_{LS}$

Lift forces working on a particle are due to particle rotation in the flow field. The rotation may be caused by different sources, for instance a velocity gradient or a particle-particle contact or, a rebound from a surface.

Figure 3 illustrates the Saffman lift force. This force is due to the pressure distribution developed on a particle in a velocity gradient. On the top of the particle there is a higher velocity that gives rise to a low pressure, and at the bottom where the velocity is lower there is a high pressure that gives rise to a lift force.

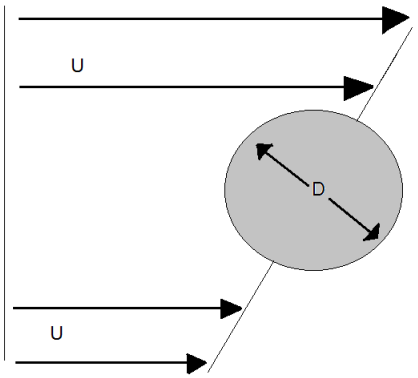


Figure 3: Illustration of Saffman lift force.

The shear lift force calculated by Saffman [32]:

$$\mathbf{F}_{LS} = 1.615 D_d^2 (\rho_c \mu_c)^{0.5} \left| \frac{\delta \mathbf{u}_c}{\delta y} \right| \mathbf{u}_s, \tag{19}$$

where $\mu_c$ is the dynamic viscosity of the fluid and $\mathbf{u}_s$ is the slip velocity. The y-direction is the direction of the velocity gradient. Written in three dimensions, this equation is:

$$\mathbf{F}_{LS} = C_{LS} \frac{\rho_c \pi}{8} D_d^3 (\mathbf{u}_s \times \boldsymbol{\omega}), \tag{20}$$

where $C_{LS}$ is the shear lift coefficient and $\boldsymbol{\omega}$ is the curl of the fluid velocity:

$$\boldsymbol{\omega} = \bigtriangledown \times \mathbf{u}_c. \tag{21}$$

Saffman [32] defined a shear lift coefficient that recover solutions for low Reynolds number:

$$C_{LS} = \frac{4.1126}{Re_S^{0.5}}, \tag{22}$$

where $Re_S$ is the Reynolds number for shear flow

$$Re_S = \frac{\rho_c D_d^2 |\boldsymbol{\omega}|}{\mu_c}. \tag{23}$$

Mei [33] proposed a coefficient for broader values of the Reynolds numbers, also called the Sommerfeld coefficient:

$$C_{LS} = \frac{4.1126}{Re_S^{0.5}} f Re_d, Re_S, \tag{24}$$

where $f Re_d, Re_S$:

$$f Re_d, Re_S = \begin{cases} (1 - 0.3334\beta^{0.5})e^{-0.1 Re_d} + 0.3314\beta^{0.5}, & (Re_d \leq 40) \\ 0.0524(\beta Re_d)^{0.5}, & (Re_d > 40), \end{cases} \tag{25}$$

and $Re_d$ is the particle Reynolds number and:

$$\beta = 0.5 \frac{Re_S}{Re_d}. \tag{26}$$

Another lift force is the Magnus force. When a particle rotates in a fluid the lift is caused by a pressure differential between both sides of the particle. The pressure differential is caused by the difference in velocity caused by the rotating particle, see Figure 4 [31].

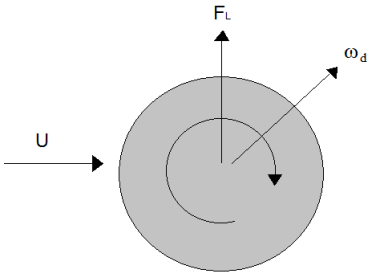


Figure 4: Illustration of Magnus force.

### The virtual mass force, $\mathbf{F}_{vm}$ and the body forces, $\mathbf{F}_b$

The virtual mass effect appears when a body, like a particle, is accelerated through a fluid. It is the additional work done by the particle that creates the corresponding acceleration of the fluid [31]. When including the virtual mass force the accelerating flow gets more realistic since the inertia of surrounding fluid influences

the acceleration of the particle. This effect is equal to a constant multiplied by the mass of fluid displaced by the particle:

$$\mathbf{F}_{vm} = -C_{vm}\rho V_d \frac{d(\mathbf{u}_d - \mathbf{u})}{dt}. \tag{27}$$

The body forces are forces acting throughout the volume of the particle. The most common body force is weight due to gravity, which is expressed as:

$$\mathbf{F}_g = m_d \mathbf{g}, \tag{28}$$

where $\mathbf{g}$ is the gravitational acceleration vector and $m_d$ is the mass of the dispersed phase [29].

### 3.2.2 Momentum response time, $\tau_v$

Momentum response time is a measure of how fast the dispersed phase responds to a velocity change in the continuous phase.

Momentum response time ($\tau_v$) is [31]:

$$\tau_v = \frac{\rho_d \cdot D^2}{18\mu}, \tag{29}$$

where the dynamic viscosity ($\mu$) of an ideal gas as a function of the temperature:

$$\mu = \mu_0 \frac{T_0 + C}{T + C} (\frac{T}{T_0})^{\frac{3}{2}}. \tag{30}$$

$\mu_0$ is a reference viscosity, $T_0$ is a reference temperature and $C$ is the Sutherland's constant for the gaseous material. For air we have the following: $\mu_0$= 18.72·$10^{-6}$ Pa s, $T_0$= 291.15 K and $C$= 120.

### 3.2.3 Energy coupling

Heat transfer across the phases can take place due to interphase temperature differences. In a one-way coupled multiphase flow it is therefore necessary to include the energy coupling, where the continuous phase affects the dispersed particles. When using a material particle it is assumed to be internally homogeneous which, from a thermal point of view implies a low Biot number, for example less than approximately 0.1. Then the substance is labelled as "thermally thin," and temperature can be assumed to be constant throughout the material volume [29].

The energy equation for a particle, assuming convective heat transfer as the primary heat transfer mechanism, is:

$$Q_t = m_d c_d \frac{dT_d}{dt} = f h A_s (T_c - T_d). \tag{31}$$

Here, $Q_t$ represents the rate of convective heat transfer to the particle from the continuous phase, $A_s$ is the particle surface area, $T_c$ and $T_d$ represent the temperature in the continuous and dispersed phase.

$h$ is the heat transfer coefficient and can be computed as a function of the continuous phase thermal conductivity ($\lambda_c$), the particle *Nusselt number* ($\mathrm{Nu}_d$) and the particle diameter ($D_d$):

$$h = \frac{\lambda_c N u_d}{D_d}. \tag{32}$$

The factor $f$ is a mass transfer correction, for which the formulation of El Wakil and others [34] is used:

$$f = \frac{z}{e^z - 1} \tag{33}$$

with

$$z = \frac{-\dot{m}_d c_d}{h A_s}. \tag{34}$$

In the limit $\dot{m}_d \to 0, f \to 1$. In this thesis the rate of mass transfer to the particle ($\dot{m}_d$) equals zero and thus $f$ equals one.

For spherical particles we can write the total interfacial area per unit volume as a function of the volume fraction and the particle diameter:

$$A_s = \frac{6\alpha_d}{d}. \tag{35}$$

## 3.3 Turbulence

Air-particle interactions are strongly influenced by turbulence, which is a property of the flow and not only of the fluid. Because of the high diffusivity, turbulence leads to mixing of the fluid and is characterized by chaotic changes in pressure and flow velocity. As a consequence of vortices generated in the flow, there is continuous fluctuation of velocities. Turbulent flow is in contrast to a laminar flow regime, which occurs when a fluid flows in parallel layers. The transition from a laminar regime to a turbulent flow regime can be predicted by a dimensionless constant called the Reynolds number. Reynolds number calculates the balance between kinetic energy and viscous cushioning in a fluid flow. When the Reynolds number reaches the critical value, the flow becomes turbulent. Because of the influence on the flow characteristics and the air-particle interaction, a turbulence model needs to be included in the calculations to get valid solutions.

**Continuous phase**

In this thesis turbulence in the continuous phase is handled by the k-$\epsilon$ turbulence model. For the computational time to be sufficiently small, several simplifications needs to be made to the Navier Stokes equations governing the fluid flow. The resulting Reynold averaged Navier Stokes (RANS) equations give a mean value of the turbulent flow instead of the fluctuations. Reynolds Averaged conservation equations are derived from the Navier Stokes equations and a stress tensor called Reynold stress is formed. With Einstein summation convention it can be written as [31]:

$$-\rho_c \overline{u'u'} = \mu_t \left( \frac{\partial \overline{u}_i}{\partial \overline{x}_j} + \frac{\partial \overline{u}_j}{\partial \overline{x}_i} \right) - \frac{2}{3} \rho_c k \delta_{ij}. \tag{36}$$

The velocity field of the flow can be split into a mean part ($\overline{u}$) and a fluctuating part ($u'$):

$$u = \overline{u} + u'. \tag{37}$$

The turbulent viscosity, $\mu_t$ is expressed as:

$$\mu_t = \rho_c \nu_t = C_\mu \rho_c \frac{k^2}{\epsilon}, \tag{38}$$

where the model coefficient $C_\mu$ =0.09, is an empirically determined constant and $\nu_t$ is the kinematic turbulent viscosity. $\delta_{ij}$ is the Kronecker-delta tensor: $\delta_{ij}$=0 when $i \neq j$ and $\delta_{ij}$=1 when $i = j$ ($i$ and $j$ stand for the coordinate directions) [35].

Because there are more unknown variables than equations, the equation is not closed and for this we need to apply turbulence models. The widely used two-equation model, k-$\epsilon$ turbulence model, solves the transport equation for the turbulent kinetic energy ($k$) and the turbulent dissipation rate ($\epsilon$). The equations can be written as follow [29]:

$$\frac{\partial}{\partial t}(\rho_c k) + \frac{\partial}{\partial x_j}(\rho_c k \overline{u}_j) = \frac{\partial}{\partial x_j} \left( \left( \mu_c + \frac{\mu_t}{\sigma_k} \right) \frac{\partial k}{\partial x_j} \right) + \rho_c P_k - \rho_c \epsilon, \tag{39}$$

$$\frac{\partial}{\partial t}(\rho_c \epsilon) + \frac{\partial}{\partial x_j}(\rho_c \epsilon \overline{u}_j) = \frac{\partial}{\partial x_j} \left( \left( \mu_c + \frac{\mu_t}{\sigma_\epsilon} \right) \frac{\partial \epsilon}{\partial x_j} \right) + C_{\epsilon 1} \frac{\epsilon}{k} \rho_c P_k - C_{\epsilon 2} \frac{\epsilon}{k} \rho_c \epsilon. \tag{40}$$

In both equations $P_k$ represents a production term. More specific the production of kinetic turbulence energy. $C_{\epsilon 1}$ and $C_{\epsilon 2}$ are two empirical constants of the model. $\sigma_\epsilon$ is the turbulent Prandtl number for $\epsilon$ equation and $\sigma_k$ is the turbulent Prandtl number for $k$ equation. This means that they also are model coefficients. Further $\rho_c P_k$ can be expressed:

$$\rho_c P_k = \mu_t \left( \frac{\partial \overline{u}_i}{\partial \overline{x}_j} + \frac{\partial \overline{u}_j}{\partial \overline{x}_i} \right) \frac{\partial \overline{u}_i}{\partial \overline{x}_j}. \tag{41}$$

### Dispersed phase

For the dispersed phase the turbulent dispersion model describes the effect of turbulence on the solid particles. This model collaborates with the RANS turbulence model and is included in the simulations of each single particle. A particle located in a turbulent flow experiences fluctuations and turbulent eddies. Eddies are the swirling of a fluid and the reverse current created when the fluid is in a turbulent flow regime [28]. The particle remains in the eddy until either the eddy time-scale $\tau_e$ is exceeded, or the separation between the particle and the eddy exceeds the length scale of the eddy $l_e$. This makes the particle trajectories to be random and difficult to predict [29].

### Boundary interactions

Close to the wall in a turbulent fluid the flow can be split into three different layers. The layer adjacent to the wall is called the viscous sub-layer. The viscous sub-layer goes over to a buffer layer and close to the center of the tube is the turbulent core. In the viscous sub-layer the velocity is constant but the viscous shear is important. Eddies can occur, but the eddy diffusion is minor in this layer. On the other hand, in the buffer layer eddies play a much bigger role. Viscous shear and shear occur due to eddy diffusion in the flow. In the turbulent core the eddy viscosity dominates and therefore the viscous shear can be neglected.

To express the velocity distribution in a turbulent flow near a wall, it is useful to use dimensionless quantities. The equations are as follows:

$$u^* = \sqrt{\frac{\tau_w}{\rho_c}} \tag{42}$$

$$u^+ \equiv \frac{u}{u^*} \tag{43}$$

$$y^+ \equiv \frac{r u^* \rho_c}{\mu_c}. \tag{44}$$

In the equations $u^*$ represents the friction velocity, $\tau_w$ is the shear stress at the pipe wall and $r$ is the normal distance from the wall to the center of the flow field. $u^+$ is the dimensionless velocity quotient and $y^+$ is the dimensionless distance. A universal velocity distribution law is used to relate $u^+$ to $y^+$.

# 4 Methodology

## 4.1 Geometry

The geometry in this thesis is based on the modified Hartmann tube apparatus used for dust explosion experiments (Figure 5). Since the apparatus is used to measure the minimum ignition energy (MIE) in a dust cloud, there are openings

for the ignition electrodes on the side of the tube wall, approximately at the middle of the cylinder height. These openings were closed in the CAD-model used in this thesis, only the outline is visible in Figure 5. The apparatus consists of a cylindrical glass tube with a volume of 1.1 litre and a diameter of 68 mm. The dispersion nozzle is located in the bottom of the cylindrical tube. The dispersion nozzle contains seven gaps, where the injected gas enters the glass tube (Figure 6). At the top of the Hartmann tube there is an outlet that is covered by a thin filter that prevents the particles from exiting the tube during the dispersion process. The CAD-model used in the simulations is based on the experimental apparatus. Figure 6 shows the inlet boundary where the gas was injected into the nozzles and then further through the gaps and into the tube.


Figure 5: Left: Hartmann tube used in experiments. Right: CAD-model of the geometry used in the simulations.

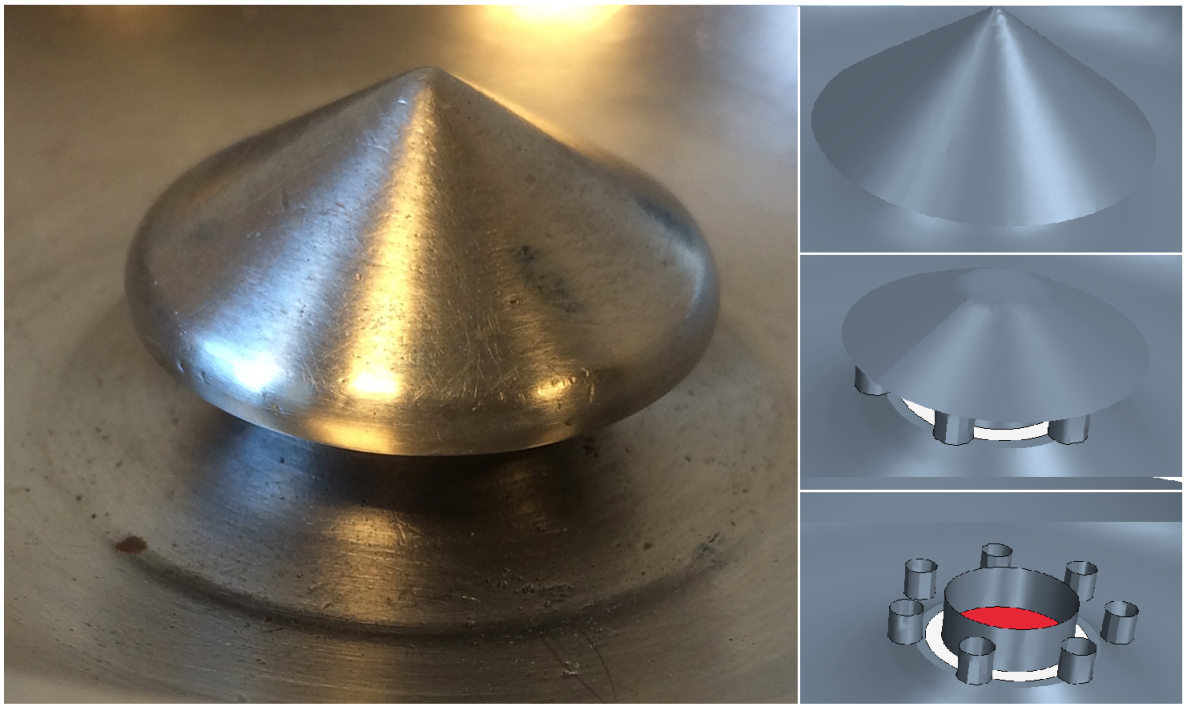

Figure 6: The dispersion device. Figure 1 also illustrates the dispersion nozzle.

## 4.2 Mesh

As mentioned earlier, Star-CCM+ has a wide range of mesh generating features. The right type of mesh needs to be selected for the domain and the geometric figures to obtain accurate numerical solutions. In this thesis the prism layer mesh and the trimmer mesh was applied to the Hartmann tube CAD-model.

The prism layer mesh generates orthogonal prismatic cells next to wall surfaces and boundaries. A prism layer is defined in terms of its thickness, the number of cell layers within it, the size distribution of the layers and the function that is used to generate the distribution. In this thesis these properties were defined globally within an automated mesh operation, but the mesh has also been defined locally around the inlet to get a better overview and solution in this special area of interest. The prism layer mesh is necessary to improve the accuracy of the flow solution. When the flow is aligned with the mesh, the numerical diffusion, i.e a discretization error that smooths the discontinuities and steep gradients, is minimized.

In addition to the prism layer mesh, the trimmer mesh was applied in this research. The trimmed cell mesh provides a robust and efficient method of producing a high-quality grid for both simple and complex mesh generation problems. The resulting mesh is composed predominantly of hexahedral cells with polyhedral cells next to the surface [29].

Volumetric refinement was used to create a finer mesh within the inlet. This customized mesh was 50 percent of base size, which means that the cells are half

the size of the base cells, which the rest of the model contains of. The base size in this thesis was set to 0.001 m and number of prism layers was equal to two. The base size of the grid cells was adjusted to get a satisfactory result, however smaller cells require a longer computational time.

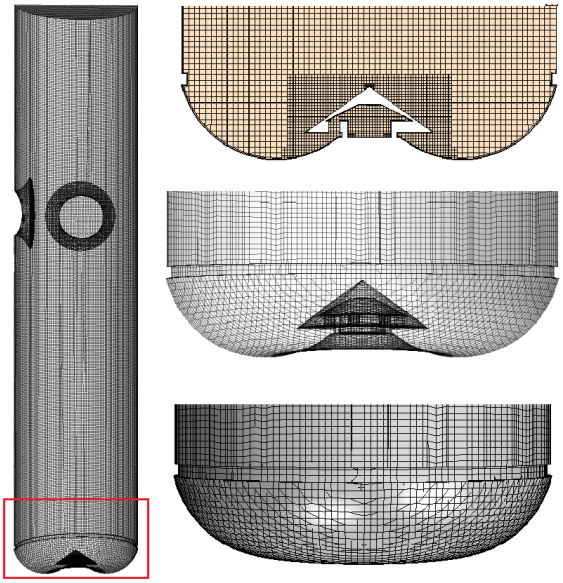

Figure 7: The total grid design. Left: surface grid of the CAD-model. On the right side the two lowest figures is the surface grid. The upper figure illustrates a cross section of the volume mesh in the bottom of the tube.

## 4.3 Initial conditions

The initial conditions in this thesis were specified as follows; the pressure was constant and equal to 0.0 Pa, the static temperature was equal to 300 K, the turbulent dissipation rate was 0.1 $m^2/s^3$ and the turbulent kinetic energy was equal to 0.001 $m^2/s^3$. The velocity was equal to zero in all the directions in the velocity field. The initial conditions were the same for every simulation, which makes the results comparable.

## 4.4 Boundary conditions

To get realistic results from the simulations, we need to specify the boundary conditions properly. The tube boundaries include outlet at the top, inlet at the bottom and the rest of the geometry is impenetrable walls.

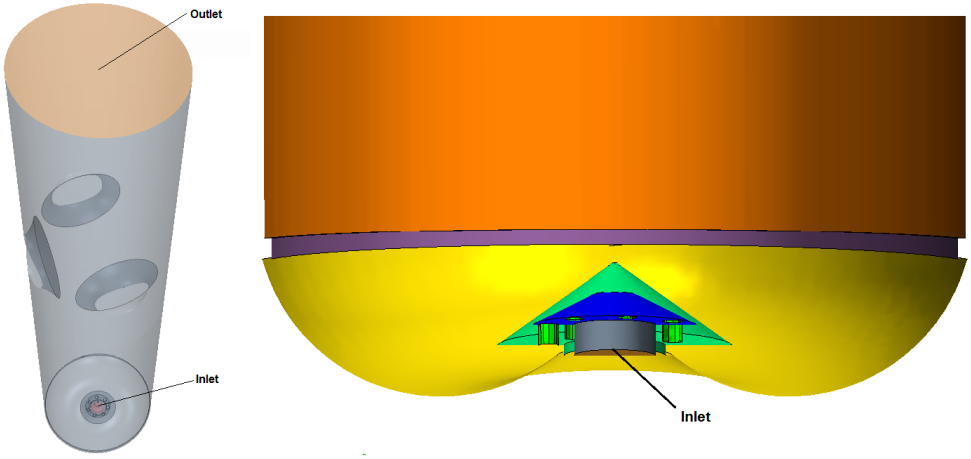


Figure 8: Outlet and inlet boundaries of the CAD-model.

At the top of the Hartmann tube the air leaves the tube unrestricted out the outlet. The boundary was set to be a pressure outlet and this prevents the pressure from building up as the air flows into the tube. To prevent the particles from being blown out of the tube a filter is placed over the outlet, the gas is still able to flow out of the tube but this may have an impact on the flow field of the gas and can influence the results of the dispersion. For the particles the outlet boundary was specified to follow a rebound model with a restitution coefficient at 0.9.

The inlet boundary where the gas flow enters the Hartmann tube was controlled by a customized field function. To get a realistic representation of the gas flow the field function was used in order to control the inlet specifications. When initiating dust dispersion in experiments using the modified Hartmann tube, a pressure pulse of gas distributes the particles, not a continuous gas flow. The customized field function made the injection of the gas follow this model: during the first 50 ms the injection velocity was 50 m/s and after this the velocity decayed with a rate of 1 m/s per 1 ms for the next 50 ms. This second period mimicked the end of the gas injection. The initial velocity was chosen to be 50 m/s because this gave results matching Christiansen [36] and Berg [37].

The rest of the tube geometry consisted of walls. More specific, no-slip walls which means that the gas obtains zero velocity near the wall boundary. For the particles the rebound model was used. The collisions between the particles and the wall are dependent on the restitution coefficient. The rebound model makes it possible to apply a proper value for this coefficient and it can be varied to explore its impact in the simulation.

## 4.5 Properties of the fluid and the particle

The continuous phase consisted of air with a molecular weight of 28.97 kg/kmol, dynamic viscosity of $1.86 \cdot 10^{-5}$ Pa s, thermal conductivity of 0.026 W/(m K),

specific heat of 1003.62 J/(kg K) and turbulent Prandtl number of 0.9. The gas was assumed to be ideal and was treated as compressible throughout the simulation. The initial static pressure inside the tube was 0.0 Pa and the initial temperature was 300.0 K.

The dispersed phase consisted of solid spherical particles of constant density of 2500 kg/m$^3$ and of a diameter of 106 $\mu$m. These properties were used as default values and corresponded to the particles used in Berg's [37] experiments, see Figure 9. The particles were placed at the bottom of the tube before the gas was injected. 306 particles were present in the tube in this research.

Figure 9: A photography of the glass beads (left) and their initial position in the Hartmann apparatus. In this thesis the number of particles was significantly smaller.

## 4.6 Turbulence models

After specifying that the viscous regime in the continuous phase consists of a turbulent flow, the Reynolds-Averaged Navier-Stokes model is automatically applied. As mentioned in section 3.3, RANS is a simplification of the Navier-Stokes equations. The simplifications have to be made because the computational time needs to be sufficiently small.

The next step is to choose which turbulence model that is going to solve the phenomena of chaotic changes in pressure and flow velocity. In this thesis the k-$\epsilon$ turbulence model is chosen. When applying the k-$\epsilon$ turbulence model both the Realizable k-$\epsilon$ Two-Layer model and the Exact Wall Distance model is automatically included and required.

The realizable k-$\epsilon$ model contains a new transport equation for the turbulent dissipation rate $\epsilon$. It also expresses a critical coefficient $C_\mu$ which is a function of mean flow and turbulence properties in stead of assuming it to be constant as in the standard model. The model combines this realizable k-$\epsilon$ model with the two-layer approach. The coefficient in the models is identical, but the model gains the added flexibility of an all y+ wall treatment.

Two-layer All y+ Wall treatment means that the layer near the wall is divided into two parts and $\epsilon$ and $\mu_t$ are specified as functions of wall distance in the layer next to the wall.

Further Exact Wall Distance is also required by the turbulence model. This model provides a parameter that represents the distance, $y$ from the cell centroid to the nearest wall with non-slip boundary condition, calculated by the wall distance solver.

For the dispersed phase the Turbulent Dispersion model describes the effect of turbulence on the solid particles. This model collaborates with the RANS turbulence model in the physics continuum. It employs a random walk technique to synthesize the fluctuating nature of the turbulent velocity field in the continuous phase. The introduction of a random element means that turbulent flows are likely to need a higher number of parcels than similar laminar flows, to provide statistically meaningful results [29].

## 4.7 Models and the solver control

The physics model applied in this simulation defines the primary variables of the simulation such as velocity, pressure and temperature. The model also defines which mathematical formulation that is used to generate the solution. In other words, the model defines how a physical phenomenon in a continuum is represented and it works together with the solvers to provide them with required equations to obtain a presentable solution.

In this research the time solver was chosen to be implicit unsteady. When this model is activated, objects that offers a choice between iteration and time-step for a trigger (such as monitors and scenes), can be set to update each time-step. It uses the implicit unsteady solver and the solvers primary function is to control the update at each physical time of the calculation and the time-step size.

The flow specification of the simulation can either be segregated or coupled. In this thesis the flow specifications followed the segregated model, which is suited for mildly compressible gas flows and requires a smaller computational time than the coupled solver. When using this solver the mathematical equations are solved in an uncoupled manner, which means they are solved sequentially. With the segregated flow algorithm the segregated fluid temperature model is activated. This model solves the total energy equation with temperature as the solved variable. Enthalpy is then computed from temperature according to the equation of state. This is only relevant if the segregated model is used for the fluid flow.

For the dispersed phase models such as drag force, virtual mass and shear lift force were chosen in addition to the turbulent dispersion model. The dispersed phase is referred to as the Lagrangian multiphase in the programme because the Eulerian-Lagrangian model is used in this thesis.

### Time-step and inner iteration

After some trials the time-step was set to $1{\cdot}10^{-4}$s and the temporal discretization was set to first order. This gave a steady gas flow and a converging solution.

When the temporal discretization is set to first order, the unsteady term uses the solution at the current time level, as well as the one from the previous time level [29]. The inner iteration was set to five with no maximal number of steps or physical time.

### 4.8 Simulation (preparations)

It is important to get a stable solution for the gas flow before introducing the particles. After the gas flow got a stable solution, particles were placed in the bottom of the tube. The number of particles depend on the area of the section plane created in the bottom (section plane coordinate z : -0.00499). If the z direction is higher, more particles are introduced into the tube. When the particles are present in the tube, the gas inlet is opened with customized specifications to get an approximately uniform mixture of particles and air.

Several simulations were performed with and without gravity force present. For both the gravity case and the zero gravity case the velocity specifications at the inlet were the same, as well as the other properties for each pair of simulations.

## 5 Results and discussion

In this section the results from the simulations are shown. Two main simulations were done; one where the particle-cloud formation occurred in normal condition ($z$=-9.81m/s$^2$), the other in a theoretical zero gravity environment ($z = 0$). The results are presented with the help of snapshots from STAR CCM+, plots and tables.

To get a better overview of the simulation process the simulation was divided into three periods, which was also necessary for comparing results with previous works from literature:

- Early dispersion: 0 ms - 50 ms
- Velocity decay: 50 ms - 100 ms
- Settling process: 100 ms - 800 ms

The dispersion process starts with particles at rest in the bottom of the Hartmann apparatus. The code requires the particles to be injected with a certain velocity and therefore the particles are not completely without motion when the gas is injected and the dispersion process starts. This might give some slightly contaminated results, nevertheless the velocities and motions are so small that they are being neglected in this thesis, as discussed later in section 5.2.

The velocity decay is the next step in the simulation. After a given solution time, the inlet velocity of the gas starts to decrease controlled by a field function as

mentioned earlier.

The final step is the settling process. After the decay of velocity the particles will be affected by the gravitational force, which results in sedimentation. One of the main reasons and topics for this thesis is to investigate how the particle cloud will behave without the gravity force, and it is in this part of the simulation the results are expected to be important.

## 5.1 Gas flow

Because the system investigated in this thesis is a dilute multiphase flow with one way coupling, the gas flow strongly influences the particle motion. To understand the particle motion, this section provides an overview over the velocity (m/s) and pressure (Pa) distribution of the gas and the turbulent kinetic energy ($m^2/s^2$) development in each period of the simulation.

### 5.1.1 Velocity

The whole process starts when the gas is injected through the inlet boundary and distributed by the nozzles. After entering the tube the air flows upwards and out of the outlet at the top of the tube with just a minor interruption. For both the gravity case and the zero gravity case the velocity profile follows the same pattern through the simulation. The velocity profile evolves as shown in Figure 10 where the periods in which the process is divided are marked. To get a better understanding and visualization of the velocity field and velocity distribution, Figures 11-13 show gas streamlines and a vector field of the gas velocity.

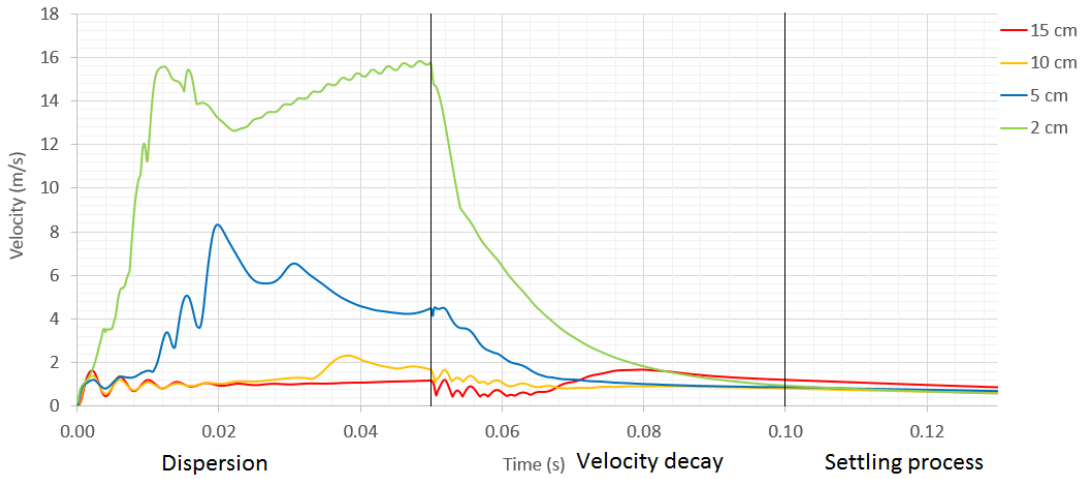


Figure 10: Velocity profile as a function of time from line probe monitors at different heights above the nozzle. The black vertical lines separate the periods of the simulation.

### Dispersion

The dispersion process begins when the gas flow is initiated and flows out of the dispersion nozzles. As long as the gas is initiated with a constant velocity the streamlines follow the same pattern at the bottom of the tube and around the injection zone (Figure 11b). The streamlines in Figure 11a immediately start to create vortices. Figure 12c shows the vector field that confirms the streamline field. The vortices at the bottom of the tube create a lifting effect on the particles. As the magnitude of the velocity increases the vortices becomes larger to a maximum size of about 7 cm in diameter (Figure 12a and b). The vector velocity field of the gas shown in Figure 12c, illustrates how the vortices climb up against the wall in the tube.

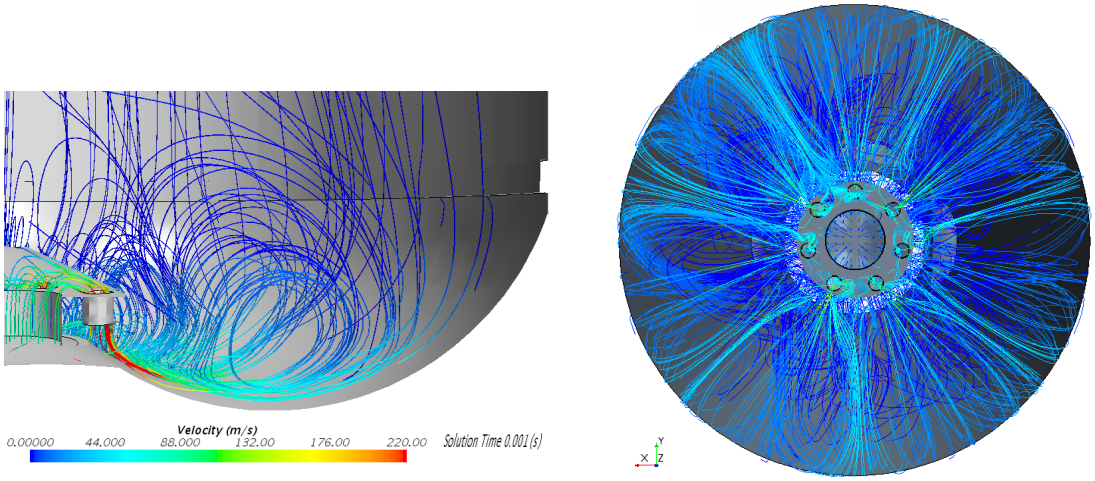


(a) (b)

Figure 11: (a) Streamline distribution of gas. The nozzle is shown at the left and the bottom of the tube is at the right. (b) Gas distribution shown from the bottom of the tube (50 ms and 50 m/s).

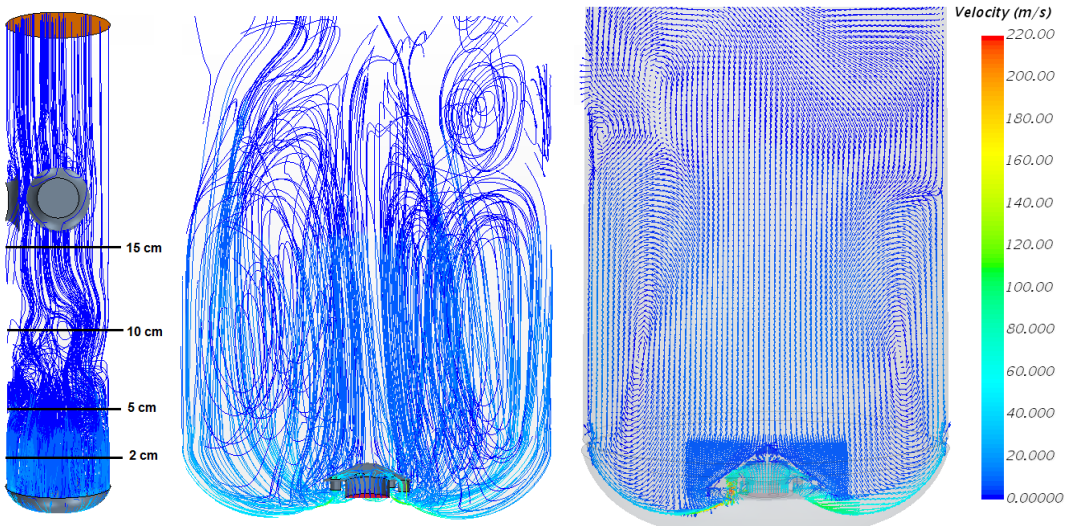


(a) (b) (c)

Figure 12: Visualization of the velocity field after the dispersion process (after 50 ms); (a) the whole tube, (b) streamlines at the lowermost 8 cm and (c) the gas velocity vector field at the lowermost 8 cm.

The evolution of the velocity magnitude as a function of time is shown in Figures 10 and 13. With an initial and constant velocity of 50 m/s during the dispersion process, the velocity magnitude reaches a maximum of 16 m/s. If measured 2 cm above the inlet nozzle the velocity decreases as it flows upwards in the tube. Figure 10 states that the velocity magnitude measured inside the tube never reaches values above 16 m/s, even though the snapshots from the scaler velocity field show values up to 220 m/s inside the nozzle (Figure 13). This reveals that the dust deposit is subject to significant gas velocities and this has not been reported in research literature yet.

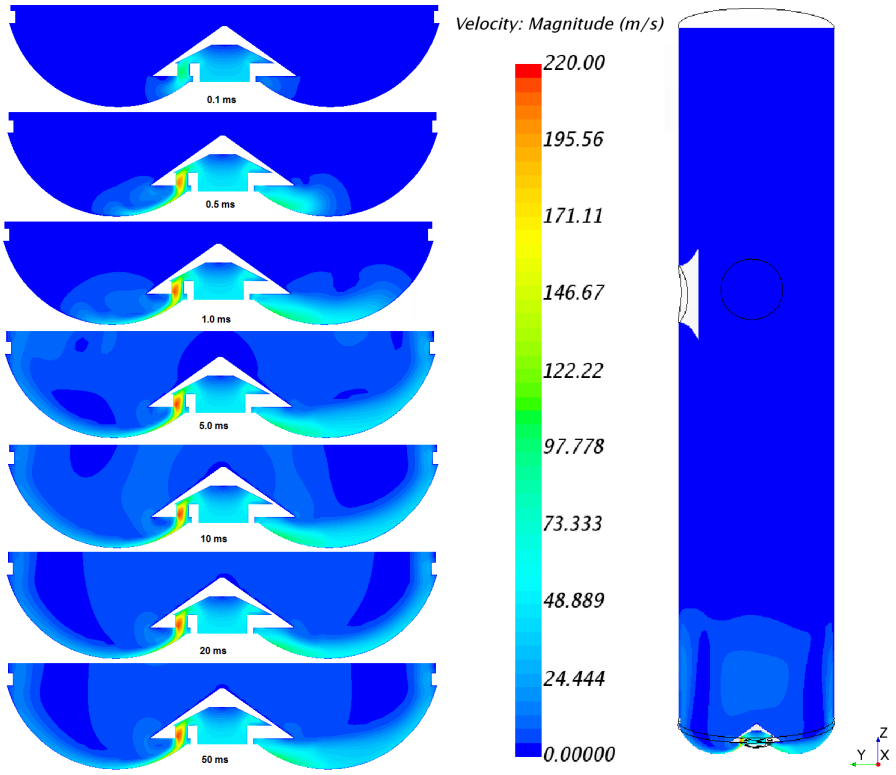


Figure 13: Left: vertical cross-section of the velocity magnitude distribution around the nozzle at different points in time during the dispersion process (0-50 ms). Right: a full view of the tube at 50 ms.

A snapshot of the velocity distribution in a horizontal cross-section after 50 ms is shown in Figure 14a and b. The inhomogeneous velocity distribution formed due to the location of the seven inlet nozzles may affect the dispersion of the particles. Figure 14 shows the results compared with a simulation done by Christiansen [36]. The figure shows clear similarities when using the Eulerian-Lagrangian approach and 50 m/s as inlet velocity in the dispersion process. Compared to the streamlines in Figure 11b it makes sense that the velocity is higher where the nozzles are located also 5 cm above the nozzles.

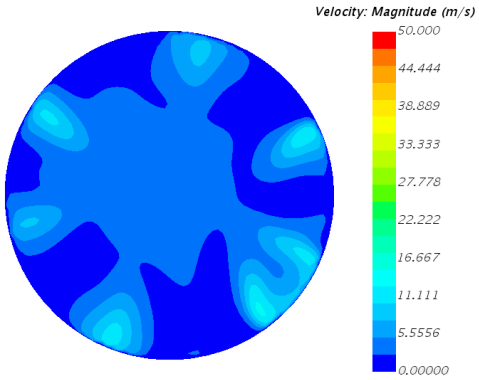


(a) 5 cm above inlet nozzle

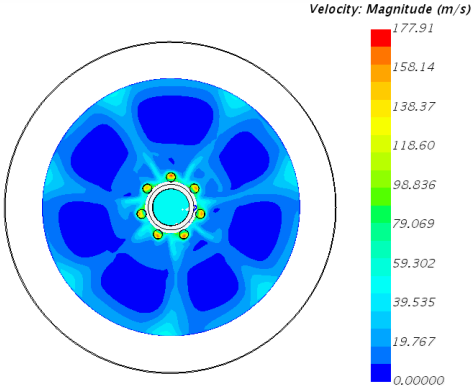


(b) Below inlet nozzle (1 mm).

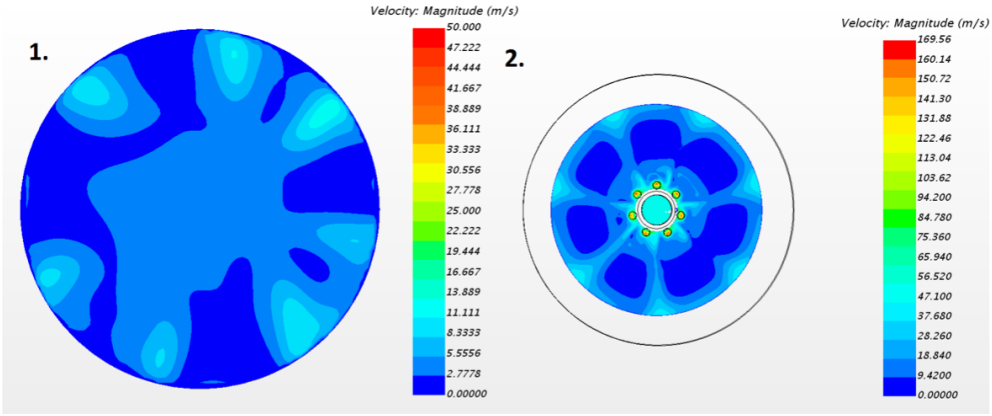


(c) 1. 5 cm above nozzle, 2. below the nozzle [36].

Figure 14: Horizontal cross-section of the velocity distribution of air after ((a), (b)) 50 ms with 50 m/s constant inlet velocity and (c) after 100 ms with 50 m/s constant inlet velocity [36].

On the other hand, research done by Dalstø [38] shows a much more circular shape on the velocity distribution when using the same Hartmann model. The Hartmann tube used by Murillo et al. [24] is slightly different from the one used in this thesis, as well as by Christiansen [36] and Dalstø [38]. The tube used by Murillo et al. had a square shape and a cross section of $0.07 \times 0.07$m. It was not clearly stated which type of inlet nozzle that was used, but the velocity distribution in a horizontal cross-section of the tube after 60 ms shown i Figure 15c has some similarities with the simulations done by Dalstø. Dalstø used the Eulerian-Eulerian approach and measured the air velocity with a dust layer present in the tube, and Figure 15a and b shows the velocity field after 10 ms of dispersion. Murillo [24], on the other hand, used the Eulerian-Lagrangian approach also with a dust layer present in the tube. The results indicate that it might not be the simulation method or the nozzle type that leads to the different velocity distribution. The only common factor for Dalstø [38] and Murillo et al. [24] is the dust layer present in the tube. The velocity distribution illustrated in Figure 14 corresponds namely no dust layer present in the tube.

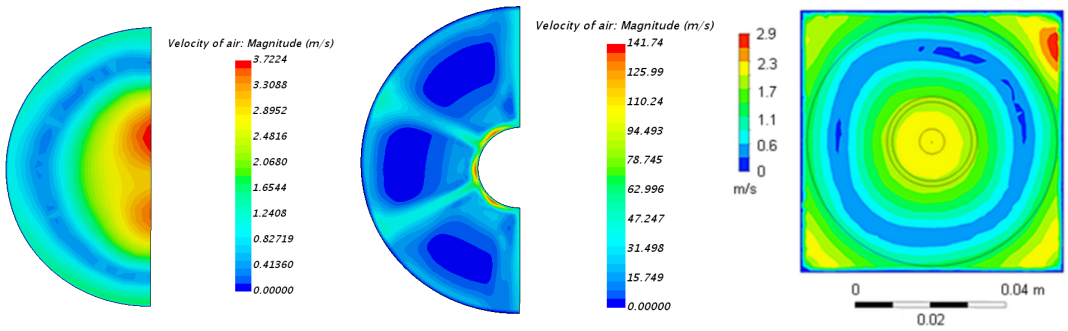


(a) (b) (c)

Figure 15: Horizontal cross-section of the velocity distribution of air; (a) 5 cm above nozzle after 60 ms [38], (b) below inlet nozzle after 60 ms [38] and (c) approximately 5 cm above inlet nozzle after 10 ms [24].

### Velocity decay

For the particles motion to be only dependent on the gravitational force and not the currents of the gas, the velocity needs to decay. In a experimental setting the gas is injected with a pressure pulse or an air jet. This does not lead to a constant inlet velocity and to get a realistic result of the simulation the initial gas velocity needs to decay with time, as mentioned earlier. The velocity specifications in the simulation is evident in Figure 10 where the velocity clearly drops after the dispersion process. It keeps on decreasing until it reaches a stable value below 0.7-1.2 m/s. The differences between velocities in different heights above the nozzles disappear after 80 ms and after 100 ms there is no more injection of gas at the inlet. Figure 16 shows how the flow field inside the tube drastically changes when the decay of velocity starts. Also this period is not affected by particles present or the gravitational field.

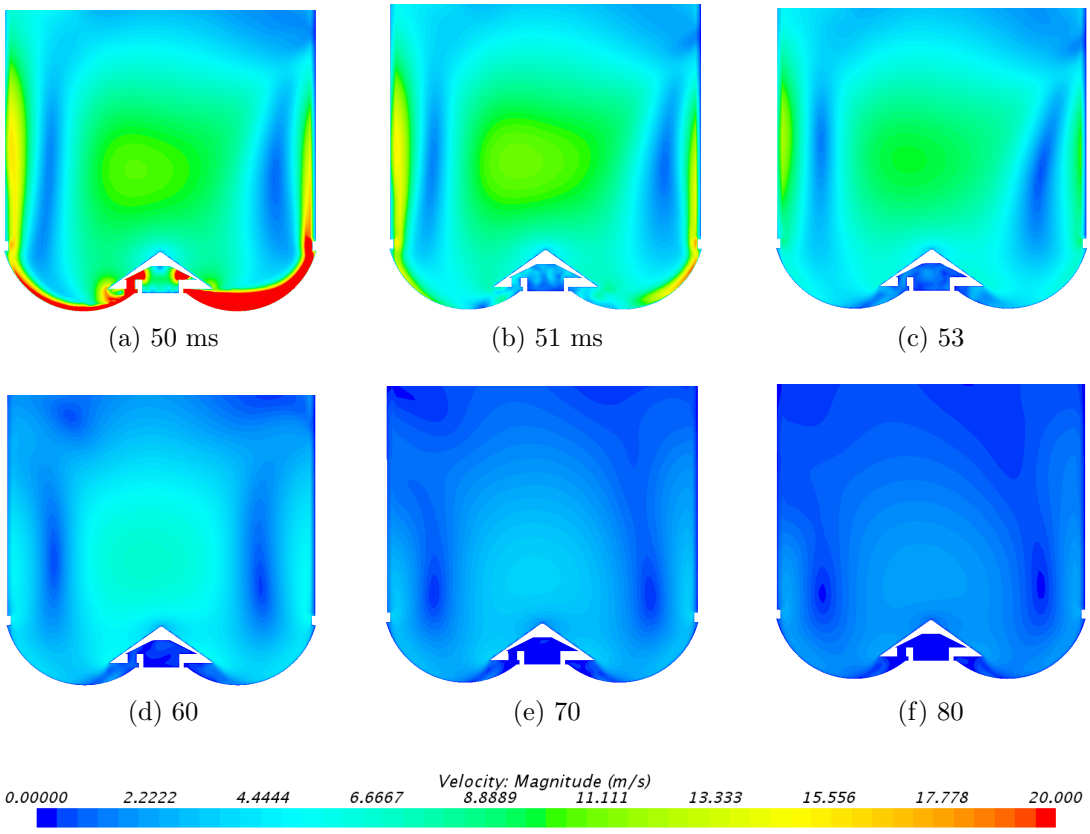


(a) 50 ms (b) 51 ms (c) 53

(d) 60 (e) 70 (f) 80

(g) Color Bar

Figure 16: Velocity of air in the velocity decay period. The red area in (a) corresponds to velocities between 20 and 100 m/s, which is at the boundary between the different periods. Compare with Figure 13 to see the gas velocity field with a different color bar.

### Settling process

In the settling period the velocity field gradually decays, see Figure 10. This is the process that takes the longest simulation time of all the periods, 100 ms to 900 ms. One of the reasons for the long simulation time for the settling process is the small size of the particles, and only small gas velocities keep them flowing around. Figure 17 shows a snapshot of the gas flow distribution in the bottom of the tube after 900 ms. The values of the color bar vary between 0.0-0.14 m/s.

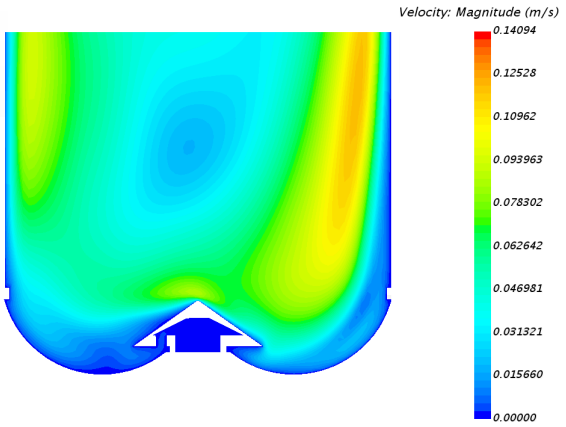


Figure 17: Snapshot of the gas velocity scalar field after 900 ms, end of the simulation.

### 5.1.2 Pressure

#### Pressure drop

When the gas is injected a pressure gradient between the inlet and the outlet forms. The pressure drop reaches a point in time where it stabilizes. This is after approximately 20 ms on a value of 36 500 Pa. This corresponds to the results achieved by Christiansen [36].

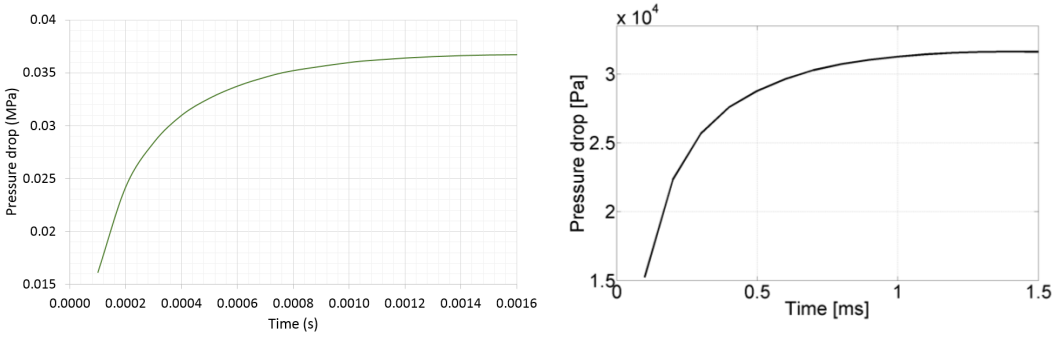


(a) (b)

Figure 18: (a) Absolute pressure drop as a function of time with a constant gas injection velocity of 50 m/s the first 1.5 ms and (b) analogous results obtained by Christiansen [36].

After the pressure drop has reached a stable value of 36 500 Pa the pressure drop does not change during the dispersion process. Figure 19 shows a drastic drop when the simulation time reaches 50 ms and the decay process is initiated. As the velocity decays, the pressure drop again starts to stabilize. When the settling process starts there is no noticeable change. This means that there is

no pressure drop when the velocity is not changed, which correspond to theoretical assumptions that there is no pressure gradient between the inlet and the outlet.

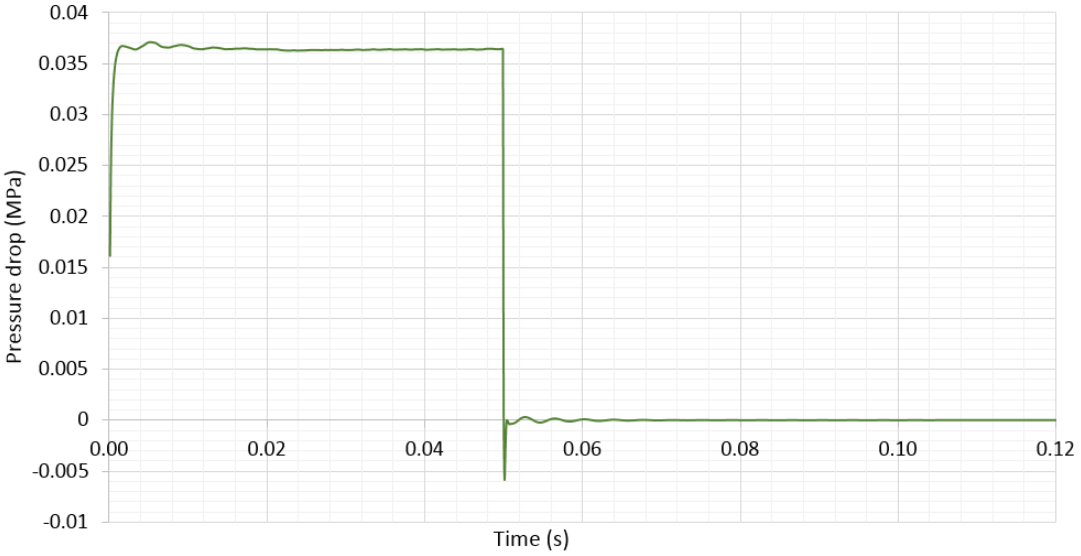


Figure 19: History of pressure drop during the whole simulation process.

### Absolute pressure

The pressure distribution in the tube is influenced by the changes in the injection velocity of gas. Figure 20 shows how the pressure changes with time at different heights above the injection nozzles. At the beginning of the simulation the pressure oscillates with smaller and smaller extremes until it starts to stabilize at 101 325 (Pa). It never gets completely stable until it again starts oscillating, similar to the beginning. The oscillation shown in Figure 20 is a representation of how the program solves the equations and manages to get a stable solution and a value of the absolute pressure in the tube. When the gas velocity is changed, the program again starts to iterate to a stable solution. This matches the injection characteristics of the gas velocity.

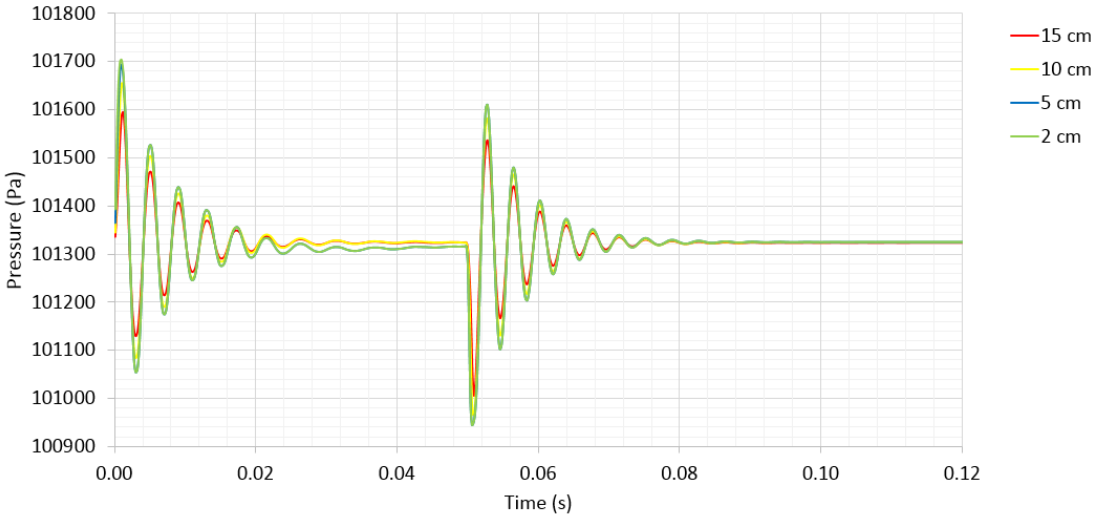


Figure 20: Absolute pressure as a function of time at different monitor lines above the nozzle.

As is true for the velocity, the pressure is also independent of the present particles and the gravitational force. The absolute pressure profile shown in Figure 20 has therefore the exactly same shape for all the cases. This correlates with expectations and physical laws.

In Figures 21, 22 and 23, snapshots of the pressure distribution are shown at different time steps and in different perspectives. The low pressure occurs inside one of the gas outlets in the nozzle. This is due to the high gas velocity in this region according to the Bernoulli's equation (confirmed in Figures 10 and 13).

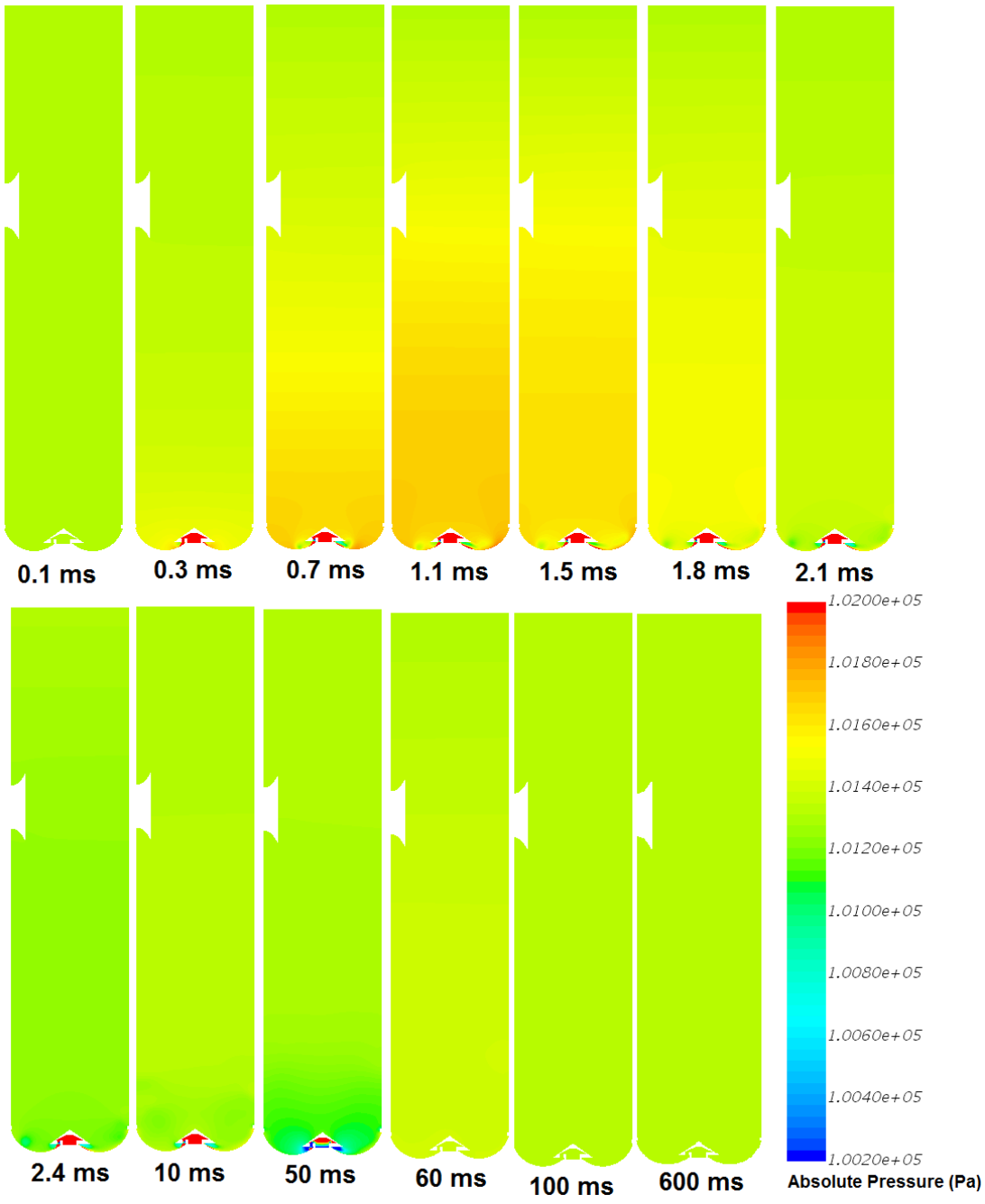


Figure 21: Snapshots of absolute pressure distribution at different points in time illustrating the pressure wave and how the pressure stabilizes after the dispersion process.

Through the three periods of this simulation the pressure in the tube follows the injection variations as mentioned above. Snapshots from the scalar field developed at the bottom of the tube show how the pressure varies in time with position relative to the nozzle.

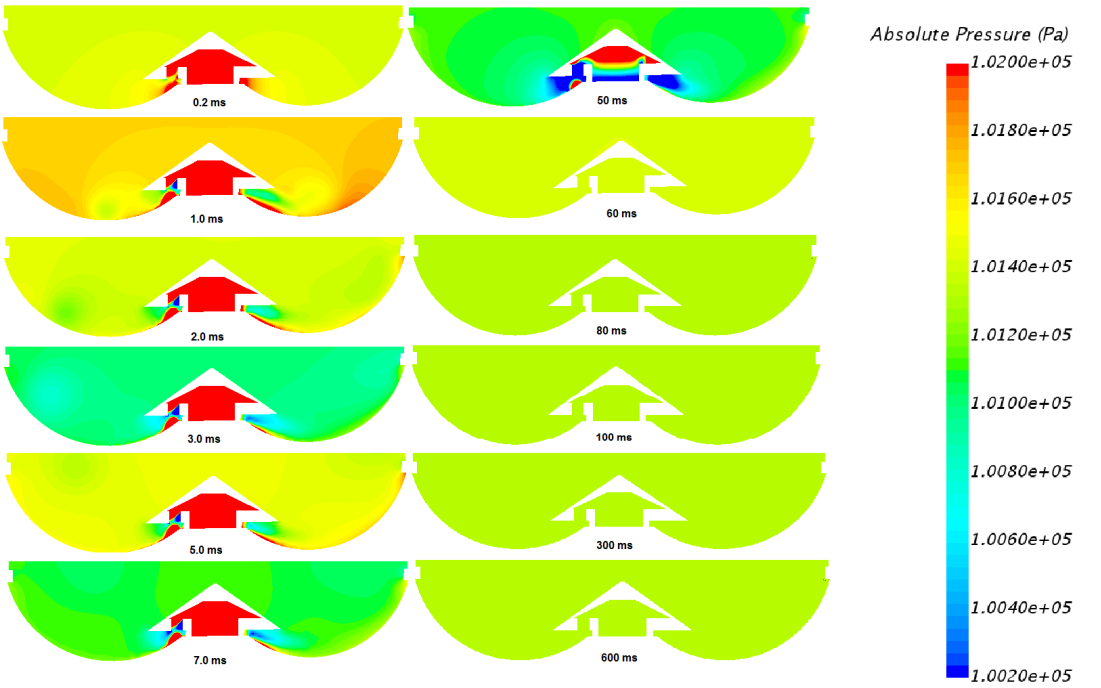


Figure 22: Snapshots of the absolute pressure distribution at the bottom of the tube at different periods of the process.

Figure 23 shows the pressure distribution at the bottom of the tube, compared with results from Christiansen's [36] research. the results are matching, the scalar fields show the same pattern, where a higher pressure is located between the injection nozzles.

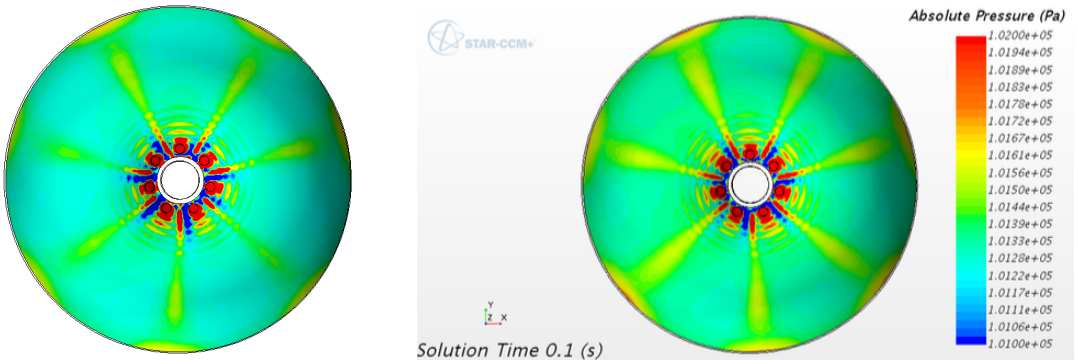


(a) (b)

Figure 23: Absolute pressure distribution at the bottom of the tube after the gas injection with constant velocity of 50 m/s; (a) after 50 ms and (b) after 100 ms [36].

### 5.1.3 Turbulent kinetic energy

The evolution of turbulent kinetic energy at different heights through the three stages in the simulation process is shown in Figure 24. It is important to monitor the turbulence level in the tube to later examine how it influences the particles motion both in normal gravity and with zero gravity condition. As for the velocity magnitude, the turbulent kinetic energy has the largest value 2 cm above the nozzles.

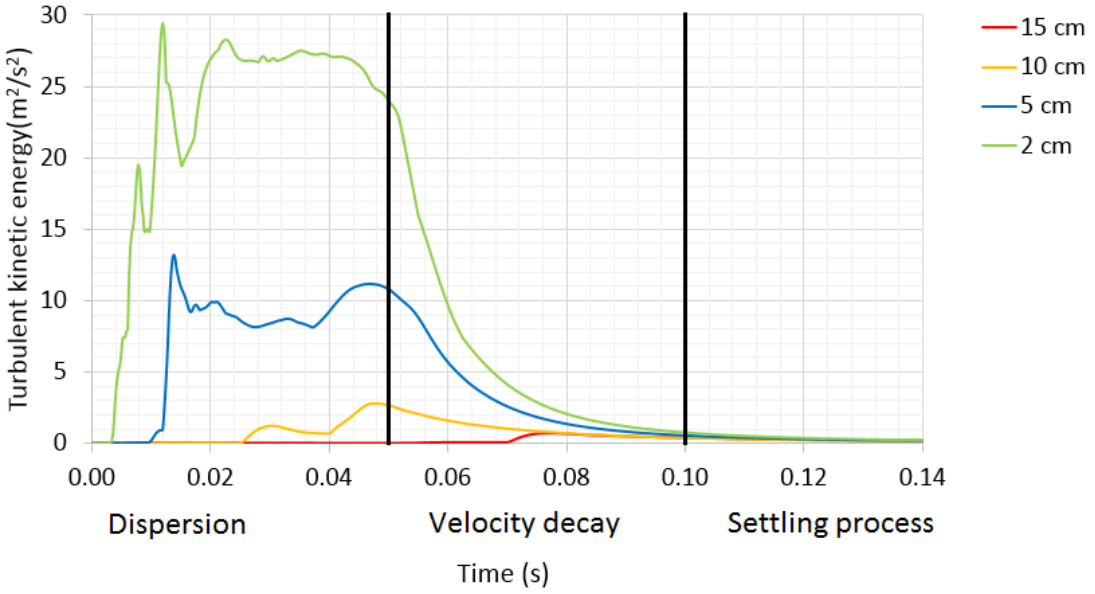


Figure 24: Evolution of the turbulent kinetic energy as a function of time at different heights above the nozzle with gas injection velocity of 50 m/s during the first 50 ms.

Both Murillo et al. [23] and Christiansen [36] investigated the turbulent kinetic energy distribution with time in the Hartmann tube. Christiansen used a constant gas velocity of 50 m/s and Murillo et al. used an injection pressure between 3-7 bar. When comparing the results, Christiansen achieved significantly lower values. Although the maximum values of this research correlates with Murillo et al., the differences between turbulent kinetic energy values measured at different monitor points are significantly larger. Nevertheless, in this research, the dispersion process was relatively short. This might be one of the reasons why the history of the turbulent kinetic energy looks differently.

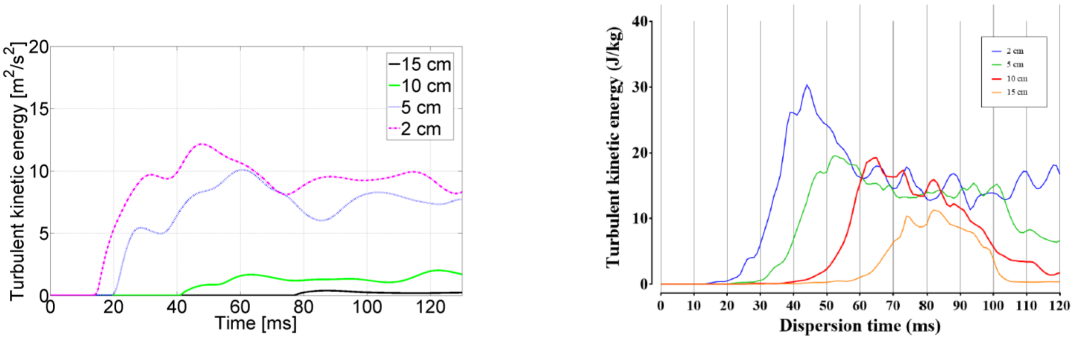


(a) (b)

Figure 25: Evolution of the turbulent kinetic energy with time; (a) results achieved by Christiansen [36] and (b) Murillo et al. [23](J/kg = $m^2/s^2$).

After the dispersion process the turbulent kinetic energy correlates with the gas velocity and decreases as the inlet velocity decreases. After 100 ms there is approximately no turbulence field in the tube. Figure 24 shows how the turbulent kinetic energy stabilizes under the dispersion process, decreases when the gas injection velocity decreases and reaches zero when there is no more injection. Snapshots of a horizontal view of the bottom of the tube (Figure 26) show how the turbulent kinetic energy rapidly increases and decreases as the injection of the gas is initiated and decays. The snapshots at the top show a fast increase the first 5 ms and how it stabilizes when the gas injection is kept constant. The bottom row of snapshots show an extremely fast decrease as the gas injection properties change. It only takes approximate 0.5 ms after the dispersion process for the turbulent kinetic energy values to decrease to values under 180 $m^2/s^2$. When comparing the stable value achieved during the dispersion process with Christiansen (Figure 27) the results correlate, even though Figure 27 shows some differences..

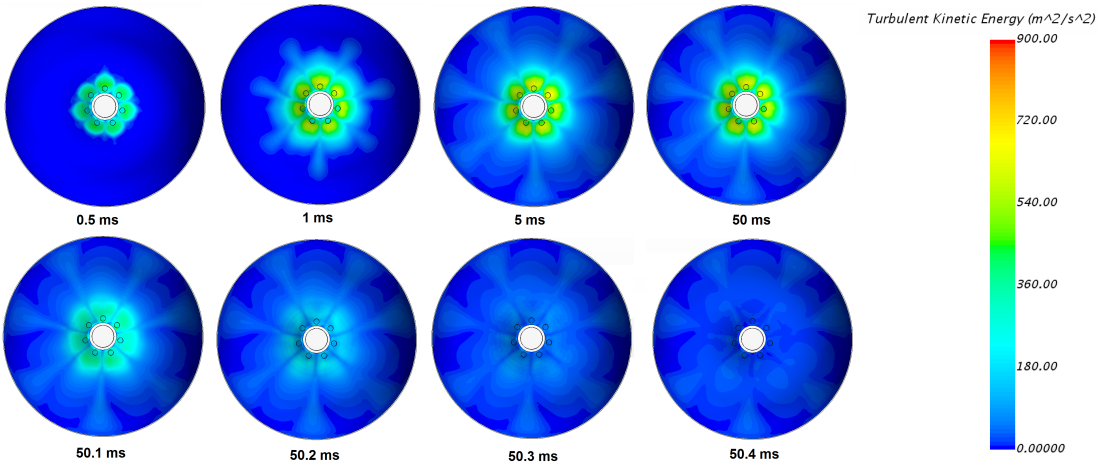


(a) (b)

Figure 26: Evolution of the turbulent kinetic energy with time. Snapshots of the scalar field at the bottom of the tube.

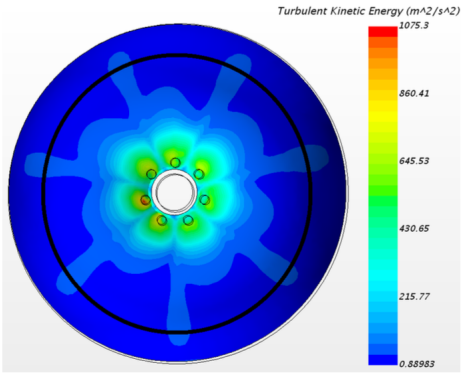


Figure 27: Distribution of the turbulent kinetic energy in the bottom of the tube. View from above. At time step 100 ms [36].

## 5.2 The movement of the particles

When analysing such a relatively large system of 306 elements affected by gas flow velocity and other parameters, it is necessary to divide the simulation into smaller periods for a better understanding of the particles movement. The following periods have been made in addition to the aforementioned gas injection periods (dispersion, decay of velocity and settling process):

1. Initial particle position
2. Initiation of the particle movement
3. The particles enter the column
4. Particles in a steady dust cloud

5. Particle settling

This section gives a general description of the movement of the particles in the modified Hartmann tube. The results in general are presented in the form of graphs and snapshots from the simulations. When using the Eulerian-Lagrangian approach it is possible to see the motion and position of each single particle present as a function of time. Nevertheless, this constitutes a huge amount of data and therefore the focus in this thesis is mostly on the particle that have reached the maximum and minimum position in the vertical direction and the particle with the highest velocity.

### 1. Initial particle position

When performing a dust cloud experiment, the particles are placed at the bottom of the Hartmann tube before dispersion. In this thesis the particles are injected into the tube through the bottom of the tube to locate them in the right position. After the particle injection the particle injector was closed and not used again in a simulation. Figure 28 shows the initial particle position at the bottom of the Hartmann tube with velocity vector arrows. The color of the particle and arrow shows the velocity of the particle. The velocity is not zero because of the injection process. Figure 28 shows how the velocity vectors are pointing upwards. This velocity magnitude is so small compared to the gas injection velocity and therefore can be safely neglected.

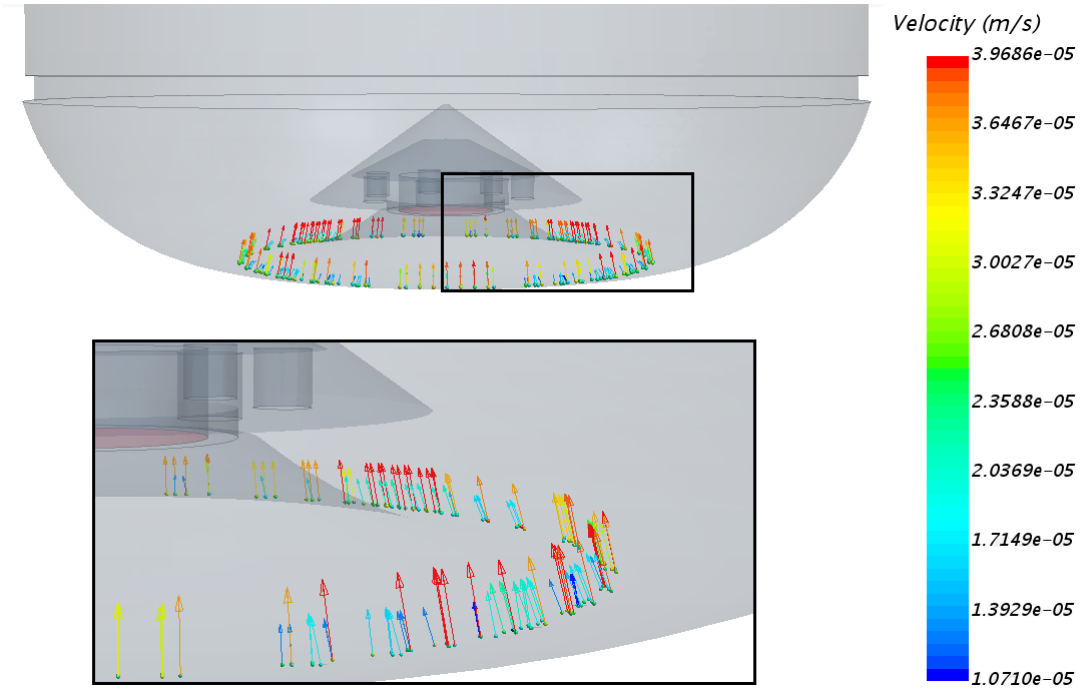


Figure 28: Initial position and velocity vector of the particles after 0.1 ms, before the gas injection was initiated.

### 2. Initiation of the particle movement

When the gas injection is initiated the particles start to move along the gas velocity streamlines. Figure 31 show particle tracks for each particle in a part for the tube the first 22 ms. There is a clear connection between the velocity field distribution and the movement of the particles. The particles follow the tube wall in a flower formation (Figure 29a) similar to the turbulent kinetic energy snapshots in Figure 26. The particle tracks in Figure 29b show how the particles flow along the tube bottom. The purple and pink part on the longest lines illustrates where the injection nozzles are located, this is because that is where the highest gas velocity exists and the particles have travelled most.

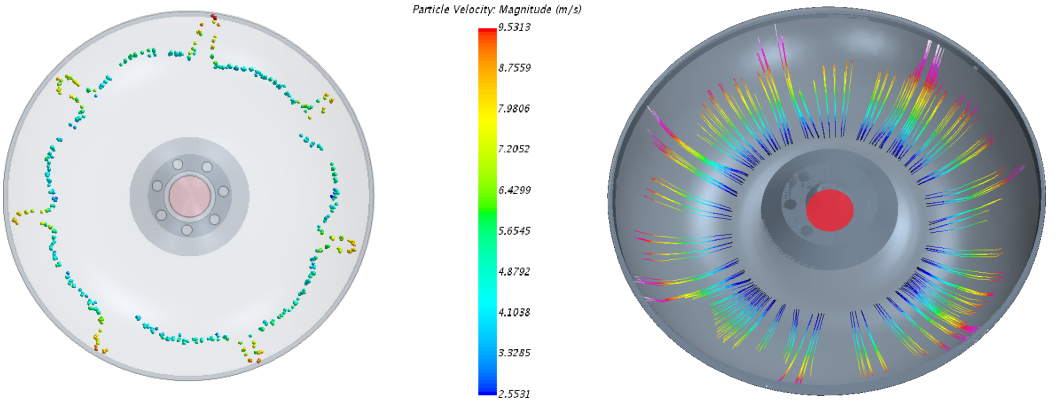


(a) (b)

Figure 29: (a) particle position and velocity after 4 ms. (b) Particle tracks the first 6.5 ms. The color differences represent the particle position.

The maximum particle velocity distribution is shown in Figure 30. The velocity is a measure of the highest particle velocity achieved by the particle cloud. During the first 0.3 ms the particles accelerate to a maximum velocity of 10.5 m/s before the velocity clearly drop to under 4 m/s and then again accelerate. After the dispersion process the particle maximum velocity drops as a result of the gas injection settings.

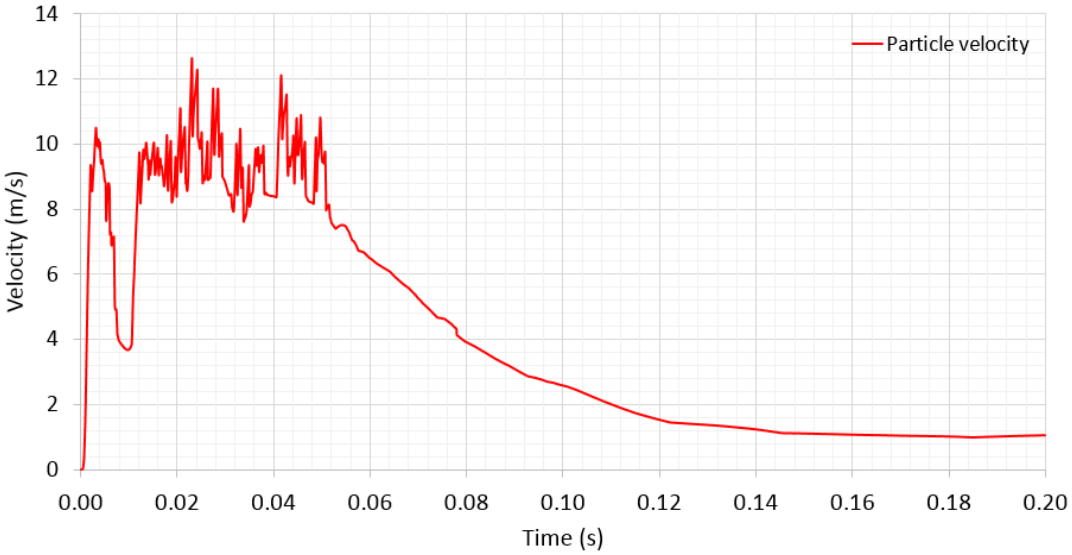


Figure 30: Particle velocity as a function of time through the first 200 ms of the simulation.

Christiansen [36] used the Eulerian-Lagrangian approach to investigate the dispersion of one single particle in the modified Hartmann tube. When looking at a bigger system of 306 particles the trajectories and track lines show several particle trails, but as in Christiansen's research, the particles start to move 0.5 ms after the gas injection was initiated. Figures 29 and 31 show the particles behaviour at the beginning of the dispersion process (after 22 ms). It is important to note that each line in Figure 31 represents one single particle movement. The figure has the same notation as Christiansen [36]: CB refers to collision with the bottom, CRS to collision with the rubber seal and CBD to collision with the bottom after the downward movement.

After the particles start to move they collide several times with the wall before reaching the rubber seal. This does not have any significant effect on the movement and velocity of the particles. When the particles reach the rubber seal, they change directions. There are two main scenarios that occur. The first shown as the black track in Figure 31 correlates with Christiansen's results (Figure 32). This particle group bounces off the rubber seal and collides with the bottom of the tube before starting to accelerate along the bottom again. There are different sizes of the loops before they again get accelerated by the gas flow. However, the other group of particles swirl upward in big arches and enter the column of the tube after reaching the rubber seal.

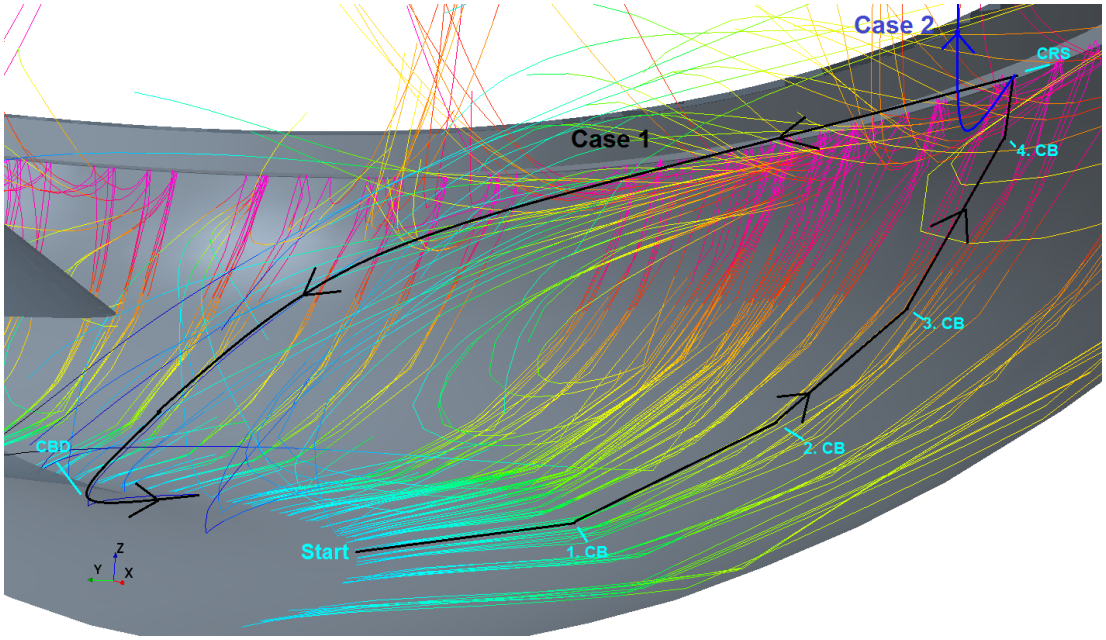


Figure 31: Trajectory of the particle movement the first 22 ms.

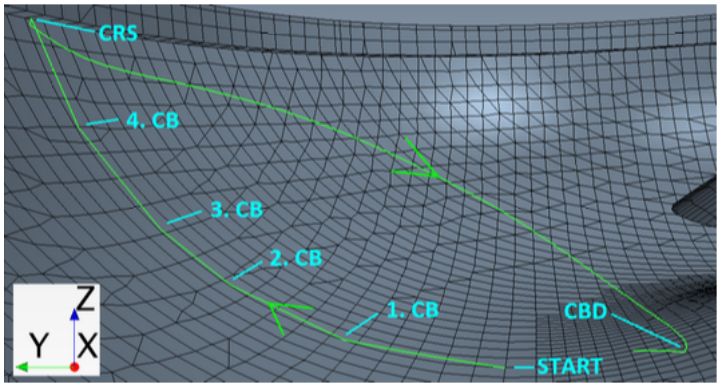


Figure 32: Particle trajectory the first 30 ms [36].

### 3. The particles enter the column

As the pressure wave distributes the particles the average velocity starts to stabilize. The particles continue to flow upward and are dispersed into the tube with the help of the gas velocity field. After colliding with the rubber seal and following case 1 or case 2 (see Figure 31), the particles enter the column in a non-uniform way. The different particle positions are strongly influenced by the physical conditions of the gas flow. The color of the particle tracks in Figure 33 illustrates the position of each particle with time.

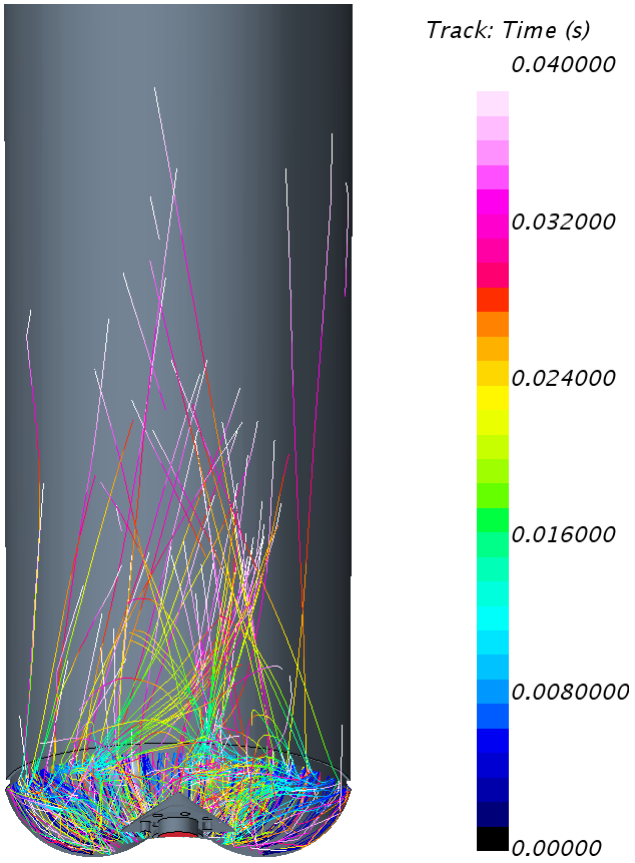


Figure 33: Particle tracks after 40 ms.

After 40 ms the particles are strongly influenced by the physical conditions of the flow. Figure 34 shows the maximum and minimum particle position as a function of time, this means the position of the highest and lowest particle present in the tube. The reason why the position in z-direction is negative is because the position representing level zero is located at the inlet nozzle and not the bottom of the tube geometry. Figure 34a show how the particles start to move at the bottom of the tube and get lifted by the gas. After 40 ms the highest particle is located 15.7 cm above the dispersion nozzle. The particle position continues to increase before it collides with the filter at the outlet. Figure 34b show that the particle with minimum position never leaves the bottom of the tube.

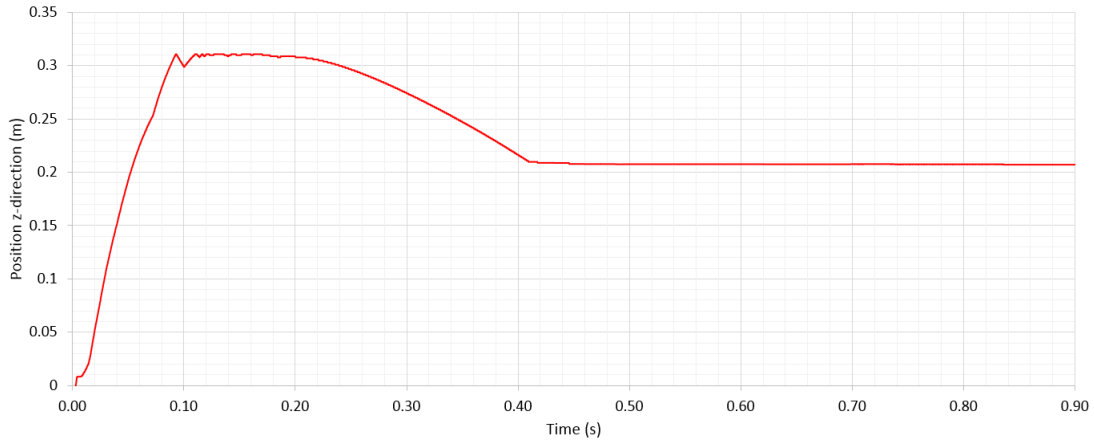


(a)

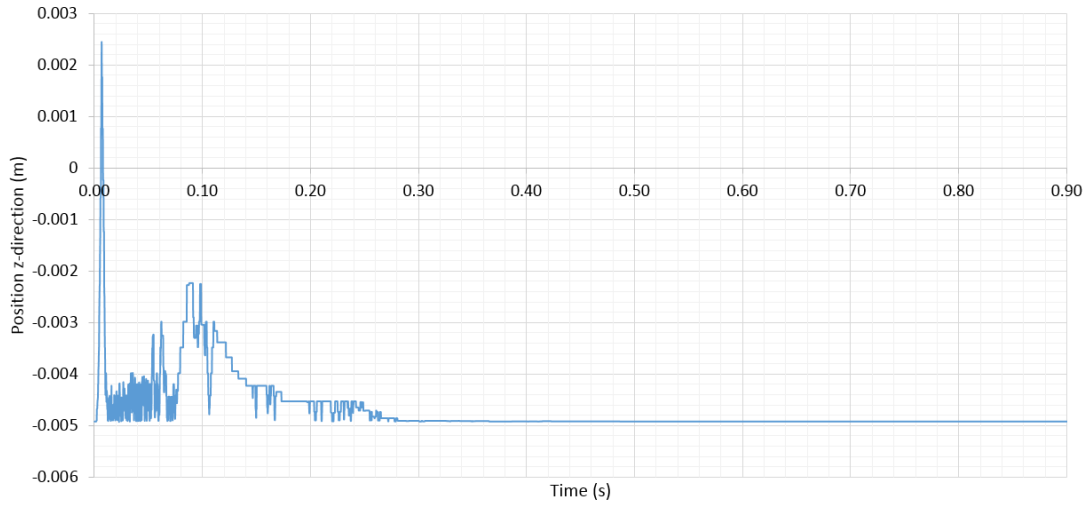


(b)

Figure 34: Particle position in z-direction as a function of time in normal condition; (a) maximum particle position and (b) minimum particle position.

## 4. Particles in a steady dust cloud

After the dispersion process, i.e. after the first 50 ms, the particle velocity starts to drop along with the gas velocity present in the tube, see Figures 10 and 30. Even though the gas injection velocity starts to decrease, it is still large enough to influence the particles and keep them in dispersion. The particles continue to form an approximately uniform dust cloud for at least 250 ms (Figure 35) which is a relatively short period of time.

Even though the particles start to settle the dust cloud could still be explosive. It is the air-fuel ratio that decides this. Distribution of particles and the question about whether the dust cloud generated could be explosive or not, is investigated later in this section.


Figure 35: Dust cloud in gas, approximately uniform dispersion.

## 5. Particle settling

When the velocity decays the gas flow fluctuations disappear and the particles are no longer able to stay in suspension. Now the gravitational force is the strongest external force, which causes the particles to settle and the dust cloud no longer represents a combustible dust cloud. As the particles settle some of them get stuck to the ignition electrode geometry at the tube wall. Figure 36 shows the particle position at the end of the simulation. The majority of particles settle to the bottom of the tube as the gravitational force overpowers the gas velocity field present in the Hartmann tube. Unfortunately, the particles that are stuck in the ignition zone affect the particle position data because the monitors measure the maximum position of the particles. In addition, some particles settle at the rubber seal close to the bottom. Because of this problem Figure 34a flattens at the position 0.20 m in z-directions for some cases.

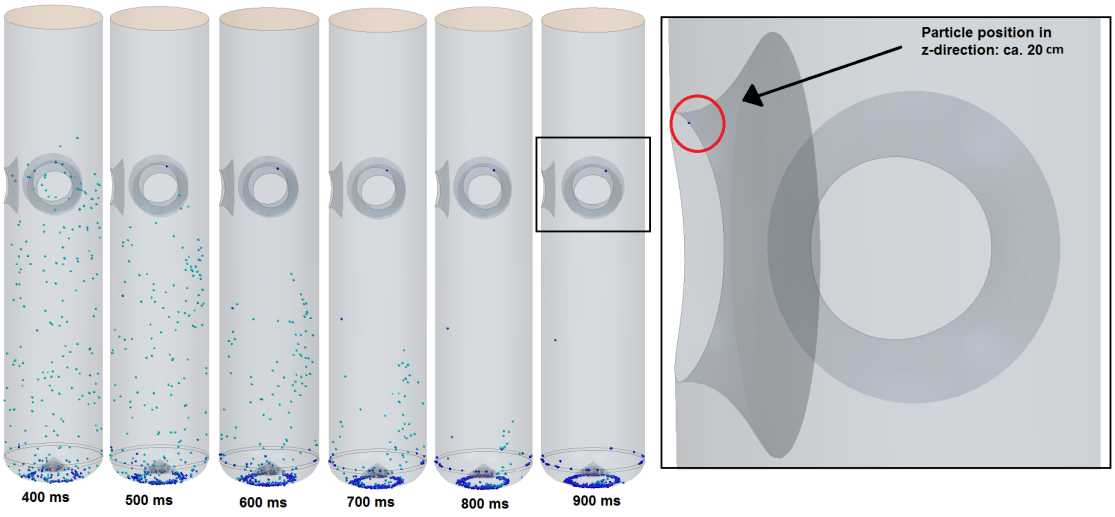


Figure 36: Snapshot of particle distribution in the tube during the settling process. At the right the picture is rotated 45 degrees.

In the simulation without gravity there is no settling process and if the zero gravity condition can represent an "ideal" condition for dust-cloud explosion experiments, the particle should stay in suspension after the decay of turbulence. Figure 37a illustrates how the maximum particle position is at the top of the tube for a lot longer time than in normal condition. The particles have approximately no velocity, stay in suspension and form a uniform and might form a combustible dust cloud even though the velocity field in the tube has decayed.

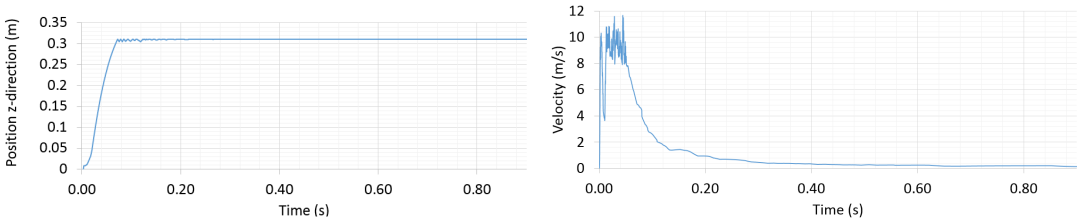


(a) (b)

Figure 37: Particle movement characteristics in zero gravity condition; (a) maximum particle position as a function of time and (b) maximum particle velocity as a function of time.

## 5.3 Volume fraction

The movement of the particles can also be investigated with the help of horizontal monitors, that measure the volume fraction of particles passing through the planes as a function of time. This illustrates how the particles are distributed in the tube in all the three periods of the simulation process. After the dispersion process the particles should form an explosive dust cloud in air. Already after 100 ms the cloud is approximately in a steady state as illustrated in Figure 38b. The particles stay in suspension for about 250 ms as mentioned earlier and Figure 38a confirms this by showing an even particle distribution through the different monitor planes in the tube. Figure 38 shows the monitor planes in the Hartmann tube and the particle distribution after 100 ms (b) and 200 ms (a).

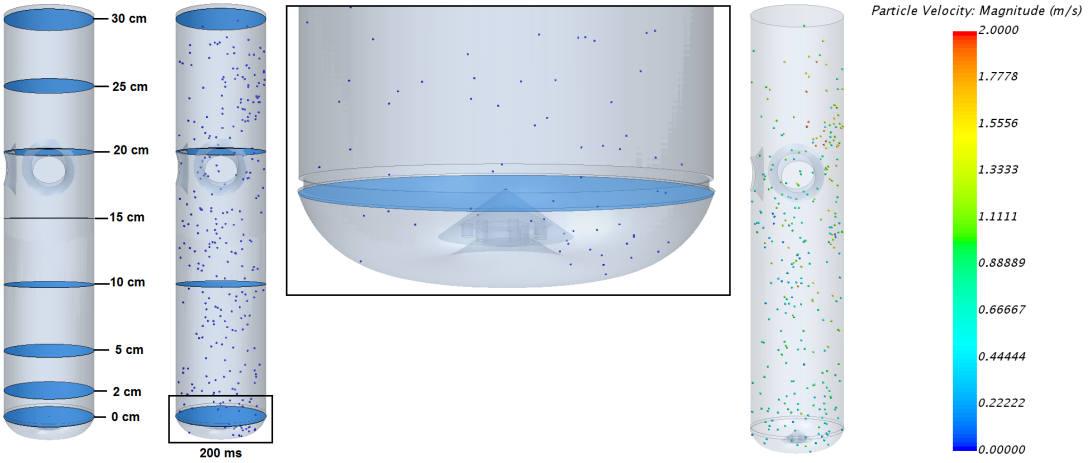


(a) (b) 100 ms

Figure 38: (a) Left: Hartmann tube with horizontal monitor planes measuring volume fraction of particles. Middle: Hartmann tube with the monitor planes used for the volume fraction plots and with the particles in suspension after 200 ms. Right: Closeup of the monitor present 0 cm above the nozzle; (b) particle velocity and position after 100 ms.

After 100 ms there is no more gas injection in the tube and the gravity slowly starts to affect the particle position. The measured volume fraction at different heights above the injection nozzle is presented in Figure 39. The figure illustrates how parcels of particles move through the Hartmann tube as the turbulent field in the tube rises and decays. Figure 39a shows the measured volume fraction in normal condition. Figure 40 show a closer and more precise illustration of the first 100 ms of the dispersion process in normal condition. The figure shows the following: after 4.1 ms (different for the different initial gas velocities) the first parcel of particles reaches the monitor plane located at the nozzle height. Further they reach the 10 cm monitor after 31 ms, 20 cm after 52 ms and 30 cm after 80 ms (Figure 40).

On the other hand, Figure 39b shows that when the gravity does not have any influence on the particles, they stay in suspension after being dispersed by the gas. After 600 ms there is still some motion through the monitor planes for the zero gravity case (we return to this difference between the two conditions later in the thesis).

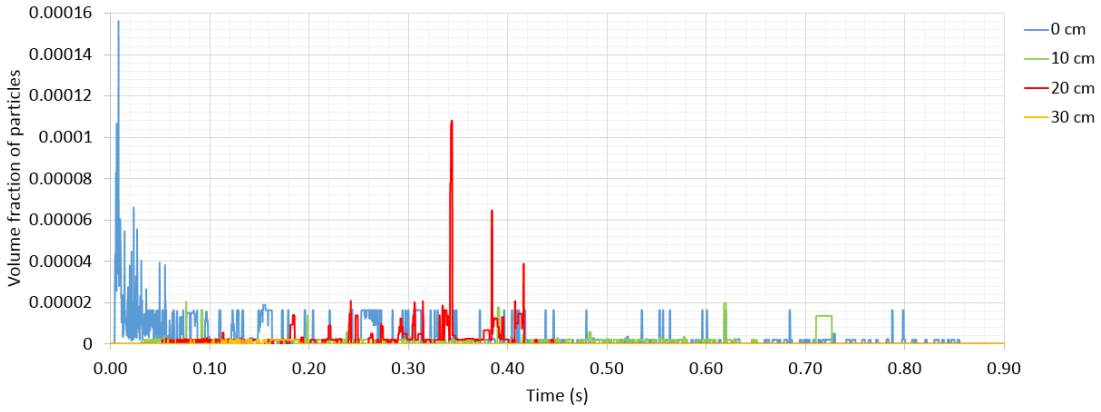


(a)

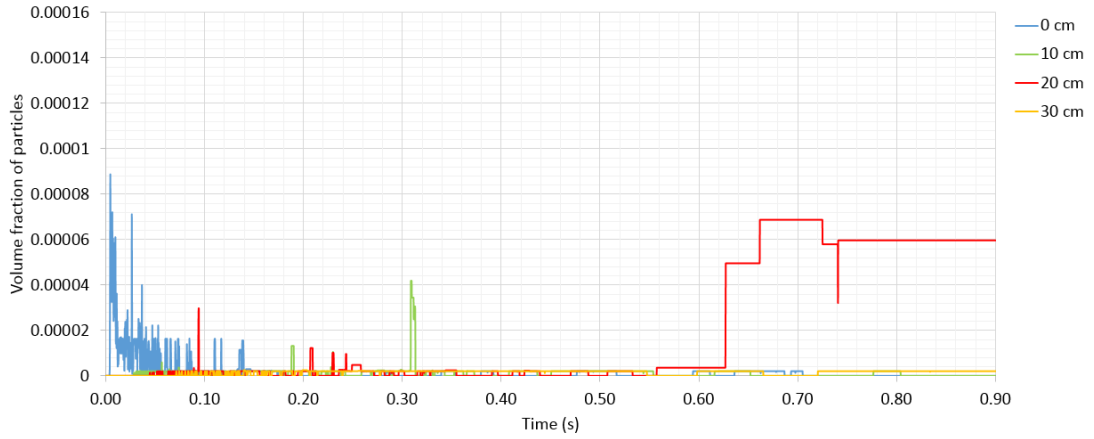


(b)

Figure 39: Volume fraction of particles moving through the Hartmann tube; (a) normal condition and (b) zero gravity condition.

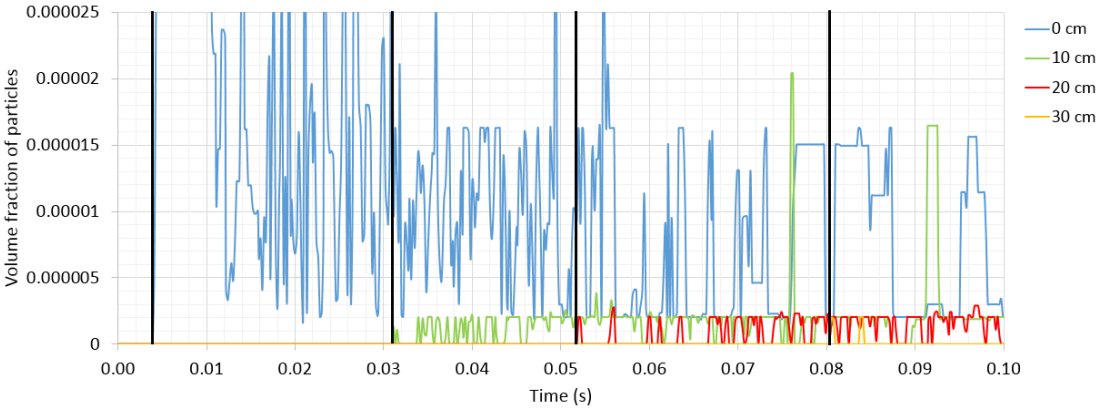


Figure 40: Volume fraction of particles moving through the Hartmann tube the first 100 ms. The black horizontal lines show when parcels of particles cross the different monitor planes located in the tube.

In all the cases, which are illustrated above, the amount of particles moving

through the monitor plane placed at the height of the injection nozzle is the largest. This is because there is more movement in the gas velocity field.

## 5.4 Influence of the gas injection velocity

The dispersion process is initiated and strongly influenced by the gas flow. Different simulations were created to investigate this issue. The gas velocity at the inlet varied in the range of 30-60 m/s. The velocity was held constant for 50 ms in each case with the same amount of particles and particle characteristics. Figure 41 shows the maximum particle position in z-direction as a function of time for different gas injection velocities. As mentioned in section 5.2 Figure 36 explains why the graph in Figure 41 shows that particles stop settling at 20 cm for some of the simulations. Particle position path for velocities under 50 m/s follows a smooth curve. When using 30 m/s the particles never reach heights above 0.22 m, which indicates that the cloud is not sufficiently uniform.

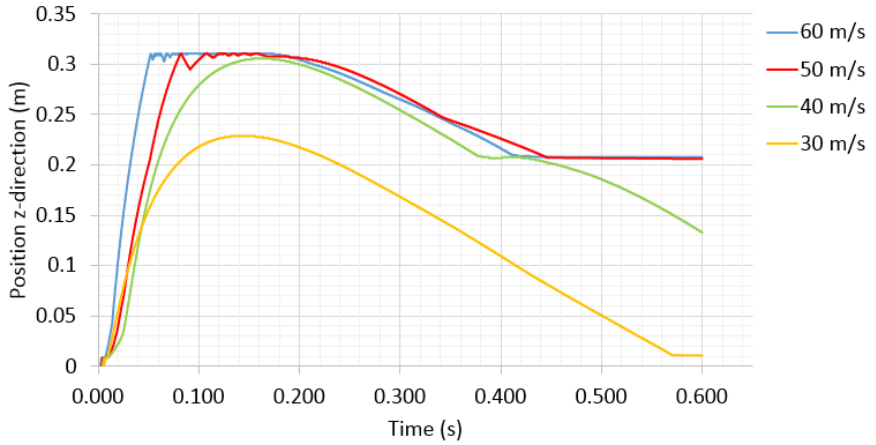


Figure 41: Maximum position of the particles in z-direction as a function of time for different gas injection velocities.

It is important to note that the downscaling of the gas injection velocity is different for each case. The velocity decays with 1 m/s regardless of initial gas velocity. This results in different velocity decay times and different duration of particle settling time, as shown i Table 1.

Table 1: Overview of simulations.

| **Inlet velocity** (m/s) | **Dispersion time** (ms) | **Downscaling** (ms) |
|---|---|---|
| 30 | 50 | 30 |
| 40 | 50 | 40 |
| 50 | 50 | 50 |
| 60 | 50 | 60 |

Figure 42 compares the results for the maximum particle velocity and the maximum particle position the first 25 ms with simulation results conducted by Christiansen [36] for one particle. The comparison of the cases is not straightforward, but the history of particle velocity in Figure 42a indicates significantly higher velocities if compared to Figure 42c. The maximum particle position shown in Figure 42b displays how the particles dispersed with a inlet gas velocity of 30 m/s is lifted faster than for 40-50 m/s gas inlet velocities. When comparing with a snapshot taken at the bottom of the tube after 20 ms (Figure 43), the plot shows the maximum position, which in this case correlates with one single particle illustrated at the left in Figure 43.

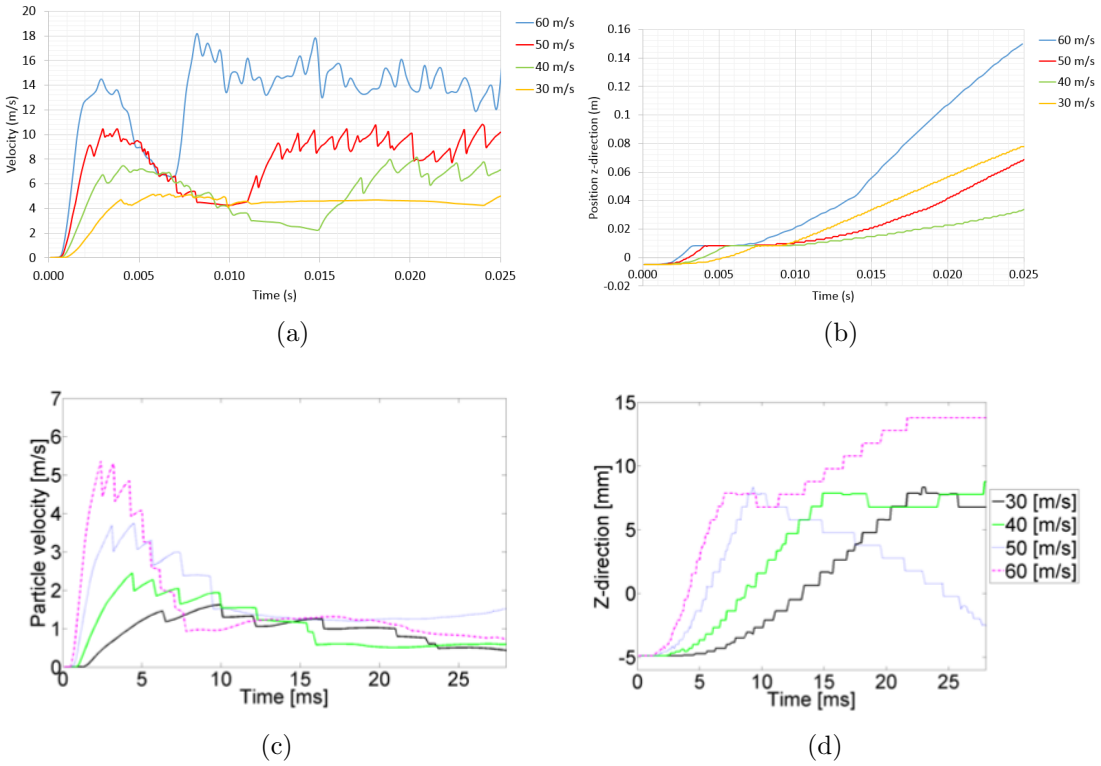


Figure 42: Particle movement characteristics for different gas injection velocities the first 25 ms of the dispersion processes compared to Christiansen's results [36]; (a) particle velocity as a function of time, (b) particle maximum position as a function of time, (c) particle velocity as a function of time [36] and (d) particle position as a fuunction of time [36].

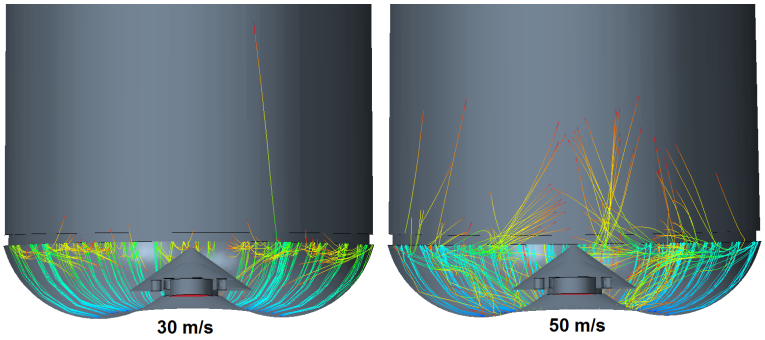


Figure 43: Snapshots 20 ms after initiation of particle movement. Left: particle streamlines with gas injection velocity 30 m/s. Right: particle streamlines with gas injection velocity 50 m/s.

Figure 44 shows the maximum particle velocity magnitude as a function of gas injection velocity. The graph shows an approximately linear correlation.

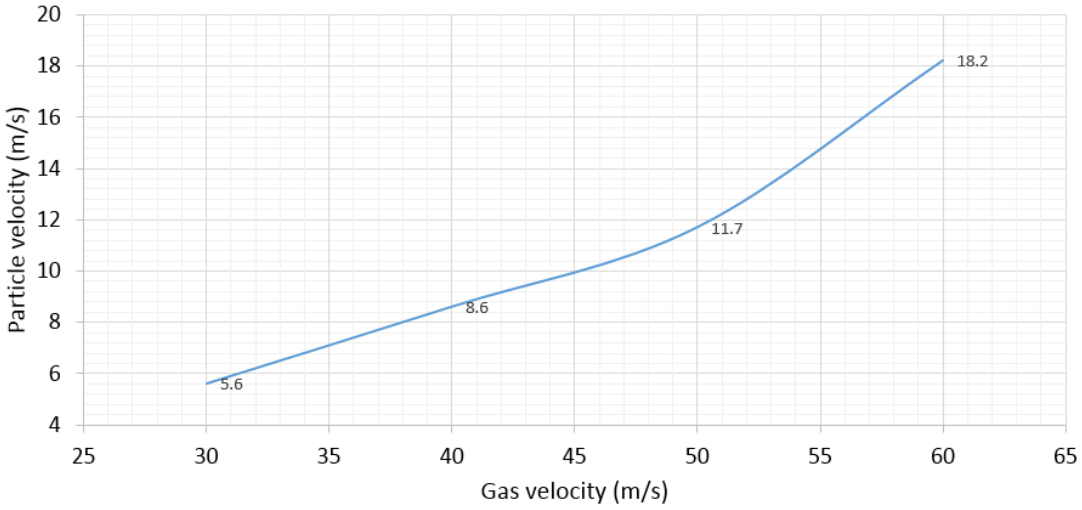


Figure 44: Maximum particle velocity magnitude as a function of the gas injection velocity.

Figure 41 might indicate that gas injected with velocities under 40 m/s does not manage to create a uniform dust cloud, for the case where the injection velocity was constant during the first 50 ms. Figure 45 shows the volume fraction of particles passing through different monitor planes in the tube when using a gas inlet velocity of 30 m/s. The particles never reach planes over 20 cm, they barely cross the 20 cm plane after 85 ms.

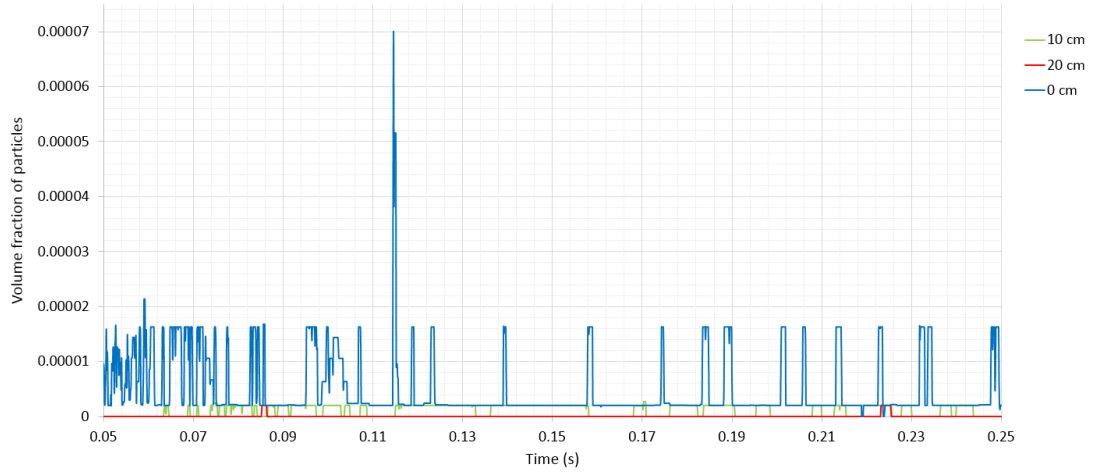


Figure 45: Volume fraction of particles when using initial velocity of 30 m/s. Time: 50 ms-250 ms.

When using a inlet gas velocity of 40 m/s the particles maximum position as a function of time follows a smooth curve (Figure 41). The particles reach the highest position 160 ms before they start to settle. The particles might reach an approximately uniform cloud but they never pass through the monitor plane located 30 cm above the nozzle (Figure 46). When comparing volume fraction distribution for 30 m/s and 40 m/s (Figure 45 and 46) there is a lot more particle movement located above the 20 cm monitor plane, where the ignition is located, when using 40 m/s gas injection velocity.

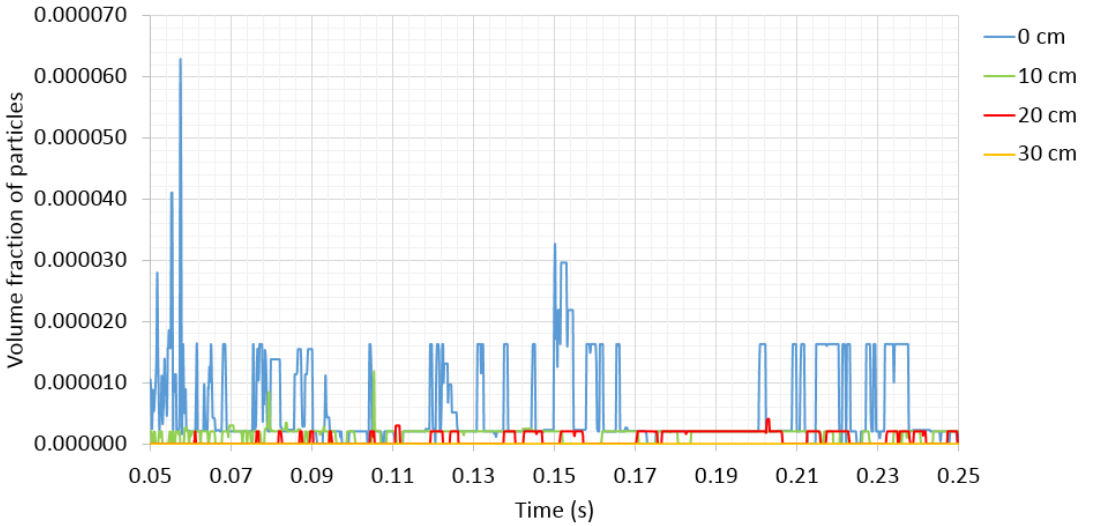


Figure 46: Volume fraction of particles when using initial velocity of 40 m/s. Time: 50 ms-250 ms.

When using 50 m/s as inlet velocity the particles reaches a maximum velocity of 11.7 m/s and collide several times with the outlet filter before starting to settle. The high inlet velocity causes a greater amount of particles to move, and Figure

47 shows how the volume fraction passing through the monitor planes is greater than for the lower velocities.

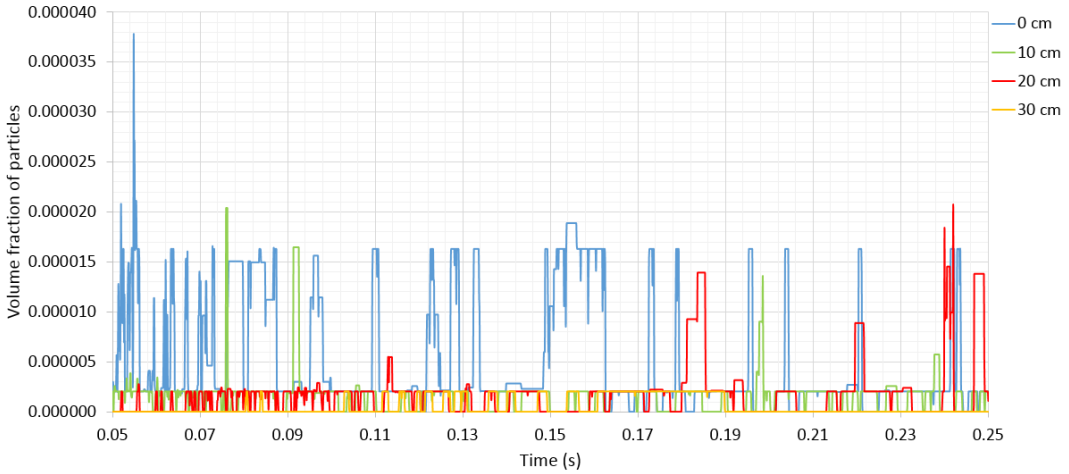


Figure 47: Volume fraction of particles when using initial velocity of 50 m/s. Time: 50 ms-250 ms.

A gas injection velocity of 60 m/s results in a maximum particle velocity of 18.2 m/s, which causes the particles to reach the outlet filter faster so that a larger portion of the particles is located in the upper part of the tube (Figure 48). The volume fraction of particles distribution in the time interval 50-250 ms illustrates intense particle motion in the tube. The settling process duration is longer for larger velocities.

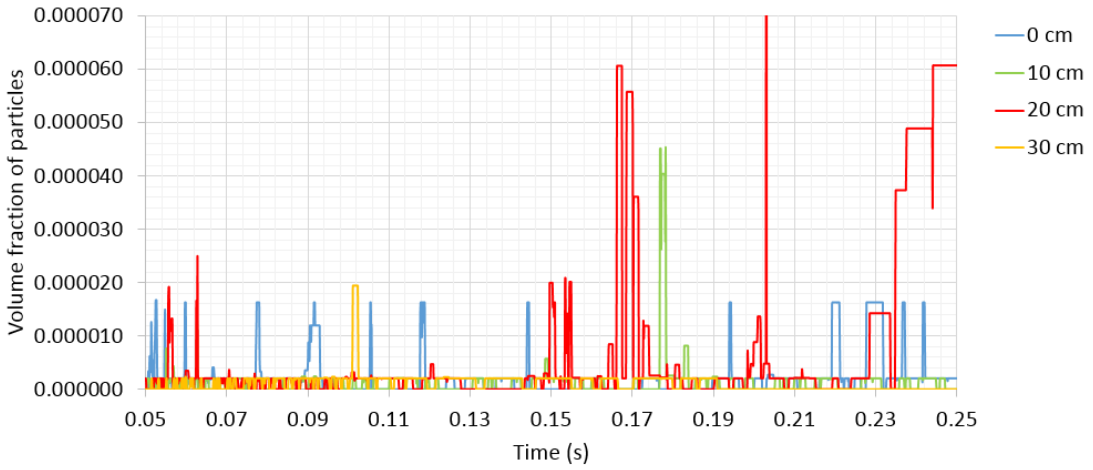


Figure 48: Volume fraction of particles when using initial velocity of 60 m/s. Time: 50 ms-250 ms.

## 5.5 Particle cloud propagation

When investigating the formation of a particle cloud, it is important not to only investigate the maximum particle position and the maximum particle velocity, but also to look at the particle cloud as a complete system. Both Murillo et al. [23] and Berg [37] experimentally investigated the propagation of a dust cloud in normal conditions. In this section the movement of the particle cloud in normal condition are compared to previous research in order to validate the results and explain why 50 m/s gas injection velocity was used as standard for the simulations.

Berg [37] used a high-speed camera (HSC) to investigate the movement of the particle cloud. HSC can be a very useful tool in combustion research, but with 1 gram dust sample it is very difficult to extract precise data. Therefore, when using HSC, a lot of uncertainties may occur. Figure 49 shows one of the images used to extract dust cloud position data. It is obviously a challenging task to find the right cloud position at each point in time with this kind of tool: although the photograph shows a possible boundary of the cloud, it is still unclear if this selection is correct.

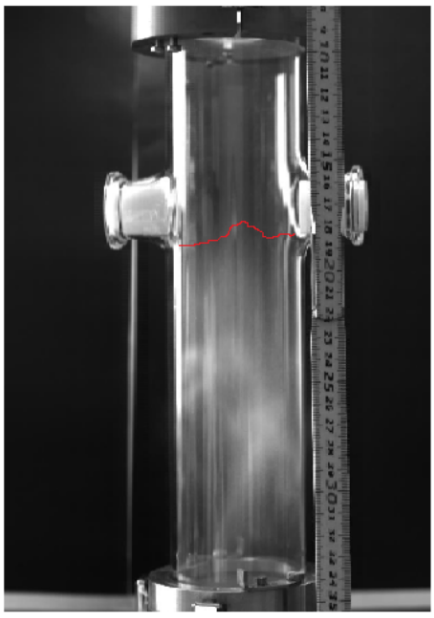

Figure 49: 1 gram dust sample dispersed by a 5 barg pressure pulse (20 ms).

When looking at Figure 50, it is not straightforward to see if the pressure used to disperse the dust sample seen on HSC, corresponds to results from a simulation where a gas injection velocity of 50 m/s was used. Already after 50 ms the experiment show traces of a well dispersed cloud, but in the simulation the particle cloud has not yet reached the ignition zone. Snapshots of the total dispersion process with 10 ms intervals is presented in Figure 51. Figure 51 shows particle dispersion during the first 100 ms with an injection velocity of 50 m/s. Figure 51 might indicate that the dispersion process is not completed before 100 ms of

the simulation. An approximately uniform dust cloud can be seen in the interval 80-100 ms. To visualize the particle movement better, Figure 52a shows particle tracks, one line for each particle, and the monitor planes measuring the cloud propagation. Particle cloud height above injection nozzle as a function of time compared to results from Berg's [37] experiments is presented in Figure 52b.

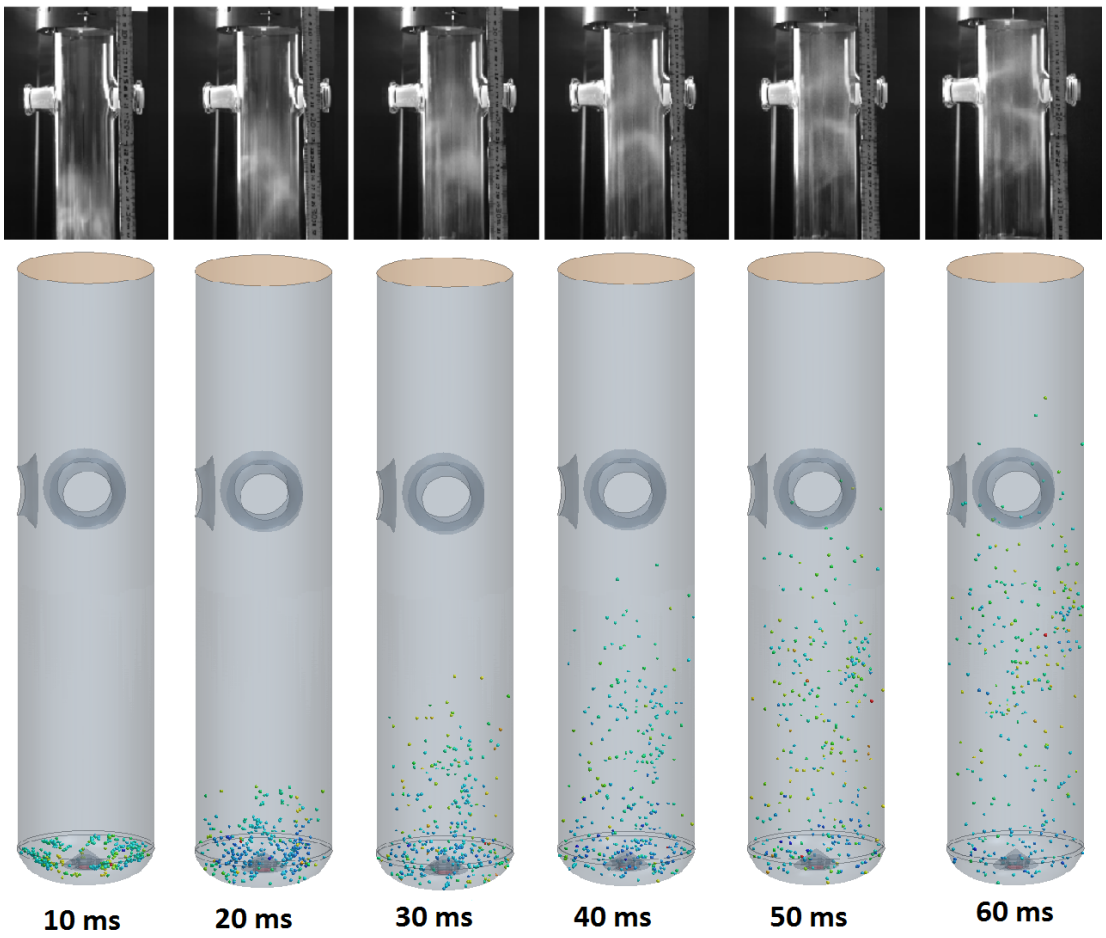


Figure 50: Particle cloud dispersion. Experimental results achieved from a 5 barg injection pressure conducted by Berg [37] (1 gram of glass beads) compared with an injection velocity of 50 m/s.

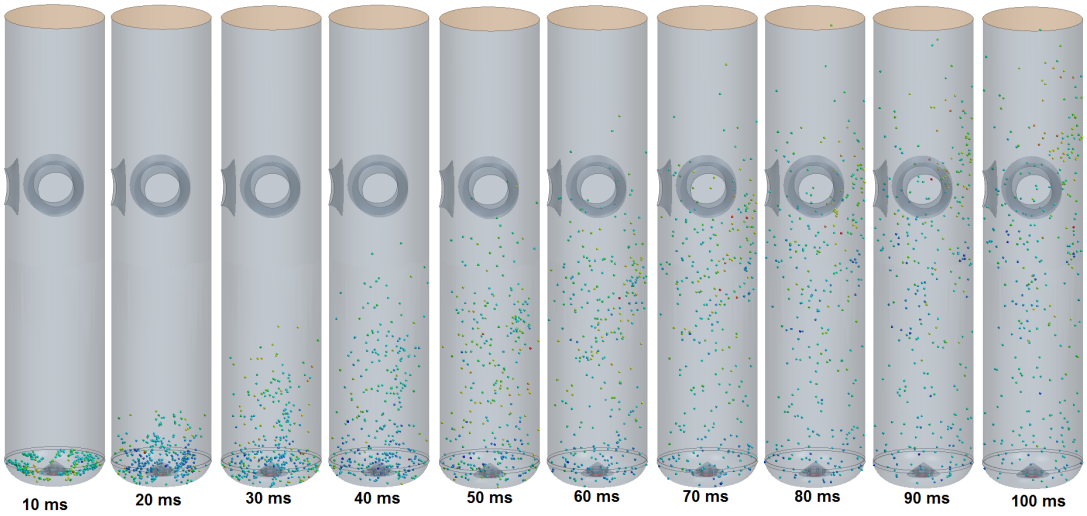


Figure 51: Particle cloud dispersion (50 m/s the first 50 ms, gas velocity decay 50 ms). Particle characteristics: density 2500 kg/m$^3$, diameter 106 $\mu$m, number: 306 particles.

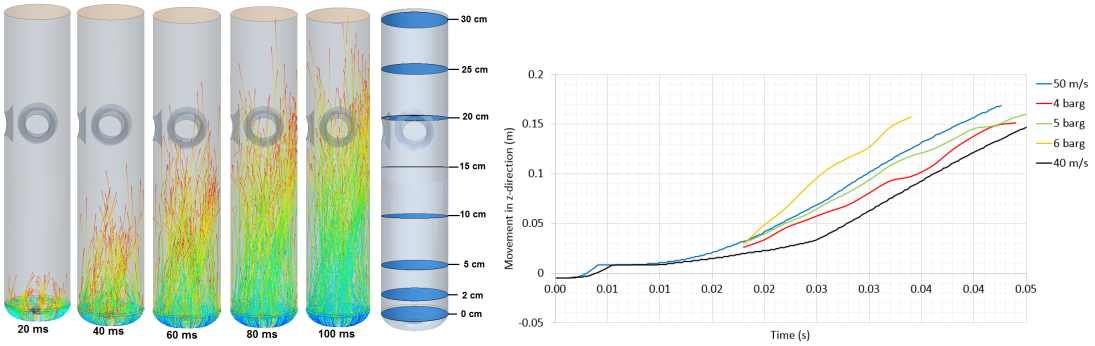


(a) (b)

Figure 52: (a) Particle streamlines and (b) cloud height above nozzle as a function of time for different injection velocities compared with experimental results from Berg [37].

Figure 52b shows the particle cloud movement in z-direction as a function of time. The x-axis needed to be rescaled for the data to be comparable with the experimental results achieved by Berg. When using HSC to investigate the position of the dust cloud, it is not possible to measure under the 20 mm high rim at the bottom of the Hartmann tube (see Figure 49). Therefore it is assumed that the time scale starts when the dust cloud reaches a 20 mm height.

Figures 52b and 53 compare the simulation results with Berg's [37] experiments. Berg used an inlet pressure of 4, 5 and 6 barg and a dust sample of 1 gram glass beads with diameter 106 $\mu$m. The simulations have gas injection velocities of 50 m/s and 40 m/s, containing 306 glass bead particles with the same diameter. The dust sample of 1 gram was chosen because this was the smallest sample that

was used in experiments. The figures indicate that a gas injection velocity of 50 m/s validates well with a gas injection pressure at 5 barg.

When using Berg's time scale and rescale the simulation data, to validate the results, Figure 53 shows matching results. This indicates that the rescaling was done correctly (Figure 53).

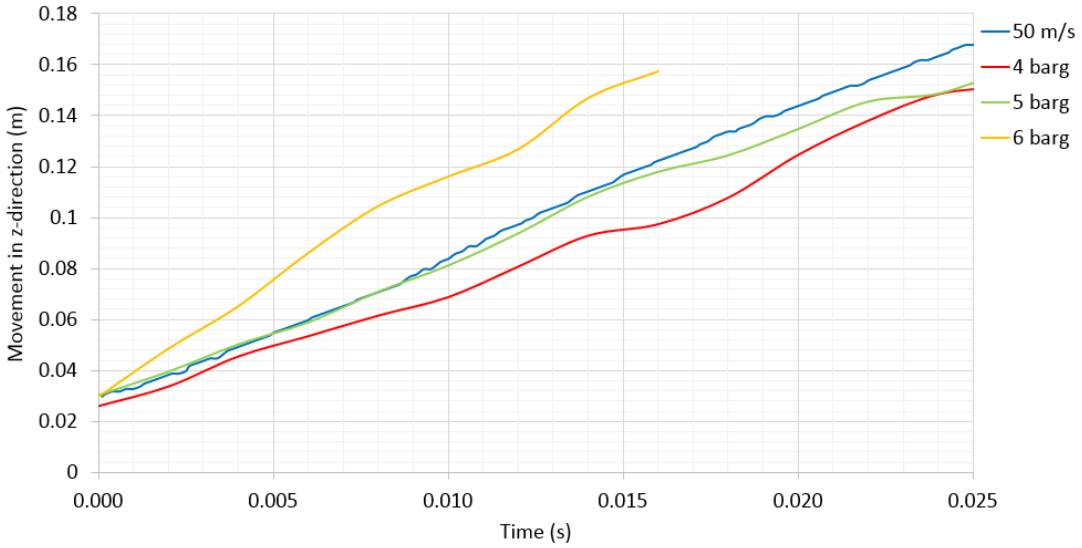


Figure 53: Particle cloud propagation the first 100 ms.

Murillo et al. [23] investigated the dispersion process of wheat starch with an injection pressure of 7 barg. Figure 54 shows the simulation results comparing the (A) gas streamlines with (B) high-speed video images and (C) the dust concentration distribution the first 120 ms. The most comparable results are achieved between 60-80 ms. When comparing Figure 54c with Figures 50 to 52, it can look like the dense dust cloud in 54c never really leaves the tube bottom, but the experimental results in Figure 54b show a generated dust-cloud already after 60 ms.

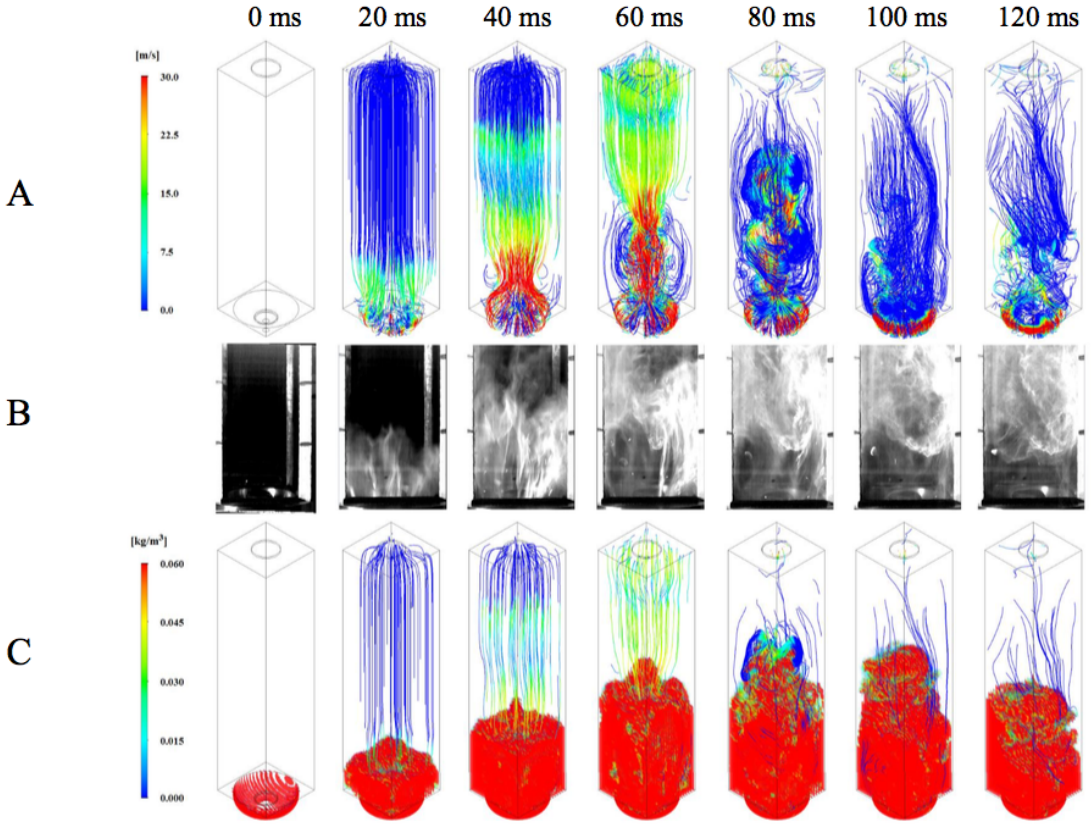


Figure 54: Distribution of the wheat starch dust cloud in the modified Hartmann tube; (A) streamlines and velocity of the gas flow (m/s), (B) High-speed video and (C) dust concentration (kg/m$^3$) [23].

## 5.6 Duration of a steady particle cloud

An important parameter when investigating dust cloud explosion characteristics, is how long the particles are able to form a uniform dust cloud before the settling process starts and the concentration no longer is in the explosive range.

Figure 55 compares particle maximum velocity, maximum and minimum position as a function of a time in normal condition and zero gravity condition. For both cases the particle maximum velocities correlates with each other, but the particle positions show significant differences. When the gas velocity decays the particle velocity follows and decrease as the time moves on. When the gas velocity declines sufficiently, the settling process starts in normal condition. When comparing the minimum particle position, it is shown that the minimum particle position is a lot higher for the simulation run with zero gravity condition. The particles are getting lifted higher by the gas vortices when the gravity force has no impact on the particles.

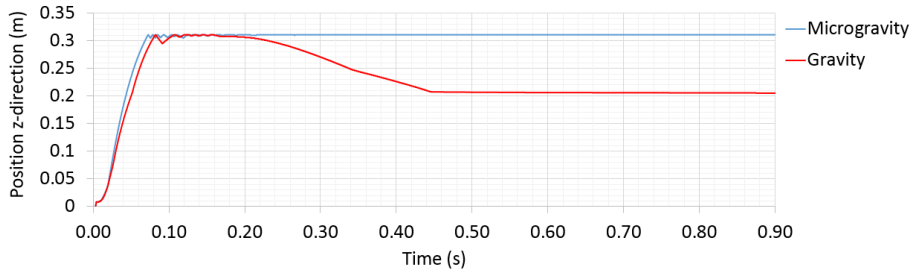


(a)

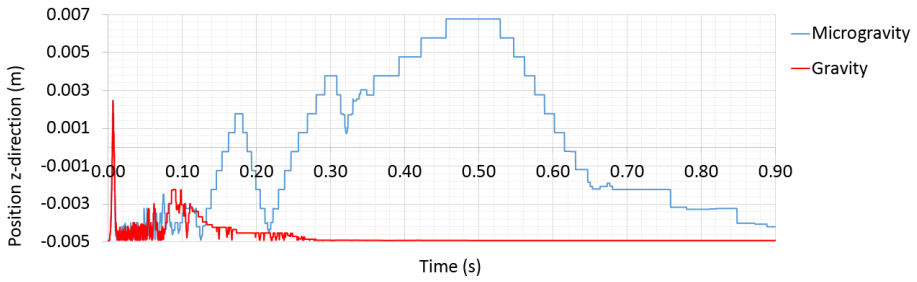


(b)

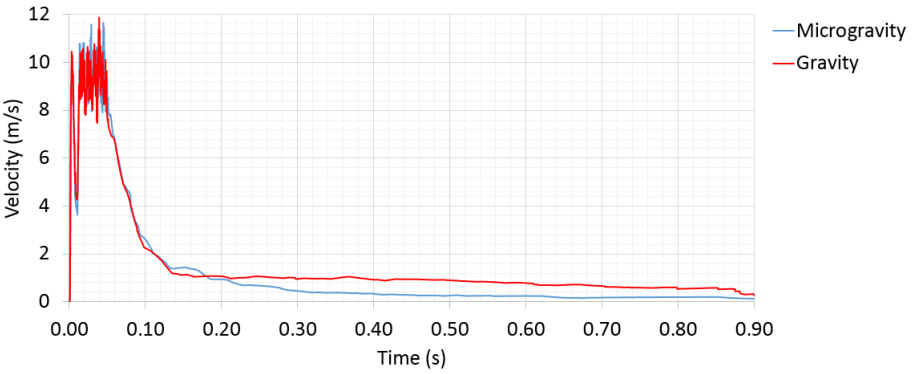


(c)

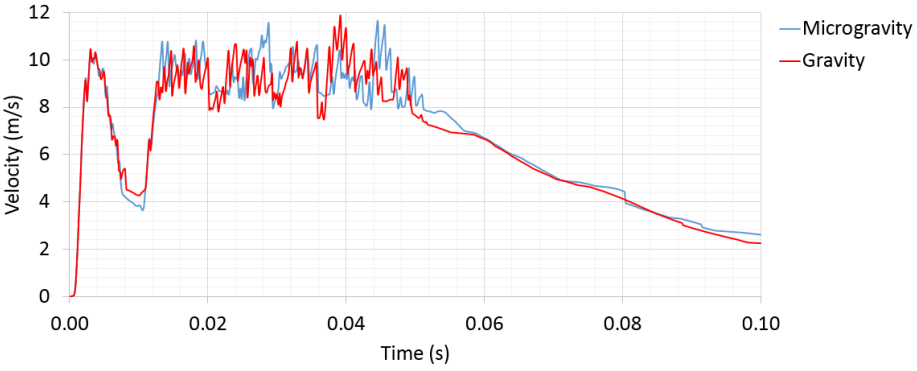


(d)

Figure 55: Particle movement in zero gravity condition versus normal conditions: (a) maximum particle position as a function of time, (b) minimum particle position as a function of time, (c) particle velocity as a function of time and (d) particle velocity the first 100 ms.

The volume fraction monitors (Figure 56) show how the particles are dispersed through the tube and later stay at the same location because there is no more particle movement across the monitor planes. In normal gravity there is only a small amount of particles still in motion after 600 ms and as the time passes they settle under the monitor plane located at the nozzle height, after 850 ms and there is no particle movement in the tube column. In the zero gravity condition there is much more action. A larger amount of particles are in motion and at a higher position in the tube. There are particles partitioned also at 30 cm above the dispersion nozzle and the monitor plane located at the ignition source measures the largest amount of particles.

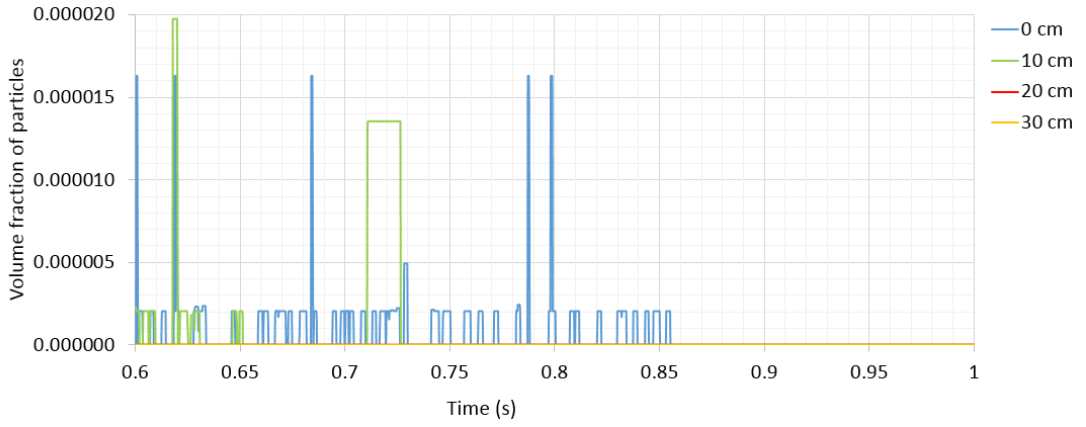


(a)

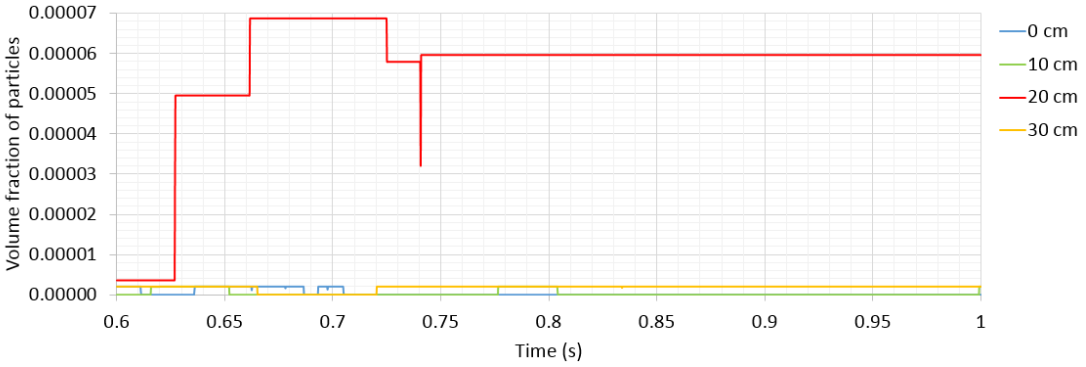


(b)

Figure 56: Particle movement through the monitor planes after 600 ms to 1 s into the simulation process; (a) normal condition and (b) zero gravity condition.

The ideal condition for dust cloud explosion investigation was suggested to be a condition where the gravity would be absent [5, 12, 2, 6]. Figures 56 and 57 substantiate the possibility for the particles to remain in suspension after the decay of gas velocity. When looking closer to the particle movement in zero gravity condition, the dust cloud may represent a uniform particle cloud already after 100 ms (Figure 57). This is when the gas injection velocity have decayed and the particles remain dispersed thorough the rest of the simulation time (0.1 s -1 s). Figure 57 shows the particles in the tube for both zero gravity condition

and normal condition. This matches Figure 56 where in normal condition the particles are located in the bottom 10 cm of the tube and after 750 ms there is only movement through the plane located at the nozzle height. However, for the zero gravity case an intense particle movement is not detected, but the particles are still detected at higher positions.

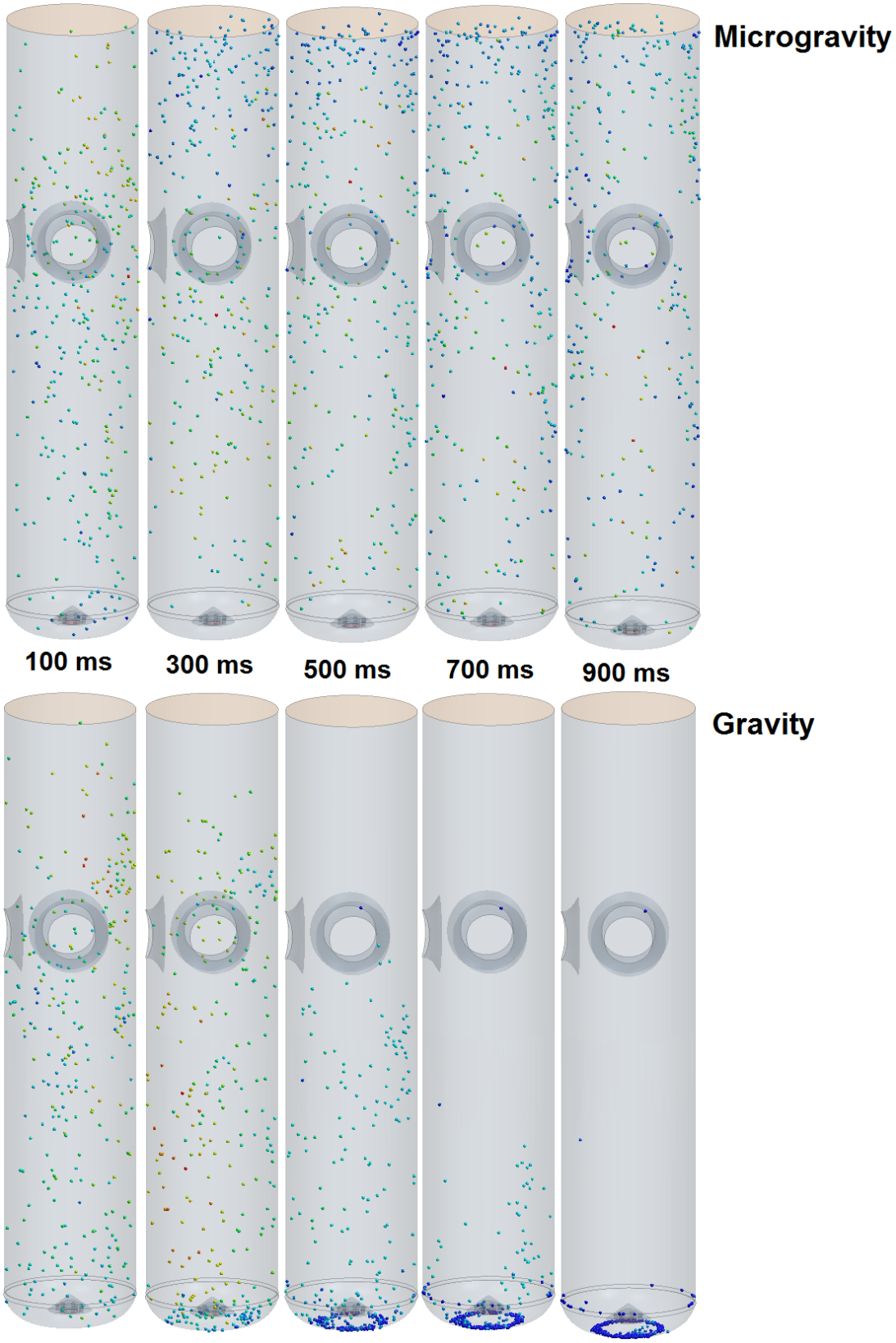


Figure 57: Snapshot of the Hartmann tube 100 ms to 900 ms. No gas injection present.

## 5.7 Explosive dust cloud generation

For the simulation of this dispersion process to be important in the research for exploring dust cloud combustion characteristics, the concentration of fuel particles need to be above the lower explosive limit (LEL). An explosive concentration (EXC) is a concentration of the fuel particles where an explosion is almost guaranteed. In this section flammable particles are investigated instead of glass beads studied in previous sections, so that we can look into the possibility of generating an combustible dust cloud. Important characteristics for the cloud to be flammable and explosive inside the Hartmann tube are listed in table 2 [39].

Table 2: Characteristics of the combustible particles.

| **Solid** | **LEL** ($g/m^3$) | **EXC** ($g/m^3$) | **Quantity** (g) | **Number of particles** |
|---|---|---|---|---|
| Lycopodium | 125 | 150 | 1.65 | $98.9 \cdot 10^6$ |
| Cornstarch | 40 | 60 | 0.66 | $327.5 \cdot 10^6$ |
| Aluminium powder | 100 | 120 | 1.32 | $10.3 \cdot 10^6$ |

(Number of particles was calculated with the density and diameter specified in Table 3.)

When looking at the number of particles needed for generating an combustible concentration in the tube, with the different combustible materials listed in Table 2, the Eulerian-Lagrangian approach may not be the best model to investigate such a large amount of particles. On the other hand, the computational power needed for this task is enormous. An alternative solution would be to make a model where each particle represents a cluster or a small cloud of particles. Nevertheless, when adding more particles in the simulation for lycopodium powder, Figure 58 shows no significant deviation for the different amounts. This is still a small amount of particles, but can give an indication in whether the number of particles affect the distribution in any significant way.

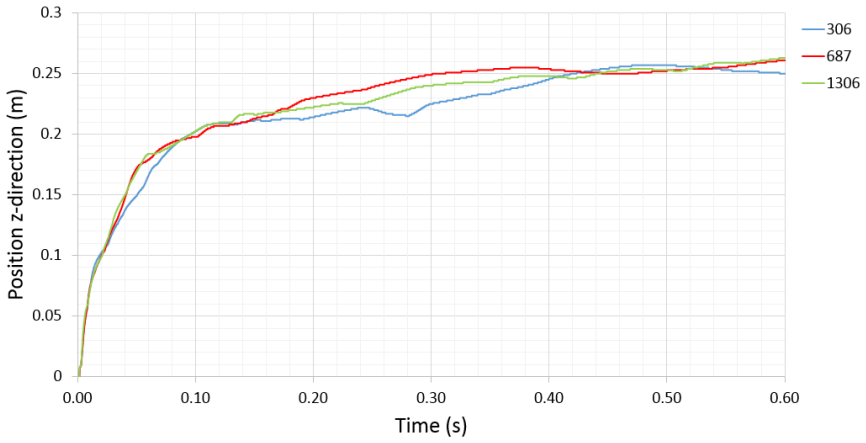


Figure 58: Maximum particle position in z-direction for different number of particles present in the tube.

The size and density of the particles might have a influence on the velocity of the sedimentation process in normal gravity. It also might affect which initial gas velocity that gives the best uniform solution. Both the diameter and the density of the particles was varied and the results is presented in this section. The spherical shape of the particles was constant, but number of particles was varied for lycopodium.

Table 3: Overview of particle properties used in simulations.

| **Material** | **Diameter ($\mu$m)** | **Density (kg/m$^3$)** | **Number of particles** |
|---|---|---|---|
| Glass beads | 106 | 2500 | 306 |
| Lycopodium | 30 | 1180 | 306 |
| Lycopodium | 30 | 1180 | 687 |
| Lycopodium | 30 | 1180 | 1306 |
| Cornstarch | 20 | 481 | 306 |
| Aluminium powder | 10 | 800 | 306 |

Figure 59 shows a clear difference in both maximum particle velocity and in maximum particle position for combustible particles versus glass beads. This could be because of the size and density of the particles. Nevertheless, the distribution of the combustible particles matches. Both the dispersion time and the settling time increase when the particle diameter and density decrease. When using an gas injection velocity of 50 m/s the small combustible particles never reach the top of the tube, however it might still form an combustible mixture if the concentration is right. Figure 59b shows that the combustible material particles achieve a larger velocity than the glass bead particles. The plot do not specify which direction the velocity is in, and by comparing with Figure 59a the particle may only be swirling around in the middle part of the tube.

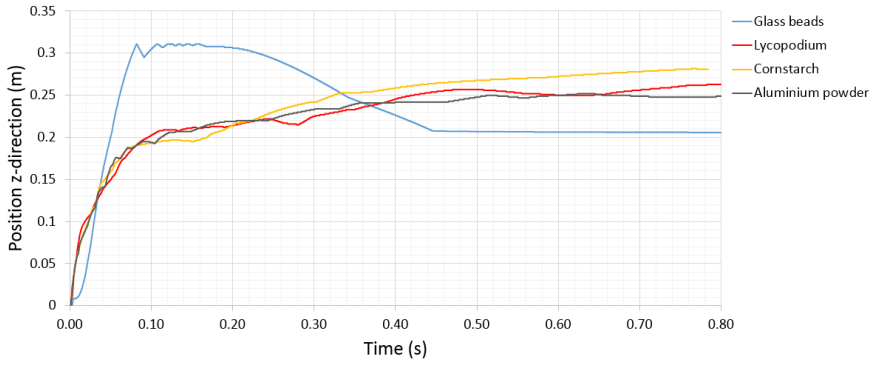


(a)

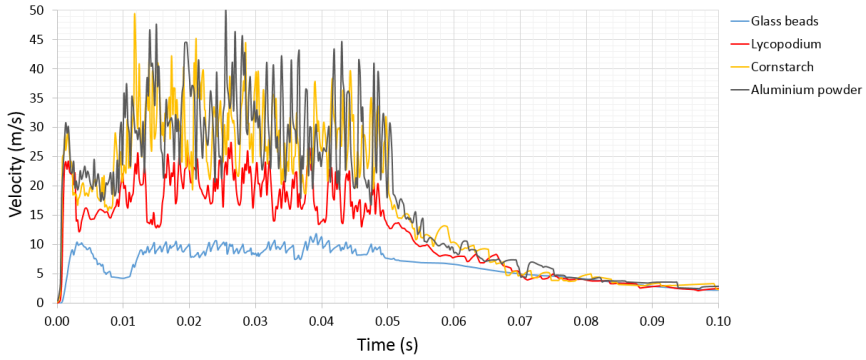


(b)

Figure 59: Particle movement. Comparison of glass beads, lycopodium, cornstarch and aluminium powder: (a) maximum particle position as a function of time and (b) maximum particle velocity as a function of time.

Figure 60 shows the first 25 ms of the dispersion process for the different particle types. By comparing with Figure 61, the movement in Hartmann tube is initiated a lot faster for the lighter combustible particles. The combustible particles takes a lot longer to get dispersed and to settle.

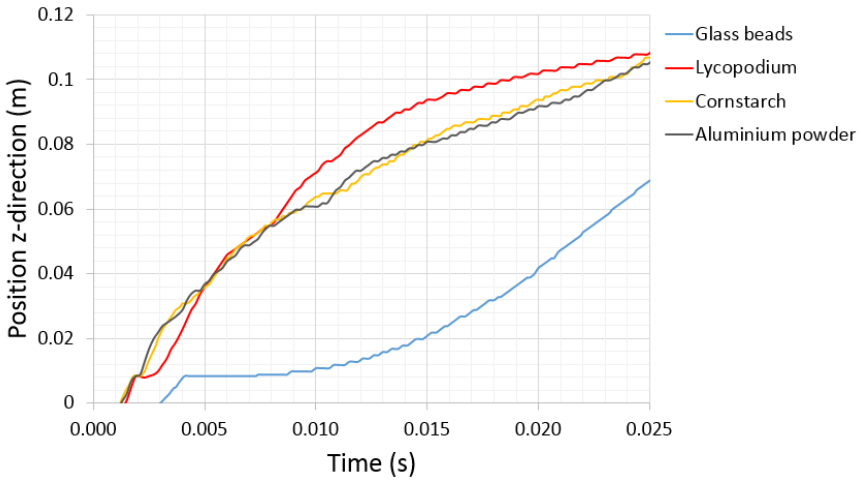


Figure 60: Maximum particle position in z-direction for different particle types present in the tube.

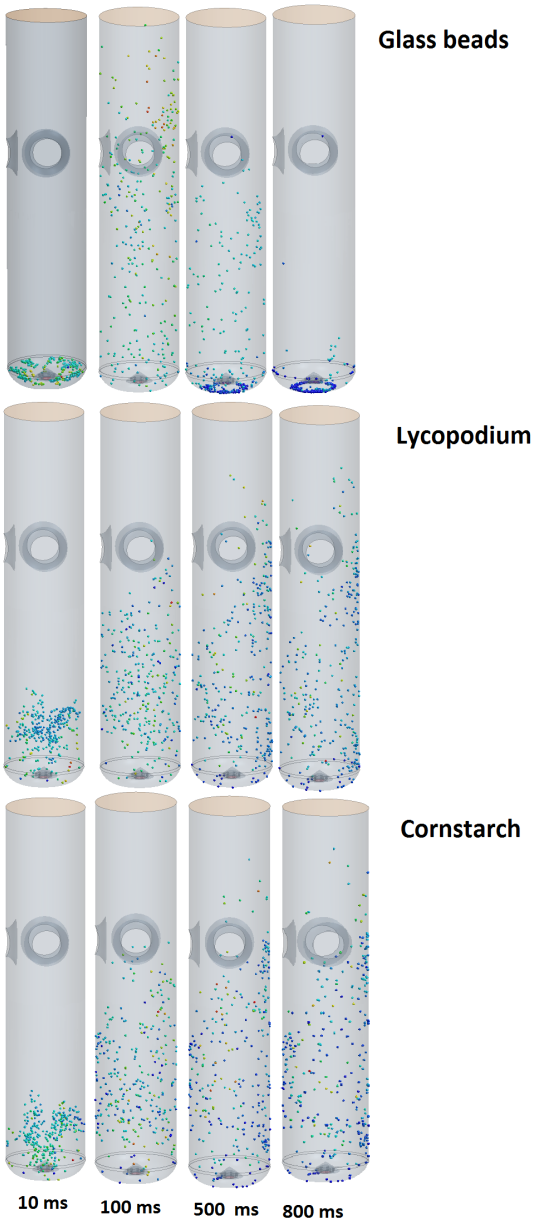


Figure 61: Particle distribution for different materials, but same amount of particles (10-800 ms).

As mentioned earlier in this section, the glass bead particles are significantly larger than the other particles. When calculating the momentum response time ($\tau_v$) with the use of Equations (29) and (30), it was observed a correlation between the particle sizes, particle velocity and particle movement in z-direction. Table 4 shows how the momentum response time decreases together with the particle size. This means that the largest particles need longer time to respond to the velocity changes in the continuous phase and achieve lower velocities during the dispersion. This may be one of the reasons why the smallest particles obtain relatively high values of velocity magnitude.

Table 4: Momentum response time ($\tau_v$), calculated by using particle density and diameter from Table 3.

| **Material** | **Momentum response time,** $\tau_v$(s) |
|---|---|
| Glass beads | 0.83 |
| Lycopodium | $3.15 \cdot 10^{-3}$ |
| Cornstarch | $5.71 \cdot 10^{-4}$ |
| Aluminium powder | $2.37 \cdot 10^{-4}$ |

## 5.8 Influence of the coefficient of restitution, $e$

The coefficient of restitution ($e$) is an important parameter, which influences the particle-wall collision process. When investigating how the coefficient of restitution influences the collision-process and further the results three simulations were conducted, using different values of the restitution coefficient (Table 5). A totally elastic collision modelled by a restitution coefficient of 1.0, so that the expectation is that the particle velocity magnitude should maintain the same after the collision with the wall. If the coefficient is less than 1.0, the walls absorb some of the particle velocity.

When the particle motion is initiated and gets accelerated by the gas, as mentioned in section 5.2, the particles travel along the bottom of the tube where the initial motion gets disrupted by collisions with the wall in the bottom of the tube. When the particles collide with the wall a velocity reduction occurs. Figure 63 shows how the maximum velocity of the particles decreases due to particle-wall collisions. It is important to note that the monitor measures the maximum particle velocity and position, which means that it only measures the particle whose velocity is the largest of all the particles and that reached the highest elevation.

Figures 62-65 confirms the theory, a restitution coefficient below 1.0 leads to an inelastic collision and particle deceleration, while a coefficient value at 1.0 leads to a fully elastic collision where the change in the particle velocity is hardly to observe. Independent of coefficient value the particles move along the bottom of the tube as shown in Figure 29 during the first 20 ms.

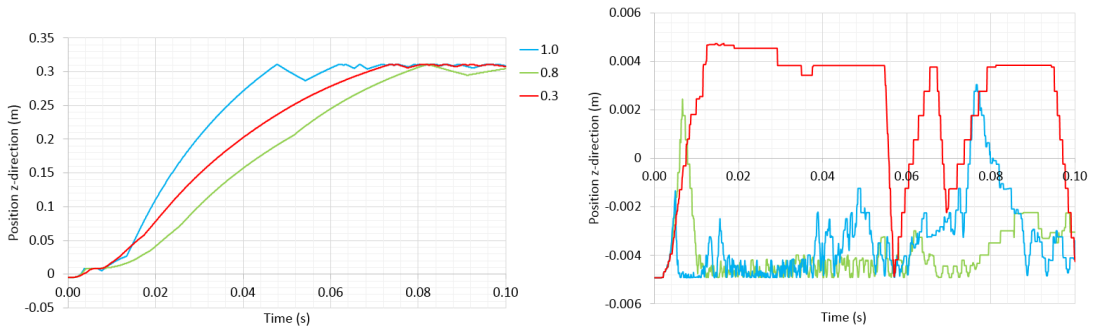


(a) (b)

Figure 62: (a) Maximum particle position as a function of time and (b)minimum particle position as a function of time for different values of restitution coefficient.

These observation is in agreement with Kosinski et al. [26] and Ilea et al. [27]. They observed a higher dust lifting effect with a higher coefficient of restitution. Their studies were done for many particles and the particle-particle collisions also influenced the process. When comparing the results to Christiansen [36] it correlates even though she only investigated the movement of one single particle.

Table 5: Comparison of particles with different values of coefficient of restitution. Maximum particle velocity and number of collisions with the wall during the first 20 ms of the dispersion process is shown.

| Coefficient of restitution | Maximum velocity first 20 ms (m/s) | Maximum velocity in total (m/s) |
|---|---|---|
| 1.0 | 13.7 | 15.7 |
| 0.8 | 10.75 | 11.7 |
| 0.3 | 9.2 | 9.2 |

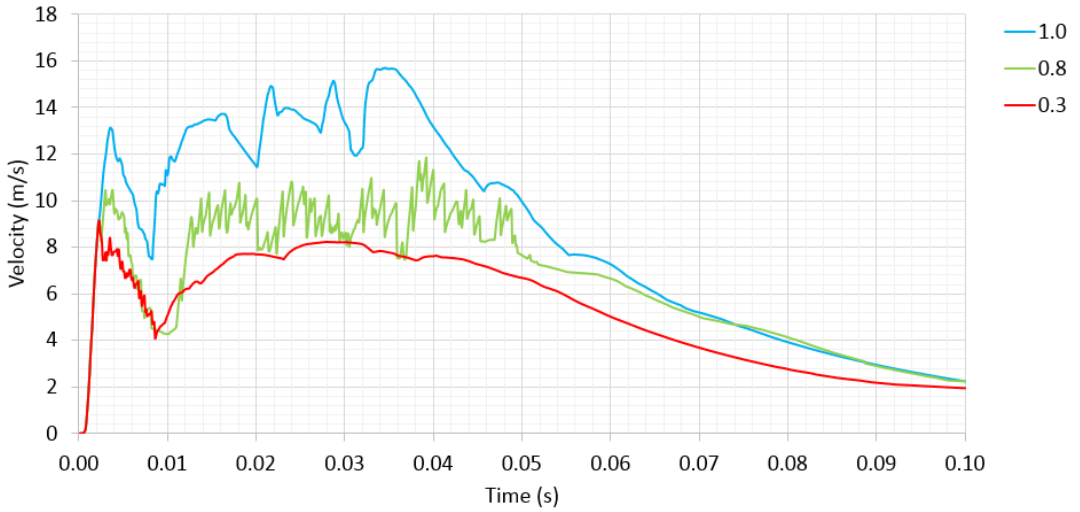


Figure 63: Particle velocity as a function of time for different values of restitution coefficient.

After 20 ms the majority of the particles enters the tube column and collide with the walls when they flow further up. Figure 63 shows the particle velocity through the whole particle dispersion process (first 100 ms) and Figure 64 shows the particle movement in z-direction.

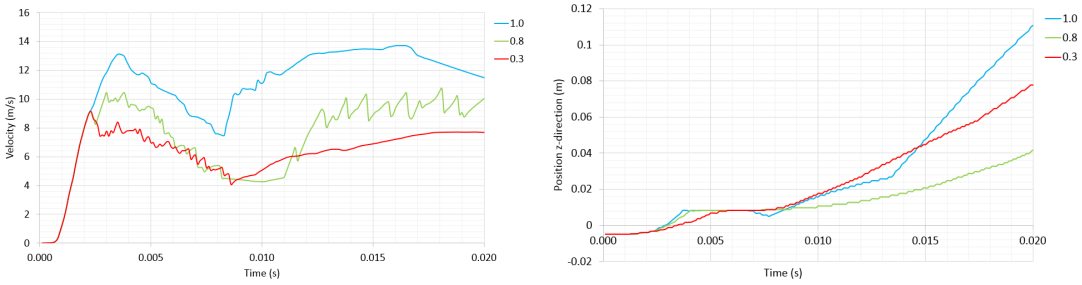


(a) (b)

Figure 64: Comparison of different values of coefficient of restitution (1.0, 0.8 and 0.3): (a) maximum particle velocity as a function of time during the first 20 ms and (b) maximum particle position in z-direction as a function of time.

When comparing Figure 42a and b from section 5.4, where the gas injection velocity varies, to Figure 63 where the restitution coefficient varies, the results correspond well. When the restitution coefficient models an inelastic collision the particle velocity decays but the particles still travel faster up into the tube column because after colliding with the rubber seal the gas velocity is stronger then their velocity in opposite direction. Nevertheless, the total maximum particle velocity is lower through the whole simulation.

For getting a better understanding of the particle movement snapshots of the particle tracks after 20 ms were included (Figure 65). Figure 65 shows snapshots

of the particle tracks with different values of the restitution coefficient. For the case when the restitution coefficient value is 1.0 and the collision is elastic the particles movement is more straight and follows a different path than if the collision is more inelastic. For the value of 0.8 the particles follows a more curved path after collision with the rubber seal. For a restitution coefficient value of 0.3, the particles get lifted immediately after collision with the rubber seal by the gas field, and follow the path of case 2 illustrated in Figure 31. The particle velocity is too low to defeat the gas injection movement.

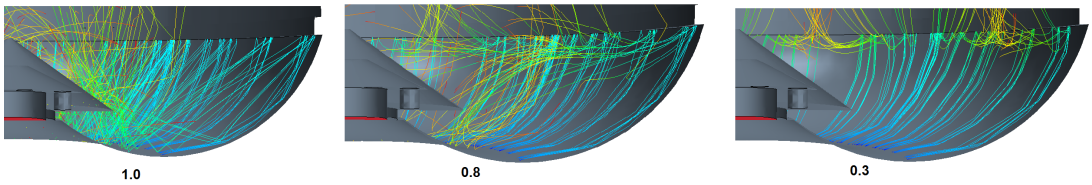


Figure 65: Particle tracks the first 20 ms for restitution coefficient values of 1.0, 0.8 and 0.3.

## 5.9 Influence of the shear lift force, $\mathbf{F}_{LS}$

The shear lift force calculated by Saffman is presented in Equation (19) where the shear lift coefficient, $C_{LS}$, is used. There are two types of lift force coefficients, Saffman (Equation 22) and Sommerfeld (Equation 24). To evaluate the lift forces impact on the particle movement three simulations were carried out, one with the Sommerfeld shear lift coefficient, one with the Saffman shear lift coefficient and one where the shear lift force was disabled.

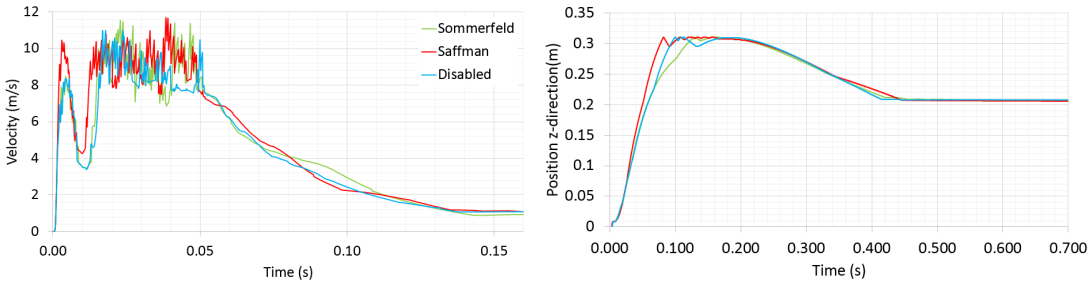


(a) (b)

Figure 66: Comparison of particle (a) maximum velocity the first 150 ms of the simulation and (b) maximum position in z-direction the first 700 ms of the simulation, obtained by different models as a function of time. Saffman, Sommerfeld or shear lift force disabled.

The particle maximum velocity and maximum position development during the dispersion process is shown in Figure 66. A slightly larger lifting of the particels appeared when using the Saffman coefficient. When comparing the results to

Christiansen [36] it might indicate that the shear lift force does not affect the particle dispersion in any significant way. Similar observation were made by Zydak [40], who investigated an interaction of a shock wave with a dust layer.

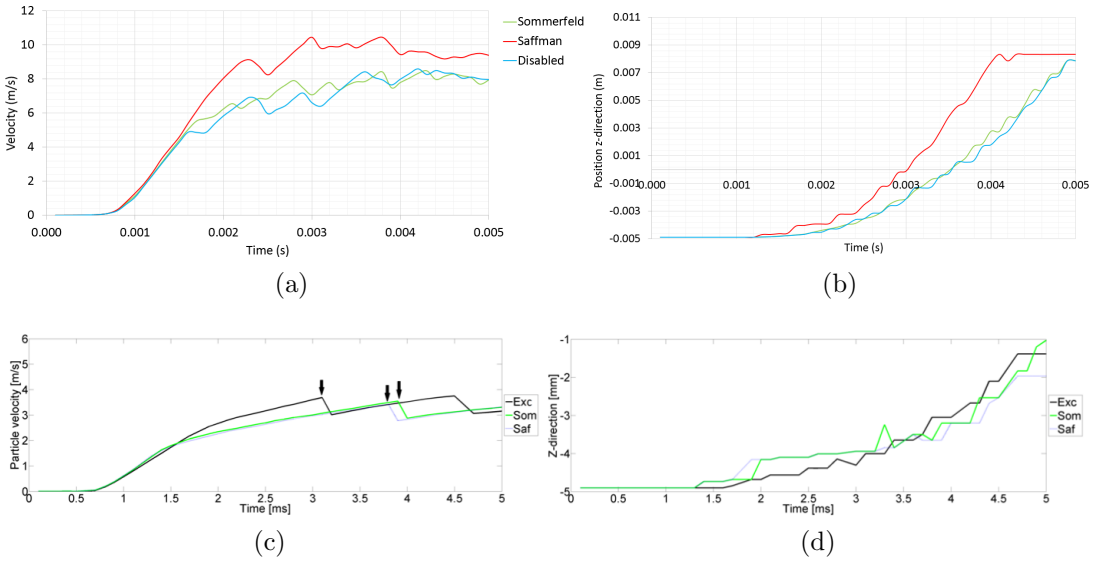


Figure 67: Comparing the influence of Saffman and Sommerfeld shear lift coefficient on the particle motion the first 5 ms. (a) maximum particle velocity as a function of time, (b) maximum particle position as a function of time; (c) particle position [36] and (d) particle velocity [36] as a function of time.

## 5.10 Influence of the pressure gradient force, $\mathbf{F}_p$

Pressure gradient force as mentioned in section 3.2.1 is a inter-phase force acting on the particle due to pressure differences in the carrier fluid (Equation 18). The effect of the pressure gradient force on the particle movement is evaluated in this section by comparing maximum position and velocity of the particles for the case when the pressure gradient force was included in the model and a case when the force was disabled. The effect is only considered the first 100 ms of the dispersion process because after this it was not straight forward to observe any differences. Figure 68 illustrates the maximum position and velocity of the particles the first 100 ms of the dispersion where the gas injection velocity have a constant value of 50 m/s during the first 50 ms and decays with a rate of 1 m/s per millisecond.

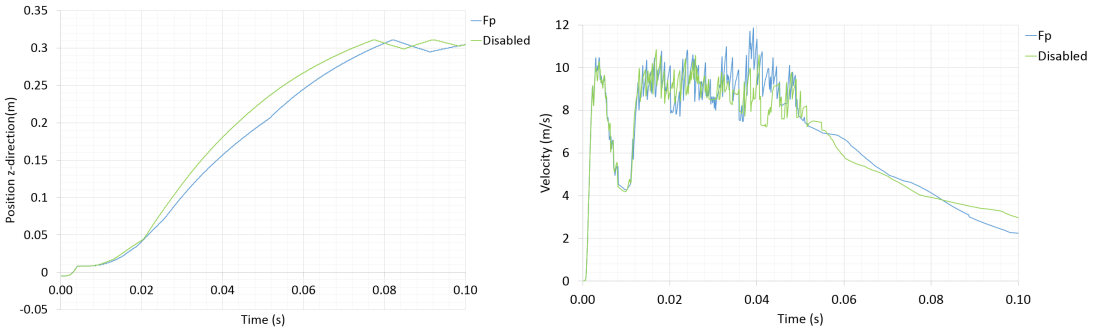


(a) (b)

Figure 68: Pressure gradient force ($F_p$) compared to no effect; (a) maximum particle position as a function of time and (b) maximum particle velocity as a function of time.

From the results, it can be concluded that no significant differences were observed. Neverthless, when the the pressure gradient force was disabled, the maximum particle position increased faster and collided with the filter at the outlet a few millisecond earlier. The lifting of the particle follow the same path and the maximum particle velocity matched. Research performed by Christiansen [36] shows a more significant influence when only on particle was included in simulations. Velocity and position of the particle is presented in Figure 69: during the first 0-10 ms the force cause higher particle velocity and made the particle collide with the tube in different ways.

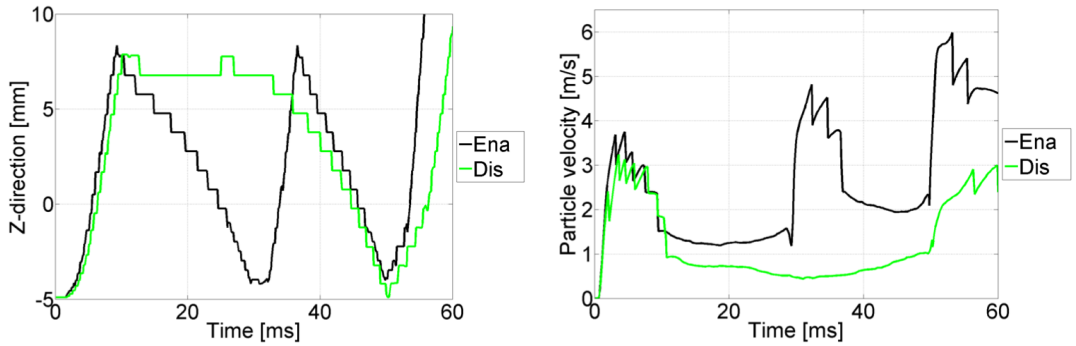


(a) Maximum particle position (b) Maximum particle velocity.

Figure 69: (a) Particle velocity magnitude as a function of time during the first 60 ms. (b) Particle position in z-direction as a function of time during the first 60 ms. Comparison of particle dispersion where the pressure gradient force were enabled (Ena) and disabled (Dis) [36].

# 6 Grid and time-step independence

### Grid sensitivity

For achieving high accuracy of numerical solutions, the grid needs to be of high quality. A detailed and fine grid compared to a rougher grid will have more grid points where the discretisized equations can be solved. The accuracy of the numerical solution will increase as the number of grid points within the domain increases.

To validate if a grid is of sufficient quality, it is advantageous to adjust the grid size by either reducing or improving the grid size. If the change is insignificant, the grid size can be set to the biggest size resulting in a small change in the solution.

By comparing the solution of a rougher grid to the solution of the grid described in section 4.2 it was discovered that the mesh had a adequately small size.

### Time-step dependency

In the process of getting a stable and converging solution, different time-steps were investigated. It was discovered a clear influence on the results after running the simulations with different time-steps. The time-step was validated by running simulations with higher and lower values. Finally, it was concluded that a time-step of $1{\cdot}10^{-4}$ was sufficiently low enough.

# 7 Concluding remarks

In this thesis, a numerical investigation of particle dispersion in a modified Hartmann tube was performed. Inlet gas velocity, number of particles and particle characteristics were varied to study their effect on the particle dispersion process. Physical models affecting the particles, such as coefficient of restitution, the shear lift force and the pressure gradient force, were also investigated. In addition, the particle dispersion in zero gravity condition was conducted to investigate the suggested "ideal" condition. The objective was to better understand the particle dispersion in normal conditions versus zero gravity condition, and evaluate how a numerical model can be a useful tool in dust explosion research.

The Eulerian-Lagrangian approach was used to simulate a two-phase flow of a small amount of particles dispersed in air. This technique made it possible to visualize the movement of each particle throughout the dispersion process as well as the settling process. Data showing volume fraction of particles, velocity, pressure and turbulent kinetic energy were recorded and the results were compared with literature.

The results showed that the gas flow was non-symmetric in the vertical cross section, this correlated with research done in literature. The particle distribution the first 20 ms are strongly affected by the placement of the nozzles and the gas flow velocity field.

The geometry of the apparatus had a significant influence on the movement of the particles. After the particle movement was initiated by the injected gas flow, the particles followed the tube bottom before colliding with the rubber seal. The particles followed two main paths after colliding with the rubber seal, where one of them correlated with results achieved in literature. The geometry of the dispersion equipment also affected the gas flow, causing vortex structures to generate at the bottom section of the tube.

In addition, the inlet velocity represented an important parameter in the dispersion of the particles. It was shown that higher inlet velocities favoured a more efficient dispersion in terms of movement in z-direction. For gas injection velocities under 40 m/s, the particle cloud never got sufficiently dispersed.

Simulations done with smaller particles showed that the particle velocity, velocity decay time and dispersion time increased. When increasing the amount of particles, no significant effect on the movement in z-direction was discovered. Nevertheless, because of the significant larger particle velocity recorded, it might indicate a greater amount of movement in x-and y-direction.

It was observed that after 100 ms an approximately uniform particle cloud was generated. In normal conditions the particles started to settle as the velocity decayed. In zero gravity condition the particles remained in suspension throughout the whole simulation, which might indicate a successful creation of the suggested "ideal" condition.

No evident effect of the pressure gradient force acting on the particles was observed. The Saffman shear lift coefficient led to a minor increase in particle velocity and a slightly larger lifting of the particles immediately after the particle movement was initiated.

The coefficient of restitution affected the particles movement significantly. As the collisions went from totally elastic to fully inelastic, the particle velocity decreased. For the particles with a coefficient of restitution value below 1.0, the velocity decelerated in each collision.

## 7.1 Further work

Even though the gas injection system created in the simulation code was customized, the creation of a even more realistic and reproducible gas injection system is preferred. This can make the simulation results easily compared to the experimental set-up. A suggestion is that a pressure-chamber can be included in the CAD-model. Other modifications that can be done to the CAD- model include inserting a filter at the outlet boundary. Since the filter used in the experiments restricts the gas flow.

For subsequent research, a smaller time-step and grid size can be used to generate even more accurate results. More simulations can be run to investigate the physical models affecting the particles in the continuous phase. In addition several monitors and measuring points can be created for obtaining more information. Another improvement is to better measure the particle cloud uniformity in the tube.

Furthermore, simulations of combustible solids are of great interest for more practical applications. The next step in making the cloud combustible is to include a much larger amount of particles in the tube. One way of doing this, without needing a extreme amount of computational power, could be by letting one particle represent a cluster or volume of particles for simplifications in the E-L model. The E-E model can also be a good tool for investigating a bigger system. It is also of practical interest how the particle cloud behave around the ignition source in the Hartmann tube.

# References


[1] Eckhoff, R. K. (2005). *Explosions Hazards in the Process Industries.* Gulf Publishing Company, Huston TX.

[2] Bozier, O., and Veyssière, B. (2010). *Study of the Mechanisms of Dust Suspension Generation in a Closed Vessel Under Microgravity Conditions.* Microgravity Science and Technology, 22:233-248.

[3] Yang, C. C. and Shih, C. L. (2016). A coordinated emergency response: *A color dust explosion at a 2015 concert in Taiwan.* American Journal of Public Health, 106:1582-1585.

[4] U.S. Chemical Safety Board and Hazard Investigation. Investigation report: Combustible dust hazard study. Report 2006-H-1, Nov. 15 2006.

[5] Hanai, H., Ueki, M., Kobayashi, H., Hasegawa, S., and Niioka, T. (1999). *A Lean Flammability Limit of Polymethylmethacrylate Particle-cloud in Microgravity.* Combustion and Flame, 118:359-369.

[6] Hanai, H., Maruta, K., Kobayashi, H. and Niioka, T. (1998). *Pulsating Flame propagation of PMMA Particle cloud in Microgravity.* Twenty-Seventh Symposium (International) on Combustion/The combustion institute, 2675-2681.

[7] Berlad, A. L., and Tangirala, V. (1989). *Reduced Gravity Combustion of Particle Cloud.* NASA Contractor Report 182299.

[8] Ballal, D., R. (1983). *Flame propagation through Dust Clouds of Carbon, Coal, Aluminium and Magnesium in an Environment of zero gravity.* Royal Society London, 385:21

[9] Jarosinski, J., Podfilipski, J., and Pu, Y. (2000). *Visualization of Dust Explosion Under Microgravity Conditions.* Combustion Science and Technology, 158:1, 183-194.

[10] Paraldi, O., Lee, J. H., Knystautas, R., Landry C., Gregorio P., and Shemie M. (1993)*Constant Volume Combustion of Aluminium dust suspension in Microgravity.* Proc. 14th International Colloquium on Dynamics of Explosions and Reactive Systems, Coimbra, Portugal.

[11] Law, C., K., Faeth, G., M. (1994). *Opportunities and challenges of combustion in microgravity.* Progress in Energy and Combustion Science, Pergamon-Elsevier Science LTD, 20:65-113.

[12] Lee, John, H., S., Peraldi, O., and Knystutas, R. (1993). *Microgravity Combustion of Dust Suspensions.* Technical Report N93-20201. Department of Mechanical Engineering, McGill University.

[13] Ross, H., Facca, L., Berland, A., and Tangirala, V. (1989). *Feasibility of Reduced Gravity Experiments involving Quiescent Uniform Particle Cloud Combustion.* NASA Technical Memo 101371

[14] Hanai, H., Maruta, K., Kobayashi, H. and Niioka, T. (2000). *Numerical study of Pulsating Flame propagation in mixtures of gas and particles.* Proceedings of the Combustion institute, 28:815-822.

[15] Ronney, D., P., Wu, M.-S., Abid, M., Niioka, T., Kobayashi, H., Maruta, K., Hanai, H., and Ueki, M. (2000). *Flammability Limits and Flame Dynamics of Spherical Flames in Homogeneous ans Heterogeneous Mixtures.* Cooperative Research Projects in the Microgravity Combustion Science Programs Sponsored by NASA and NEDO.

[16] Krazinski, L., J., Buckius, O., R. and Krier, H. (1979). *Progress in Energy and Combustion Science.* Pergamon- Elsevier Science LTD, England, 5:31-71.

[17] Joulin, G. and Deshaies, B. (1985). *On Radiation-Affected Flame Propagation in Gaseous Mixtures Seeded with Inert Particles.* Combustion Science Technology, 47: 299-315.

[18] Joulin, G. (1986). *Temperature-Lags and Radiative-Transfer in Particle Laden Gaseous Flames Part I: Steady Planar Fronts.* Combustion Science Technology, 52:377-392.

[19] Joulin, G. and Cambray, P. (1986). *Temperature-Lags and Radiative-Transfer in Particle Laden Gaseous Flames Part II: Unsteady Propagation.* Combustion Science Technology, 52:397-412.

[20] Buckmaster, J. and Agarwal, A. (1994). *Unsteady Spherical Flames in Dusty Gases.* Combustion Science Technology, 103: 191-206.

[21] Buckmaster, j. and Jackson, T. L. (1994). *The Effect of Radiation on the Thermal-Diffusive Stability Boundaries of Premixed Flames.* Combustion Science Technology, 103: 299-313.

[22] Goroshin, S., Tang, F-D., Higgins, J., A. and Lee, J., H., S. (2011). *Laminar dust flames in a reduced-gravity environment.* Acta Astronautica. 68, 656-666.

[23] Murillo, C., Dufaud, O., Bardin-Monnier, N., Lopez, O., Munoz, F., and Perrin, L. (2013). *Dust explosions: CFD modeling as a tool to characterize the relevant parameters of the dust dispersion.* Chemical Engineering Science, 104:103–116.

[24] Murillo, C. (2016). *Experimental and numerical approaches to particles dispersion in a turbulent flow: application to dust explosion.* Ph. D. Thesis; University of Lorraine.

[25] Murillo, C., Bardin-Monnier, N., Munoz, F., and Dufaud, O. (2015). *Application of CFD on the sensitivity analyses of some parameters of the modified Hartmann tube.* Journal of Loss Prevention in the Process Industries, 36:298–309.

[26] Kosinski, P. and Hoffmann, A. C. (2005). *Modelling of dust lifting using the Lagrangian approach.* International Journal of Multiphase Flow, 31:1097–1115.

[27] Ilea, C. G., Kosinski, P., and Hoffmann, A. C. (2008). *Three-dimensional simulation of a dust lifting process with varying parameters.* International Journal of Multiphase Flow, 34:869–878.

[28] Anderson, J. D. (1995) *Computational Fluid Dynamics.* McGraw-Hill, New York.

[29] Star-CCM+ (2017). *Star-CCM+ User Guide for version 12.02.* Siemens PLM Software Simcenter.

[30] Hyun-Joo Kim(2012). *Multiphase Modelling in STAR-CCM+.* CD-adapco Korea, Siemens PLM Software Simcenter.

[31] Crowe, C., Schwazkopf, J., Sommerfeld, M., and Tsuhi, Y. (2012). *Multiphase Flows with Droplets and Particles (second edition).* Taylor and Francis Group, CRC Press.

[32] Saffman, P. G. (1965). *The lift on a small sphere in a slow shear flow.* Journal of Fluid Mechanics, Cambridge Univ. Press, 22:385-400.

[33] Mei, R. (1992). *An approximate expression for the shear lift force on a spherical particle at finite Reynolds number.* International Journal of Multiphase flow, 18: 145-147.

[34] El Wakil, M. M, Ueyhara, O. A. and Myers, P. S. (1954). *A theoretical investigation of the heating-up period of injected fuel droplets vaporizing in air.* NACA Tech. Note 3179.

[35] Warnatz, J., Maas, U. and Dibble, W., R. (2006). *Combustion, physical and chemical fundamentals, modeling and simulation, experiments, pollutant formation.* Springer, Berlin; New York, 4th. edition.

[36] Christiansen, G., M. (2016). *Numerical simulations of particle dispersion in a modified Hartmann tube.* M. Sc. Thesis, University of Bergen.

[37] Berg, E., A. (2016) *Investigation of dust dispersion in a modified Hartmann tube.* M. Sc. Thesis, University of Bergen.

[38] Dalstø, K. (2017).*Numerical simulation of Particle Layer Dispersion in a Modified Hartmann tube.* M. Sc. Thesis, University of Bergen.

[39] Dust Explosion Info. (2016) For Engineers and Safety Professionals. *Characteristics of Dust Explosions.* dustexplosion.info

[40] Zydak, P. and Klemens, R. (2007). *Modelling of dust lifting process behind propagating shock wave.* Journal of Loss Prevention in the Process Industries, Elsevier SCI. LTD, 20:417–426.

[41] Christiansen, G. M., Berg, A. E., Balakin, V. B. and Kosinski, J. P. (2016). *Numerical and experimental analysis of particle dispersion in dust explosions.* 14th International Conference of Numerical Analysis and Applied Mathematics, Rhodes, Greece.